

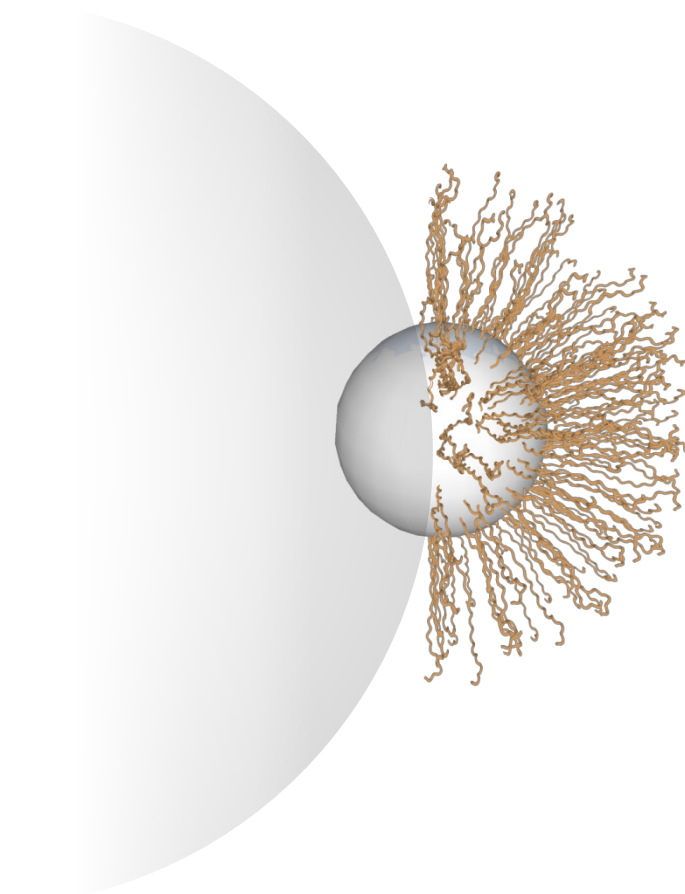


University of Crete  
Department of Materials Science and Technology  
Foundation for Research & Technology – Hellas  
Institute of Electronic Structure and Laser



Master Thesis

# Development of functional Janus particles from hybrid colloidosomes



**Dafni Moatsou**

Supervisor: Associate Professor Maria Vamvakaki

Heraklion, November 2011



*Other applications will surely emerge once researchers can attach long chain molecules to the one side of the particles.*



## Table of contents

<b>ABSTRACT</b> .....	<b>1</b>
<b>CHAPTER 1   INTRODUCTION</b> .....	<b>5</b>
1.1 JANUS PARTICLES.....	5
1.1.1 <i>Classification</i> .....	5
1.1.2 <i>Properties and Applications</i> .....	6
1.1.3 <i>Preparation Methods</i> .....	11
(i) Toposelective surface modification.....	11
(ii) Template-directed self-assembly of particles.....	12
(iii) Controlled phase separation phenomena.....	13
(iv) Controlled surface nucleation.....	13
(v) Microfluidic flow.....	13
1.2 STIMULI-RESPONSIVE POLYMERS.....	14
1.2.1 <i>pH responsive polymers</i> .....	14
1.2.2 <i>Temperature responsive polymers</i> .....	15
1.2.3 <i>Stimuli-responsive polymer-coated particles</i> .....	16
1.3 POLYMER-GRAFTED PARTICLES.....	17
1.3.1 <i>Grafting to</i> .....	18
1.3.2 <i>Grafting Density</i> .....	19
1.3.3 <i>Grafting from</i> .....	19
1.4 ATOM TRANSFER RADICAL POLYMERIZATION (ATRP).....	20
1.4.1 <i>ATRP mechanism</i> .....	20
1.4.2 <i>ATRP kinetics</i> .....	21
1.4.3 <i>ATRP components</i> .....	22

1.5 SCOPE OF THIS WORK .....	23
<b>CHAPTER 2   EXPERIMENTAL.....</b>	<b>33</b>
2.1 MATERIALS AND METHODS .....	33
2.1.1 <i>Materials</i> .....	33
2.1.2 <i>Methods</i> .....	33
2.2 SYNTHESIS OF THE ATRP INITIATORS AND THE FLUORESCENT DYES .....	34
2.2.1 <i>Synthesis of the 3-(2-bromoisobutyramido)propyl(trimethoxy) silane monofunctional initiator</i> .....	34
2.2.2 <i>Synthesis of the fluorescein-based bifunctional ATRP initiators</i> .....	34
2.2.3 <i>Synthesis of hematoporphyrin dichloride (red dye)</i> .....	35
2.3 ATOM TRANSFER RADICAL POLYMERIZATION (ATRP) IN BULK .....	36
2.4 SYNTHESIS OF FULLY POLYMER-COATED SILICA PARTICLES.....	37
2.4.1 <i>Immobilization of the monofunctional ATRP initiator onto the surface of the silica particles</i> .....	37
2.4.2 <i>Immobilization of primary amine groups onto the surface of the silica particles</i> .....	37
2.4.3 <i>Immobilization of the bifunctional ATRP initiator (FITC-Br) on the surface of the amine-functionalized silica particles</i> .....	38
2.4.4 <i>Surface-initiated atom transfer radical polymerization (ATRP) for the formation of fully-coated particles</i> .....	38
2.5 SYNTHESIS OF JANUS POLYMER-SILICA PARTICLES .....	40
2.5.1 <i>Synthesis of Janus particles using wax hybrid colloidosomes</i> .....	40
2.5.2 <i>Synthesis of polystyrene-silica (PS) hybrid colloidosomes</i> .....	41
2.5.3 <i>Synthesis of Janus colloidal initiator particles from the PS colloidosomes</i> .....	42
2.5.4 <i>Immobilization of the red fluorescent dye onto the amine-functionalized surface of the Janus particles</i> .....	43

2.5.5 Decoration of the amine-functionalized surface of the Janus particles with gold nanoparticles .....	43
2.5.6 Surface-initiated ATRP from the initiator-functionalized surface of the Janus silica particles .....	44
2.6 DEPROTECTION OF THE <i>TERT</i> -BUTYL ACRYLATE POLYMER BRUSHES .....	44
2.7 CHARACTERIZATION .....	45
2.7.1 Thermogravimetric Analysis (TGA).....	45
2.7.2 Gel Permeation Chromatography (GPC).....	45
2.7.3 Transmission Electron Microscopy (TEM) .....	45
2.7.4 Scanning Electron Microscopy (SEM) .....	45
2.7.5 Fluorescence Microscopy.....	46
2.7.6 Turbidimetry .....	46
2.7.7 Dynamic Light Scattering (DLS) .....	46
2.7.8 Static Light Scattering (SLS).....	47
2.7.9 Nuclear Magnetic Resonance (NMR).....	47
<b>CHAPTER 3   RESULTS AND DISCUSSION.....</b>	<b>49</b>
3.1 BARE SILICA PARTICLES .....	49
3.1.1 Dynamic Light Scattering (DLS) .....	49
3.1.2 Scanning and Transmission Electron Microscopy (SEM and TEM).....	49
3.2 SYNTHESIS OF THE ATRP INITIATORS .....	50
3.2.1 Synthesis of the monofunctional surface-bound ATRP initiator 3-(2-bromoisobutyramido)propyl(trimethoxy) silane.....	50
3.2.2 Synthesis of the bifunctional ATRP initiator 3-oxo-3H-spiro[isobenzofuran-1,9'-xanthene]-3',6'-diyl bis(2-bromo-2-methylpropanoate) (Fluo-Br).....	52

3.2.3 <i>Synthesis of the surface-bound bifunctional ATRP initiator 4-isothiocyanato-3-oxo-3H-spiro[isobenzofuran-1,9'-xanthene]-3',6'-diyl bis(2-bromo-2-methylpropanoate) (FITC-Br)</i> .....	54
3.3 NH <sub>2</sub> - AND ATRP INITIATOR-FUNCTIONALIZED SILICA PARTICLES .....	56
3.3.1 <i>Primary amino group functionalized silica particles</i> .....	56
3.3.2 <i>ATRP initiator-coated silica particles</i> .....	56
3.4 COLLOIDOSOMES .....	58
3.4.1 <i>Wax-silica hybrid colloidosomes</i> .....	58
(i) Wax-silica hybrid colloidosomes synthesized in methanol .....	58
(ii) Wax-silica hybrid colloidosomes synthesized in ethanol .....	59
(iii) Wax-silica hybrid colloidosomes synthesized in isopropanol .....	60
(iv) Wax-silica hybrid colloidosomes synthesized in 1-octanol .....	60
(v) Wax-silica hybrid colloidosomes synthesized in water .....	61
3.4.2 <i>Polystyrene-silica hybrid colloidosomes</i> .....	63
(i) Synthesis of the PS-SiO <sub>2</sub> hybrid colloidosomes .....	63
(ii) PS-SiO <sub>2</sub> hybrid colloidosomes after immobilization of FITC-Br on the exposed surface .....	65
3.5 JANUS COLLOIDAL INITIATOR PARTICLES .....	67
3.6 ATOM TRANSFER RADICAL POLYMERIZATION IN BULK .....	70
3.6.1 <i>ATRP in bulk initiated by the monofunctional initiator</i> .....	70
(i) ATRP of MMA in bulk .....	70
(ii) ATRP of t-BuA in bulk .....	71
(iii) ATRP of DMAEMA in bulk .....	72
3.6.2 <i>ATRP in bulk initiated by the bifunctional initiator</i> .....	77
(i) ATRP of MMA in bulk .....	77

3.7 FULLY POLYMER-COATED SILICA PARTICLES .....	79
3.7.1 PMMA fully-coated particles.....	79
3.7.2 PtBuA fully-coated particles.....	87
3.7.3 PDMAEMA fully-coated particles .....	91
(i) pH responsive behavior.....	95
(ii) Temperature-responsive properties.....	99
3.8 JANUS PARTICLES WITH A POLYMER-COATED HEMISPHERE .....	103
3.8.1 PMMA Janus particles (JF-PMMA).....	103
3.8.2 PtBuA Janus particles (JF-PtBuA).....	110
3.8.3 PDMAEMA Janus particles (JF-PDMAEMA) .....	114
(i) pH-responsive behavior .....	119
(ii) Temperature-responsive character .....	123
<b>CHAPTER 4   CONCLUSIONS.....</b>	<b>129</b>
4.1 CONTROLLED ATRP IN BULK.....	129
4.2 FULLY POLYMER-COATED PARTICLES .....	130
4.3 COLLOIDOSOMES.....	131
4.4 JANUS PARTICLES .....	132
4.5 FUTURE WORK.....	133
<b>EΥΧΑΡΙΣΤΙΕΣ.....</b>	<b>135</b>



## **Abstract**

Janus particles are named after the two-faced ancient Roman god, Janus, based on the chemical and physical anisotropy that these particles exhibit. This work focuses on the synthesis of sub-micron silica particles with asymmetric grafting of polymer chains from their surface. High demand of such particles is in contrast to their usually small-scale production. In response to that, this work takes advantage of the large surface area provided by spherical latex particles to immobilize silica particles at the latex-solvent interphase and thus provide shielding to one hemisphere of the colloidal silica particles buried in the latex particles, whereas the exposed silica surface can be chemically modified as required. Here, the exposed surface of the silica particles was functionalized with atom transfer radical polymerization initiating sites. The successful transformation of the particles into Janus precursor initiators was verified by means of transmittance electron microscopy (TEM) and fluorescence microscopy. These Janus initiator particles were used for the preparation of hybrid polymer-silica Janus particles.

In order to successfully grow well-defined polymer chains from the surface of the particles, the atom transfer radical polymerization conditions were optimized for each monomer used. In each case, the polymerization kinetic studies provided information on the reaction time and the control of the polymer molecular weight and molecular weight distribution. The results show that high polymer molecular weight and narrow molecular weight distributions are achieved, indicating the good control of the polymerization reactions.

The Janus particles synthesized comprised an amine-functionalized hemisphere and a polymer-grafted one. Three different polymers were grown from the particle surface: a hydrophobic poly(methyl methacrylate) (PMMA) leading to amphiphilic Janus particles, a hydrophobic poly(*tert*-butyl acrylate) (PtBuA) to give polyampholyte particles that can be hydrolyzed to form an anionic and pH-responsive derivative poly(acrylic acid) (PAA) and a hydrophilic cationic and pH- and temperature-responsive polymer; poly(2-(dimethylamino)ethyl methacrylate) (PDMAEMA), leading to fully hydrophilic cationic particles. For comparison, fully-coated particles of the same polymers were also synthesized employing the same polymerization conditions.

The successful grafting of the polymers from the surface of the silica particles was verified by TGA while the high polymer molecular weight and narrow molecular weight distributions were measured by GPC verifying the control of the surface-initiated polymerization reactions. Based on the results derived from these techniques the number of polymer chains grafted per particle was calculated, finding that for the polymer-silica Janus particles this number was significantly lower than for the corresponding fully polymer-coated particles. Observation by SEM provided insight on the topology of the polymer-silica Janus particles, indicating the formation of acorn-like and snowman-like particles.

The pH-dependent size of the Janus PDMAEMA particles was shown by DLS measurements verifying the pH-responsive behavior of the Janus particles. Although a temperature-induced precipitation of the particles was observed by turbidimetry, the size of the particles measured by DLS was not found to decrease before the LCST of the polymer, as was the case for the fully-coated PDMAEMA particles. Instead, an increase of the size of the particles was found attributed to the formation of controlled aggregates.

**Abbreviations**

<b>APTES</b>	(3-aminopropyl)triethoxysilane
<b>APTMS</b>	(3-aminopropyl)trimethoxysilane
<b>ATRP</b>	atom transfer radical polymerization
<b>CTAB</b>	hexadecyltrimethylammonium bromide
<b>Cu(I)Br</b>	copper(I) bromide
<b>Cu(I)Cl</b>	copper(I) chloride
<b>Cu(II)Br</b>	copper(II) bromide
<b>DLS</b>	dynamic light scattering
<b>DMAEMA</b>	2-(dimethylamino)ethyl methacrylate
<b>DMF</b>	N,N-dimethylformamide
<b>dNbpy</b>	4,4'-dinonyl-2,2'-dipyridyl
<b>EBiB</b>	ethyl $\alpha$ -bromoisobutyrate
<b>FCA</b>	monofunctional initiator fully coated particles
<b>FCF</b>	bifunctional initiator fully coated particles
<b>FITC</b>	fluorescein isothiocyanate isomer I
<b>FITC-Br</b>	4-isothiocyanato-3-oxo-3H-spiro[isobenzofuran-1,9'-xanthene]-3',6'-diyl bis(2-bromo-2-methylpropanoate)
<b>Fluo-Br</b>	3-oxo-3H-spiro[isobenzofuran-1,9'-xanthene]-3',6'-diyl bis(2-bromo-2-methylpropanoate)
<b>GPC</b>	gel permeation chromatography
<b>HMTETA</b>	1,1,4,7,10,10-hexamethyltriethylenetetramine
<b>J-FITCBr</b>	FITC-Br -functionalized Janus particles
<b>LCST</b>	lower critical solution temperature
<b>MMA</b>	methyl methacrylate
<b>M<sub>n</sub></b>	number average molecular weight
<b>NMR</b>	nuclear magnetic resonance
<b>PAA</b>	poly(acrylic acid)
<b>PDI</b>	molecular weight distribution
<b>PDMAEMA</b>	poly(2-(dimethylamino)ethyl methacrylate)
<b>PMDETA</b>	N,N,N',N',N'',N''-pentamethyldiethylenetriamine
<b>PMMA</b>	poly(methyl methacrylate)
<b>PNIPAm</b>	poly( <i>N</i> -isopropylacrylamide)
<b>PS</b>	polystyrene
<b>Pt BuA</b>	poly( <i>tert</i> -butyl acrylate)
<b>R<sub>G</sub></b>	radius of gyration
<b>R<sub>h</sub></b>	hydrodynamic radius
<b>SEM</b>	scanning electron microscopy
<b>SLS</b>	static light scattering

<b>SLS</b>	static light scattering
<b>St</b>	Styrene
<b><i>t</i>BuA</b>	<i>tert</i> -butyl acrylate
<b>TEA</b>	triethylamine
<b>TEM</b>	transmission electron microscopy
<b>TFA</b>	trifluoroacetic acid
<b>TGA</b>	thermogravimetric analysis
<b>THF</b>	tetrahydrofuran

## **Chapter 1 | Introduction**

### **1.1 Janus Particles**

In Roman mythology, Janus (or Ianus) was the god of gates, doors, doorways, beginnings and endings. He is most often depicted as having two faces or heads, facing opposite directions. The term Janus was first used in natural sciences in 1989 to describe the property of having two faces, a hydrophobic and a hydrophilic, for the partial hydrophobic modification of commercial glass beads.<sup>1</sup> Ever since, the term has been used to describe compartmentalized colloids with two sides of different polarities or chemistries.<sup>2</sup>

#### **1.1.1 Classification**

Janus particles may be classified as ‘soft’, involving unimolecular micelles and dendrimers,<sup>3-15</sup> or ‘hard’ when inorganic particles derive their asymmetry from their shape, or from the partial modification of their surface. While hard Janus particles are permanent, soft Janus particles exhibit their anisotropic character under specific conditions (i.e. solvent, temperature, etc.) where the two components segregate.<sup>6</sup> Apart from chemical composition, the localization of the anisotropy has been explored as an important aspect of synthetic Janus particles. Most reported resulting anisotropies fall under one of the categories shown in Figure 1.1.

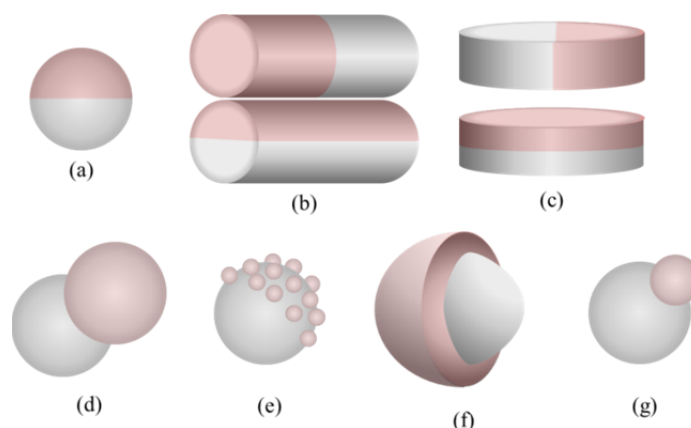


**Figure 1.1.** Schematic representation of possible Janus particles where each color represents different composition: (a) sphere, (b) cylinders, (c) disks, (d) dumbbell, (e) half-raspberry, (f) acorn, (g) snowman.

### 1.1.2 Properties and Applications

While most reports agree that Janus particles may contribute in catalysis, photonics, optics, drug delivery, membranes, microreactors, microelectronics, microfluidic, biomedical and biophysical applications only a handful provide insight on their properties, possibly due to the small amount of Janus particles synthesized by most techniques.

As Ondarçuhu *et al.* first observed in 1990<sup>16</sup> Janus particles of amphiphilic character can be exploited for their surfactant properties. It is anticipated that particles with randomly distributed hydrophilic/hydrophobic functionalities on their surface, at an oil/water interface will have a contact angle less than  $90^\circ$ . On the other hand, particles with compartmentalized functionalities will have greater contact angles and are thus expected to stabilize Pickering emulsions.<sup>17</sup>

When pH- or temperature- responsive polymers are present on either hemisphere of a Janus particle, it has been shown<sup>18</sup> that the emulsions formed are only stable at a specific range of pH and temperature values. Individual particles are observed at good solvent conditions while controlled aggregates form when one hemisphere is at poor solvent conditions.<sup>19,20</sup> Lattuada *et al.*<sup>21</sup> utilized pH-responsive polymers to functionalize the two hemispheres of magnetic particles. When both polymers on the nanoparticles had the same charge then the nanoparticles were dispersed stably as individual entities. When one of the polymers was uncharged and effectively hydrophobic in character while the other was charged, finite sized clusters were

formed. When the two polymers bear opposite charges uncontrolled aggregation occurred due to the strong dipolar interactions between the Janus nanoparticles.

Simulations<sup>22</sup> predict that the self-assembly of Janus nanoparticles at the interface of block copolymers is a viable approach to fabricate novel structures or superstructures on the nanometer scale. On the basis of this approach, oriented structures or superstructures on a macroscopic scale can be reached. The presence of Janus nanoparticles in block copolymers can provide a unique approach to create polymer nanocomposites with tunable and enhanced processing properties.

It has been experimentally shown<sup>23</sup> that Janus particles can be used to efficiently compatibilize polymer blends under high shear conditions. The performance of the Janus particles in compatibilizing the polymer blend is significantly superior to other state-of-the-art compatibilizers, such as linear block copolymers. Common problems like micellization of the stabilizer and insufficient adsorption at the interface can be overcome to a major extent. The structural ordering of Janus particles at polymer blend interfaces can occur by two ways; the first is the complete adsorption at the interface and the second is the lateral ordering at the interface.

Comparing to some experimental data, Hong *et al.*<sup>24</sup> used a simulation model to study the cluster formation of amphiphilic Janus particles. As a model they used a sphere containing a hydrophobic hemisphere and a charged hemisphere. As a result, when two hydrophobic hemispheres are faced attractive forces result, while upon rotation of the spheres, when two charged hemispheres are faced maximum repulsive forces result. What was observed was that increasing the concentration of a salt, thereby decreasing the screening length of the charged hemispheres, clusters were formed. Furthermore, even though the mechanism of cluster formation is the minimization of free energy, no frozen shape was observed, meaning that rotation of the particles within the cluster was possible.

Similarly to the above study, Hong *et al.*<sup>25</sup> compared the experimental data to the simulations of charged Janus particles forming aggregates. In their model they used a sphere bearing two hemispheres with opposite charges. Letting the distance of the particles aside (the particles were considered to touch each other), the factors that will designate the aggregates are the angles  $\varphi$  and  $\theta$  as shown in Figure 1.2.

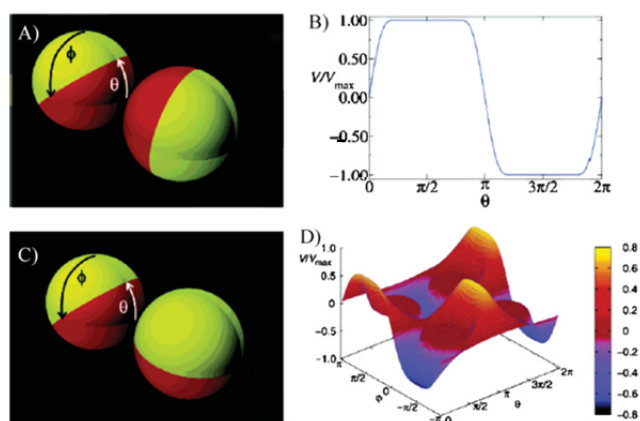


**Figure 1.2.** Simulated behavior of the charged Janus particles as a function of the angles  $\phi$  and  $\theta$ .

When the  $\phi$  angle was kept constant and the angle  $\theta$  was changed, a 2D plot of the potential over the angle  $\theta$  was formed (Figure 1.2B). The highest potential was observed when equally charged hemispheres were faced, while the lowest potential was observed for opposite charges facing. On the other hand, allowing both angles  $\theta$  and  $\phi$  change, a more complicated 4D plot was formed (Figure 1.2D).

In the same study, the aggregation pattern of the charged particles was shown as a function of the amount of particles in the aggregate. It was shown that increasing the amount of particles, a larger aggregate is formed. However the energy that keeps the aggregate together decreases monotonically as the number of particles increases.

Another approach involving charged Janus particles was shown by Goval *et al.*<sup>26</sup> In this study each Janus particle was considered to consist of two oppositely charged particles. Two cases were studied; in the first one, both particles were considered to have the same dipole moment but different sizes while in the second case both particles had the same size but different dipole moments. The resulting phase diagrams (Figure 1.3) show mixtures in the disordered phases with the appearance of the so-called string-fluid phase. Also, in the ordered phases two-phase regions appear containing single component structures.

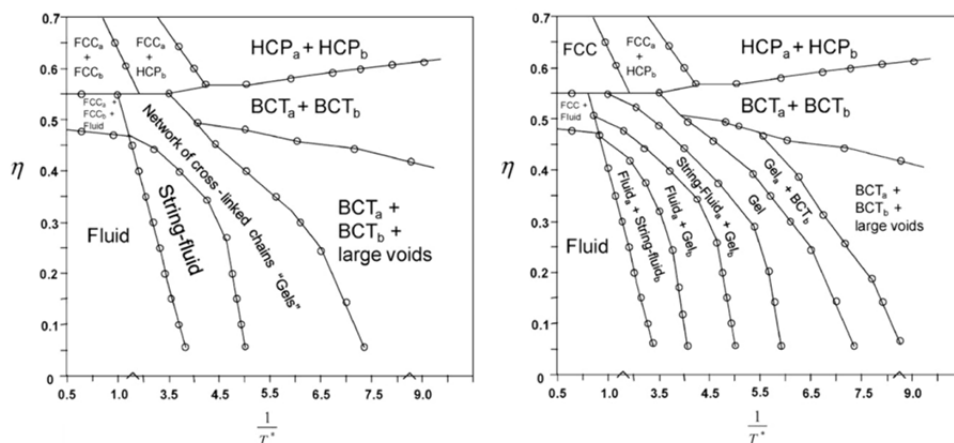


**Figure 1.3.** Phase diagrams of charged Janus particles.

Studying the control over the diffusion of Janus particles, Honegger *et al.*<sup>27</sup> utilized polystyrene particles with a gold hemisphere to demonstrate that precise 3D localization of those particles can be achieved by dielectrophoresis and that their rotation can be controlled by the gradient of the applied electrical field. Another report on magnetic Janus particles<sup>28</sup> showed that the magnetic microparticles responded to an external magnetic field on a small time scale and exhibited rotational and translational motion under a rotating magnetic field. The complex surface structures enhanced the translational velocity of the particles.

Particles can be used in biomedical applications as imaging agents and drug carriers. When polymers or ligands are tethered onto the surface of a nanoparticle, optimization of some properties may occur such as protection of their payload (hydrophobic drugs, DNA or imaging agents) during transport and the increase of their bioavailability, while remaining innocuous inside the bloodstream. It has been shown<sup>29</sup> with simulations that if only one hemisphere of the particles is tethered with ligands, the binding process of the nanoparticle with a cell densely covered with receptors is faster and results in stronger, more stable attachment employing nearly all ligands compared to a fully-coated particle. Such Janus-like nanoparticles can be rather useful for binding already existing receptor clusters and could also enhance selectivity of targeting when employing weak ligand-receptor interactions.

Porosity in a bilayer system is also important when it comes to biological membranes. Responding to an external stimulus a membrane will stretch until a critical point where it ruptures forming a pore which upon termination of the stimulus will close and disappear. For various technological applications, however, it would be

useful to design a “smart membrane” that not only forms a stable pore, but also can open and close this pore “on demand”. Such membranes could pave the way for creating novel self-healing materials, breathable fabrics, and assemblies for controlled drug delivery. Amphiphilic Janus particles in solution can localize to the edges of a pore in a lipid bilayer membrane stabilizing the pore location and size so that material can perform in a reliable, repeatable way.<sup>30</sup>

Solar energy conversion (photovoltaics), degradation of organic pollutants, transformative production of organic functional compounds, fuel cell electrochemistry, and antibacterial protection are the target applications of gold-titania snowman-like Janus particles.<sup>31</sup> Manipulating the titania photocatalytic properties (resulting from its band gap energy) and the fact that metals are good electron sinks, the resulting Janus particles exhibited well-defined photoluminescence characteristics that were consistent with electronic transitions involving trap states of the TiO<sub>2</sub> particles.<sup>31</sup> The photocatalytic activity of the heterodimer particles was also highlighted, by methanol oxidation into formaldehyde.

Janus particles with a color and electrical anisotropy have been used to create a switchable display panel.<sup>32</sup> In order to achieve this, a thin layer of these spheres was placed between two electrodes. Upon switching on an electric field, the particles orient their black sides to the negative electrode and their white sides to the positive electrode (Figure 1.4). The orientation and the color of the display can be flipped simply by reversing the electrical field.

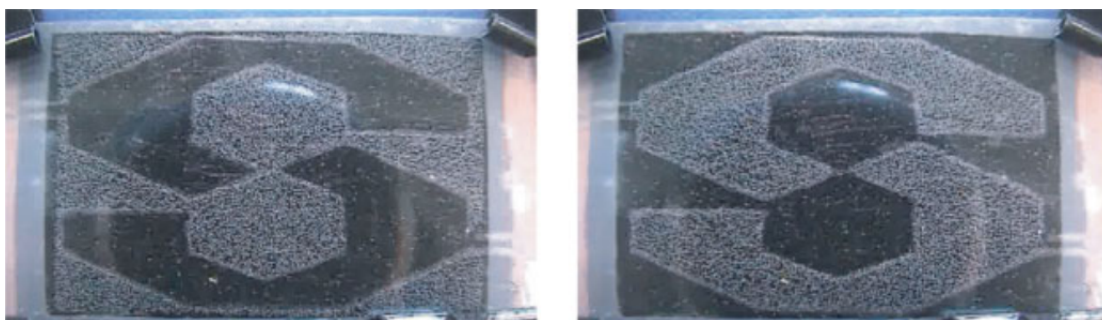


**Figure 1.4.** Display panel formed by a thin layer of color and dielectric anisotropic particles.

### 1.1.3 Preparation Methods

Even though Janus particles were unknown until 20 years ago, an astonishing amount of synthetic routes is nowadays found in the literature. Usually they involve the alteration of a symmetric particle and may be classified into five categories:<sup>33</sup> (i) toposelective surface modification, (ii) template-directed self-assembly, (iii) controlled phase-separation phenomena, (iv) controlled surface nucleation and (v) microfluidic flow.

#### *(i) Toposelective surface modification*

Perhaps the most reported pathway is the toposelective surface modification of a particle by altering one side without affecting the other. This may be succeeded in various ways as presented in Figure 1.5. Masking techniques (Figure 1.5a) involve partial immersion of the particle into a removable material, such as a photoresist. Then, they are treated by conventional methods in order to alter their exposed surface properties. Upon removal of the masking material the particles exhibit their anisotropic behavior. Initially, masking techniques involved a monolayer of the particles immersed in a flat masking medium.<sup>1,34-38</sup> However, a major drawback of this technique is the small amount of Janus particles produced which was overcome by forming a monolayer of particles in the interface of an emulsion (Pickering emulsion).<sup>19,39-47</sup> The large surface area provided by the dispersed phase can be exploited to modify gram-scale amounts of particles.

In an alternative way, spherical particles may be turned to Janus particles by being exposed to a directional flux (Figure 1.5b). One hemisphere will be exposed to the flux which will alter its surface properties and at the same time it will provide shielding to the other half, which will remain intact.<sup>48-50</sup> Major drawback of such pathways is the amount of Janus particles produced, since the particles need to be immobile during surface modification and are therefore arranged in a flat monolayer.

In a similar way, microcontact printing (Figure 1.5c) involves the contact of a “stamp”, i.e. a soft surface onto which molecules or nanoparticles are deposited, with a monolayer of particles.<sup>51-53</sup> The resulting Janus particles bare the stamped entities on one hemisphere establishing half-raspberry or snowman-like formations.

Opposite to the masking of particles, partial contact with a reactive media takes advantage of the arrangement of the particles along an interface between two media (liquid-liquid, liquid-air) into one of which the reactive species is solubilized (Figure 1.5d).<sup>54-57</sup> As a result, the hemisphere facing the inert medium remains intact while the other is modified.

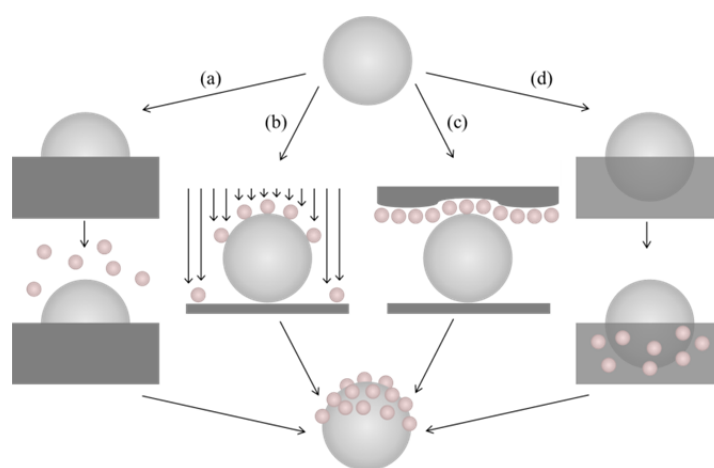


**Figure 1.5.** Schematic representation of various pathways towards the toposelective surface modification of particles by masking (a), directional flux (b), microcontact printing (c) and partial contact with a reactive medium (d).

*(ii) Template-directed self-assembly of particles*

A different pathway reported to have produced Janus particles takes advantage of a patterned surface onto which a particle dispersion is allowed to dewet.<sup>58,59</sup> Due to capillary forces the particles are trapped into the patterned holes. Repetition of the procedure with smaller particles can result in the entrapment of both particles in a hole which upon heating above the glass transition temperature of one of the components will produce Janus particles (Figure 1.6). Isolation of the Janus formations is succeeded by dissolving the pattern. However, major disadvantage of this technique is the production of a small total amount of Janus particles which in many cases are not homogeneous in terms of shape.

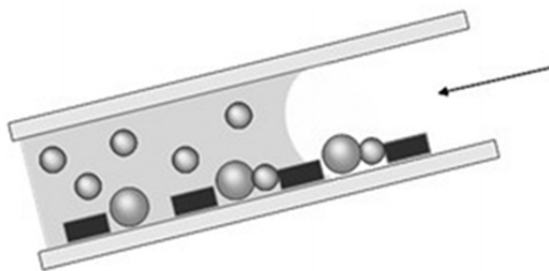


**Figure 1.6.** Schematic representation of the formation of Janus particles by template-directed self-assembly of the precursor particles.

*(iii) Controlled phase separation phenomena*

A different type of Janus particles can be produced by phase separation of two materials. Even though large scale production is feasible, the range of materials used is limited due to the nature of the reactions taking place. An example reported in the literature<sup>60</sup> involves silver core-silica shell particles which are forced into phase separation due to oxidation of silver by molecular iodine. The resulting snowman-like Janus particles are due to corruption of the silica and eruption of the silver core which forms a silver iodine particle adjacent to the silica one. In other reports,<sup>61-63</sup> seeded emulsion polymerization has been exploited in order to form dissymmetrical particles consisting of different polymers.

*(iv) Controlled surface nucleation*

Another known strategy to fabricate Janus particles is based on the nucleation and growth of a single particle onto the surface of a precursor while the 1:1 particle ratio is statistically controlled. This pathway has been extensively investigated for inorganic precursors and inorganic growths<sup>64-66</sup> but also for organic growths.<sup>67-80</sup> The formations produced are usually snowman-like or dumbbells. A major advantage of such synthetic pathways is the large-scale production of dissymmetric particles.

*(v) Microfluidic flow*

The principle of the microfluidic flow approach is to create a laminar coflowing stream of two curable liquids in a microchannel. Periodic break-up of this stream, induced by flow focusing with a third immiscible fluid (continuous phase), can

produce monodisperse micrometer-sized Janus droplets at kilohertz rates. Subsequent curing or gelling of these droplets, typically achieved through rapid photopolymerization right after droplet formation, leads to Janus particles. A striking advantage of the microfluidic approach is that large amounts of particles are obtained with extremely low polydispersity and the size and shape of these particles can be controlled by the experimental parameters. Hence, this technique has been used extensively to create Janus structures of various types.<sup>32,81-98</sup> However, all these approach has one common, intrinsic limitation: since the microfluidic droplet templating and the subsequent polymerization are coupled within a single step, flexibility in independently controlling the material properties and the morphology of the resulting particles is limited.

## **1.2 Stimuli-responsive polymers**

In nature, living systems respond to external stimuli adapting themselves to changing conditions. Polymer scientists have been trying to mimic this behavior for the last twenty years creating the so called “smart” or stimuli-responsive polymers.<sup>99</sup> These are defined as polymers that undergo reversible physical or chemical changes in response to small external changes in the environmental conditions such as temperature, pH, light, magnetic or electric field, sound, etc. Smart polymers have been proposed for use in very promising applications such as the design of biomaterials, regenerable biosensors and microfluidic bioanalytical devices.<sup>100</sup>

### **1.2.1 pH responsive polymers**

Polymers that respond to pH changes normally consist of a hydrophobic backbone onto which ionizable weak acidic or basic groups are attached.<sup>101</sup> Therefore, upon ionization of these groups the polymeric chains extend due to electrostatic interactions.

Polyacidic polymers swell at high pH values due to the negative charge of the pendant groups and their electrostatic repulsion. Upon decreasing the pH, the acidic groups become protonated and neutral. Typical acidic polymers (Figure 1.7) are poly(carboxylic acids) such as poly(acrylic acid) (PAA) and others.

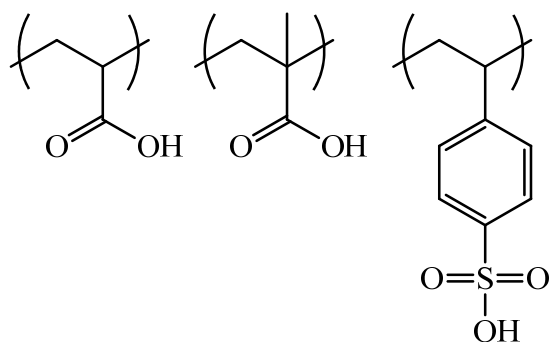


**Figure 1.7.** Examples of polyacidic polymers: poly(acrylic acid), poly(methacrylic acid) and poly(4-styrenesulfonic acid).

In contrast, polybasic polymers protonate at low pH values, while upon increasing the pH deprotonation occurs and the polymer collapses. Typical basic polymers (Figure 1.8) are polyamines such as poly(2-(dimethylamino)ethyl methacrylate).

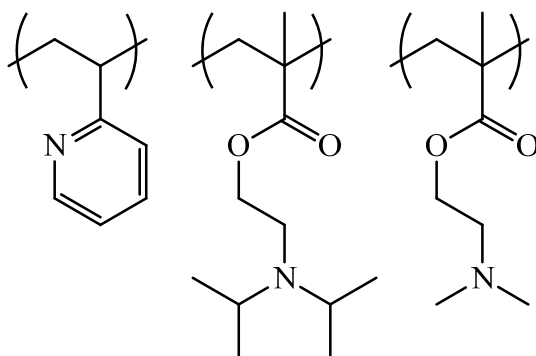


**Figure 1.8.** Examples of polybasic polymers: poly(2-vinylpyridine), poly(2-(diisopropylamino)ethyl methacrylate) and poly(2-(dimethylamino)ethyl methacrylate)

### 1.2.2 Temperature responsive polymers

Polymers that respond to temperature means disturbance of the fine balance exhibited around the critical temperature resulting in new adjustments of the interactions between the polymer chains and the solvent media.<sup>102</sup> The observed demixing process results from small temperature-dependent changes of inter- and intra-molecular interactions. At low temperatures, the accessible hydrophilic groups stabilize the homogeneous aqueous solution. Hence, the attained water-structure surrounding the polymer chains prevents the hydrophobic groups from coming

together. However, at elevated temperatures the ordered hydration structure is destroyed, resulting in aggregation of the polymer chains due to hydrophobic associations.<sup>103</sup> A very well-known temperature-responsive polymer is poly(*N*-isopropylacrylamide) (PNIPAm) which exhibits a lower critical solution temperature (LCST) at  $\sim 32$  °C in aqueous solutions. This means that above this temperature it becomes insoluble, while the decrease of the temperature will reverse the temperature effect, rendering it soluble again.<sup>102</sup> Some common temperature responsive polymers (Figure 1.9) are PNIPAm, poly(2-(dimethylamino)ethyl methacrylate) and poly(vinyl methyl ether).

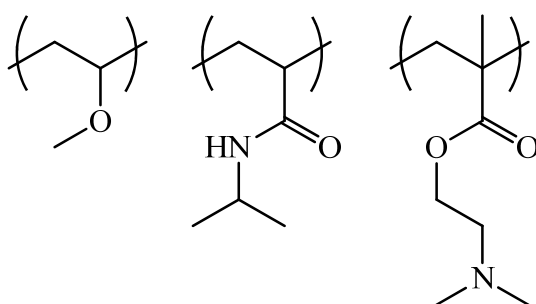


**Figure 1.9.** Common temperature-responsive polymers: poly(vinyl methyl ether), poly(*N*-isopropyl acrylamide) and poly(2-(dimethylamino)ethyl methacrylate)

### 1.2.3 Stimuli-responsive polymer-coated particles

The area of responsive colloids was born as a result of the natural merge of colloid and polymer sciences and is based on the long period of experience collected for surface modification of colloidal particles with polymers. Considering a colloidal particle decorated with polymer molecules, changes in solvent quality may strongly affect the stability of the particles' dispersions or adsorption of the particles at interface due to the solubility properties of the polymer molecules. An increase in complexity of the particle and the polymer structures and immersion of this particle in a complex solvent will result in a broad variety of multifunctional systems with important applications.<sup>104</sup>

Chen *et al.*<sup>105</sup> synthesized polyelectrolyte-grafted silica nanoparticles. When altering the pH of the aqueous suspension the zeta-potential values demonstrated that the stability of the polyelectrolyte-grafted silica particles is dictated by the nature of the grafted polyelectrolyte and is highly pH-dependent. In another study, Zhang *et*

*al.*<sup>106</sup> synthesized PDMAEMA grafted PS nanoparticles and studied their behavior in aqueous media when altering both the pH and the temperature of the solution. PDMAEMA brushes were thermoresponsive at basic pH and showed an LCST at 31 and 33 °C under pH 10 and 8, respectively. The thickness of the PDMAEMA brushes decreased with the increase of the solution pH, demonstrating their pH-sensitive characteristics. Furthermore, Zhang *et al.*<sup>107</sup> studied the behavior of silica/PNIPAm core-shell nanoparticles, around the LCST of PNIPAm (32 °C). The thermoresponsive properties of the hybrids were investigated by dynamic light scattering (DLS) as the temperature increased from 25 °C to 40 °C. The diameter did not change significantly when the temperature increased from 25 °C to 32 °C. However, from 32 °C to 33 °C, the diameter decreased from 366 nm to 284 nm, indicating that the temperature of phase transition was about 32 °C.

Finally, Song *et al.*<sup>108</sup> suggested that temperature responsive polymer-coated silica nanoparticles can be used as a packing material for high performance liquid chromatography (HPLC) with steroids, alkaloids, and substituted anilines as solutes. Control of the retention was achieved through changes in the interactions with the particles because the poly(NIPAm) stationary phase showed changes in its properties with the increase of the temperature. At low temperature poly(NIPAm) exhibited hydrophilic properties, whereas hydrophobic interactions between the stationary phase and the solutes were dominant at high temperatures.

### **1.3 Polymer-grafted Particles**

Nanoparticles have sizes of 1-1000 nm in diameter, have a large surface to volume ratio and exhibit properties intermediate between quantum and bulk materials. They can be composed of metals, semiconductors, organic polymers or core-shell structures while the physical, chemical, electrical and optical properties of these materials are size and shape dependent. Polymer coatings onto inorganic nanoparticles have been extensively reported in the literature mostly for gold, silver, alumina, carbon black and silica among others, and find applications in optics, electronics, engineering and biosciences. Polymer coated particles have been succeeded through physical or chemical methods (Figure 1.10). Physical methods involve the physisorption (adsorption) of a polymeric chain containing a sticky segment onto the surface of the

nanoparticle. This method is reversible because the forces keeping the chain in place are usually weak van der Waals forces. Chemical methods involve at least one covalent bond between the polymer and the nanoparticle and are classified into two categories: the “grafting to” and the “grafting from” approach.

### 1.3.1 Grafting to

“Grafting to” concerns a polymer chain, whose one end contains a functional group capable of reacting with the appropriate functionality of the surface. This technique provides control of the polydispersity and architecture of the polymer chains but lacks in terms of controlling the grafting density,<sup>109</sup> a term which expresses the number of grafted chains per  $\text{nm}^2$ . This is due to crowding from already attached polymer chains that prohibit high grafting densities being attained. In addition to that, the grafting reactions often require harsh conditions, e.g., high temperature and long reaction times which can induce the deterioration of the polymeric component.

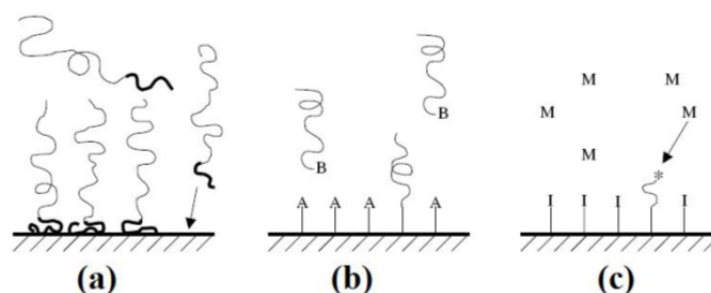


**Figure 1.10.** Representation of the various methods towards the polymer coating of a surface by (a) physisorption, (b) grafting to and (c) grafting from.

The general idea of “grafting from” is that there is an active group attached onto the surface of the particle from which polymerization may initiate. This provides the opportunity to grow chains simultaneously and requires only the diffusion of small monomer molecules into the growing polymer film, therefore crowding is avoided, allowing higher grafting densities to be attained. The active group is covalently attached onto the surface and therefore “grafting from” is non-reversible.

### 1.3.2 Grafting Density

As mentioned above, “grafting to” involves either physisorption or chemisorption resulting usually in low grafting density. This is due to the steric shielding that previously grafted chains provide to the remaining reacting sites, and it depends on the molecular weight of the polymer chains, as smaller chains are more likely to be able to diffuse within the grafted layer.<sup>110</sup> Therefore, there is a limitation to how close two chains can be grafted. This leaves the question; what is dense grafting?

For planar surfaces, the surface coverage  $\Gamma$  (mg/m<sup>2</sup>) is defined as the polymer thickness ( $h$ ) (nm) multiplied by its density ( $\rho$ ):<sup>111</sup>

$$\Gamma = h \times \rho$$

The grafting density ( $\sigma$ ) is then calculated from the surface coverage and the molecular weight of the bound polymer ( $M_n$ ) according to the equation:<sup>106</sup>

$$\sigma = \frac{602,3 \times \Gamma}{M_n}$$

For curved surfaces, the grafting density is calculated from the weight fraction of the polymeric/filler content ( $f$ ), the core density ( $\rho$ ) and radius ( $R$ ) and the molecular weight of the bound polymer ( $M_n$ ) according to the equation:

$$\sigma = \frac{f \times N_A \times \rho \times R}{3 \times M_n}$$

Taking into account the above, one can characterize the grafted polymer as “brush” when  $\sigma R_G^2 > 1$ , or “mushroom” when  $\sigma R_G^2 < 1$ ,  $R_G$  being the radius of gyration of the bound polymer.<sup>112</sup> Brushes are polymer chains that are stretched and densely grafted while mushrooms are more flexible chains grafted at a distance from each other and do not overlap.

### 1.3.3 Grafting from

There have been many reports in the literature on molecules that can be anchored onto a surface, which will define the polymerization method that will take place. For example, Boven *et al.*<sup>113</sup> reported the surface-initiated free radical polymerization of MMA by introducing 3-aminopropyltrimethoxysilane onto the surface and their reaction with an acid chloride functionalized azo initiator. Immobilization of the initiator onto the surface involved several non-quantitative reaction steps, which led to

low graft density of the initiator and tethered polymer chains. Side reactions which possibly also take place during the initiator immobilization reaction may introduce some undesired structures on the surface. Accurate characterization of the initiator layer is non-trivial. In some cases the lack of knowledge about the exact composition of the initiator layer renders the understanding of the polymerization mechanism difficult.

Another approach involved the control of the polymerization reaction utilizing “living” polymerization techniques, such as anionic polymerization. Anionic polymerization is a powerful tool towards the synthesis of well-defined polymer structures, but a major drawback is its sensitivity and lability to functional groups. Zhou *et al.*<sup>114</sup> grew polystyrene chains from silica nanoparticles via “living” anionic polymerization, although the results showed poor control of the grafting process and lack of reproducibility due to the aggregation of the particles. Other reports involved the use of reversible addition–fragmentation chain transfer (RAFT) polymerization,<sup>115</sup> ring-opening polymerization (ROP)<sup>116</sup> and carbocationic<sup>117</sup> polymerization while the majority of studies have used a polymerization technique inspired by K. Matyjaszewski; atom transfer radical polymerization.<sup>118</sup>

## **1.4 Atom Transfer Radical Polymerization (ATRP)**

Due to lack of chain transfer, termination and other side reactions, living polymerizations are appealing when the synthesis of polymers with controlled molecular weights and architectures are needed. However, their highly demanding experimental procedures as well as their limited range of monomers led in the development of a controlled radical polymerization based on atom transfer radical addition,<sup>119</sup> an efficient organic synthesis method. Independently in 1995 Mitsuo Sawamoto<sup>120</sup> and Krzysztof Matyjaszewski<sup>118</sup> developed atom transfer radical polymerization (ATRP), a reaction in which a transition metal is used as a catalyst towards the uniform growth of polymer chains.

### **1.4.1 ATRP mechanism**

The general mechanism of ATRP is depicted in Figure 1.11 where the equilibrium provided by the metal catalyst between the propagating polymer and its dormant

species is shown. Since the dormant form of the polymer is vastly preferred, side reactions are suppressed, providing the desired control over the polymer characteristics. Upon transfer of the (pseudo)halogen from the polymer (R-X) to the transition metal complex ( $M^m/L$ ), the propagating radical is formed ( $R^\cdot$ ) while the transition metal adopts a higher oxidation state ( $X-M^{m+1}$ ). Monomer units are added to the propagating polymer, in a manner similar to conventional radical polymerization, increasing its molecular weight until the radical reacts reversibly with oxidized metal complexes ( $X-M^{m+1}/L$ ) to reform the dormant species and the transition metal in the lower oxidation state ( $M^m$ ). Since ATRP is a radical-based process, the active species can also terminate.

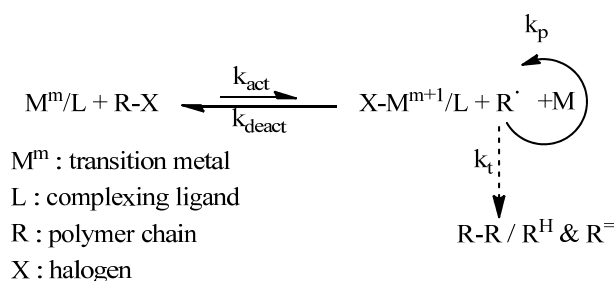


**Figure 1.11.** Reaction mechanism of metal-complex mediated ATRP.

ATRP is in many ways a complex reaction, since the polymerization process includes one or more (co)monomers, a transition metal complex in two or more oxidation states, which can comprise of various counterions and ligands, an initiator with one or more radically transferable atoms or groups and an optional solvent, suspending media or various additives. All of the components present in the reaction medium can, and often do, affect the interactions between the reagents that constitute the ATRP equilibrium.<sup>121</sup>

### 1.4.2 ATRP kinetics

Understanding the kinetics in a controlled/“living” radical polymerization is of critical importance for the design of well-defined macromolecules. Activation and deactivation of the dormant species in ATRP occur with a rate constant of activation,  $k_{\text{act}}$ , and deactivation  $k_{\text{deact}}$ , respectively. Polymer chains grow by the addition of monomers to the periodically generated radicals in a manner similar to a conventional

radical polymerization, with the rate constant of propagation,  $k_p$ . Termination reactions ( $k_t$ ) also occur in ATRP, mainly through radical coupling and disproportionation. The rate of polymerization is ultimately governed by the position of the ATRP equilibrium. The following Equation 1 illustrates how the polydispersity index of a polymer prepared by ATRP, in the absence of chain termination and transfer, relates to the concentration of initiator ( $RX$ ) and deactivator ( $D$ ), the rate constants of propagation ( $k_p$ ) and deactivation ( $k_{deact}$ ), and the monomer conversion ( $q$ ).<sup>122</sup>

$$\frac{M_w}{M_n} = 1 + \left( \frac{([RX]_o - [RX]_t)k_p}{k_{deact}[D]} \right) \left( \frac{2}{q} - 1 \right)$$

**Equation 1.** Polydispersity index dependence on ATRP variables.

Thus, for the same monomer, a catalyst that deactivates the growing chains faster will produce polymers with a lower polydispersity index (smaller  $k_p/k_{deact}$ ). Alternatively, polydispersity index decreases with an increasing concentration of deactivator, although at the cost of slower rates of polymerization. For example, the addition of a small amount of  $Cu^{II}$  halides to the feedstock (5-10%) in a standard copper-based ATRP leads to better controlled polymerizations with decreased polymerization rates, as a consequence of instantaneous control and increased initiation efficiency due to increased rate of deactivation.<sup>123</sup>

### 1.4.3 ATRP components

The ATRP initiator is most frequently an alkyl (pseudo)halide which can be either a low<sup>124</sup> or high<sup>125</sup> molar mass compound or even a part of an insoluble material, such as when initiators are tethered to the surface of modified particles,<sup>126</sup> flat wafers,<sup>127</sup> or even fibers,<sup>128</sup> etc. Copper has proven by far to be the transition metal of choice, as determined by the successful application of a spectrum of copper complexes as catalysts, for the ATRP of a broad range of monomers in diverse media by many research groups. However, other transition metals have been used such as iron,<sup>129</sup> ruthenium<sup>130</sup> and osmium.<sup>131</sup> Oxygen should be removed from the reaction medium,

but a limited amount can be tolerated particularly in the presence of an added reducing agent e.g. Cu(0), Sn(EH<sub>2</sub>), ascorbic acid, reducing sugars or amines.<sup>132</sup> An important parameter may be the addition or formation of a small amount of Cu(II) species at the beginning of the reaction, since it enables the deactivation process to occur immediately without requiring its spontaneous formation by termination reactions, thereby providing both higher initiator efficiency, reduced cost and instantaneous control.<sup>133</sup>

The spectrum of polymers that can be prepared by a well-controlled ATRP presently includes polymers with virtually any desired distribution of monomer units along the polymer backbone or within any specific segment in a copolymer. This includes homopolymers, random copolymers, alternating copolymers, gradient copolymers, block, graft, brush and star copolymers.<sup>134</sup>

### **1.5 Scope of this work**

This work focuses on the synthesis of sub-micron silica particles with asymmetric grafting of polymer chains from their surface. High demand of such particles is in contrast to their usually small-scale production. In response to that, this work takes advantage of the large surface area provided by spherical latex particles to immobilize silica particles at the latex-solvent interphase and thus provide shielding to one hemisphere of the colloidal silica particles buried in the latex particles, whereas the exposed silica surface can be chemically modified as required. Here, the exposed surface of the silica particles was functionalized with atom transfer radical polymerization initiating sites. The successful transformation of the particles into Janus precursor initiators was verified by means of transmittance electron microscopy (TEM) and fluorescence microscopy. These Janus initiator particles were used for the preparation of hybrid polymer-silica Janus particles.

In order to successfully grow well-defined polymer chains from the surface of the particles, the atom transfer radical polymerization conditions were optimized for each monomer used. In each case, the polymerization kinetic studies provided information on the reaction time and the control of the polymer molecular weight and molecular weight distribution.

The Janus particles synthesized comprised an amine-functionalized hemisphere and a polymer-grafted one. Three different polymers were grown from the particle surface: a hydrophobic poly(methyl methacrylate) (PMMA) leading to amphiphilic Janus particles, a hydrophobic poly(*tert*-butyl acrylate) (PtBuA) to give polyampholyte particles that can be hydrolyzed to form an anionic and pH-responsive derivative poly(acrylic acid) (PAA) and a hydrophilic cationic and pH- and temperature-responsive polymer; poly(2-(dimethylamino)ethyl methacrylate) (PDMAEMA), leading to fully hydrophilic cationic particles. For comparison, fully-coated particles of the same polymers were also synthesized employing the same polymerization conditions.

Both the fully-coated and the Janus particles were characterized by means of thermogravimetric analysis (TGA), dynamic and static light scattering (DLS, SLS) and scanning electron microscopy (SEM). Gel permeation chromatography (GPC) was employed to analyze the synthesized polymers in terms of molecular weight and molecular weight distribution and used to calculate the polymer grafting density.

The solution behavior of the temperature- and pH-responsive PDMAEMA particles was examined by turbidimetry, DLS and potentiometric titrations.

- 
- (1) Casagrande, C. Fabre, P. Guedeau, M.; Veyssie, M. *Europhysics Letters* **1987**, *3*, 73-78.
  - (2) Walther, A.; Müller, A. H. E. *Soft Matter* **2008**, *4*, 663.
  - (3) Voets, I. K. Leermakers, F. A. de Keizer, A. Charlaganov, M.; Stuart, M. A. C. *Advances in Polymer Science* **2011**, *241*, 163–185.
  - (4) Dupont, J.; Liu, G. *Soft Matter* **2010**, *6*, 3654.
  - (5) Wu, Z. Liang, H. Lu, J.; Deng, W.-L. *Journal of Polymer Science Part A: Polymer Chemistry* **2010**, *48*, 3323-3330.
  - (6) Walther, A. Barner-Kowollik, C.; Müller, A. H. E. *Langmuir* **2010**, *26*, 12237-46.
  - (7) Ariura, F. Schappacher, M. Borsali, R.; Deffieux, A. *Reactive and Functional Polymers* **2009**, *69*, 402-408.

- (8) Cheng, L. Zhang, G. Zhu, L. Chen, D.; Jiang, M. *Angewandte Chemie International Edition* **2008**, *47*, 10171-4.
- (9) Li, X. Yang, H. Xu, L. Fu, X. Guo, H.; Zhang, X. *Macromolecular Chemistry and Physics* **2010**, *211*, 297-302.
- (10) Christodoulou, S. Driva, P. Iatrou, H.; Hadjichristidis, N. *Macromolecules* **2008**, *41*, 2607-2615.
- (11) Lanson, D. Schappacher, M. Borsali, R.; Deffieux, A. *Macromolecules* **2007**, *40*, 9503-9509.
- (12) Nie, L. Liu, S. Shen, W. Chen, D.; Jiang, M. *Angewandte Chemie International Edition* **2007**, *46*, 6321-4.
- (13) Wurm, F. König, H. M. Hilf, S.; Kilbinger, A. F. M. *Journal of the American Chemical Society* **2008**, *130*, 5876-7.
- (14) Erhardt, R. Zhang, M. Böker, A. Zettl, H. Abetz, C. Frederik, P. Krausch, G. Abetz, V.; Müller, A. H. E. *Journal of the American Chemical Society* **2003**, *125*, 3260-7.
- (15) Heroguez, V. Gnanou, Y.; Fontanille, M. *Macromolecules* **1997**, *30*, 4791-4798.
- (16) Ondarçuhu, T. Fabre, P. Raphaël, E.; Veyssié, M. *Journal de Physique France* **1990**, *51*, 1527-1536.
- (17) Fan, H. Resasco, D. E.; Striolo, A. *Langmuir* **2011**, *27*, 5264-74.
- (18) Tanaka, T. Okayama, M. Minami, H.; Okubo, M. *Langmuir* **2010**, *26*, 11732-11736.
- (19) Umeda, Y. Kobayashi, T. Hirai, T.; Suzuki, D. *Colloid and Polymer Science* **2010**, *289*, 729-737.
- (20) Isojima, T. Lattuada, M. Vander Sande, J. B.; Hatton, T. A. *ACS nano* **2008**, *2*, 1799-806.
- (21) Lattuada, M.; Hatton, T. A. *Journal of the American Chemical Society* **2007**, *129*, 12878-89.
- (22) Yan, L.-T. Popp, N. Ghosh, S.-K.; Böker, A. *ACS nano* **2010**, *4*, 913-20.
- (23) Walther, A. Matussek, K.; Müller, A. H. E. *ACS nano* **2008**, *2*, 1167-78.
- (24) Hong, L. Cacciuto, A. Luijten, E.; Granick, S. *Langmuir* **2008**, *24*, 621-5.
- (25) Hong, L. Cacciuto, A. Luijten, E.; Granick, S. *Nano letters* **2006**, *6*, 2510-4.
- (26) Goyal, A. Hall, C. K.; Velev, O. D. *Soft Matter* **2010**, *6*, 480.

- (27) Honegger, T. Lecarme, O. Berton, K.; Peyrade, D. *Microelectronic Engineering* **2010**, *87*, 756-759.
- (28) Kim, S.-H. Sim, J. Y. Lim, J.-M.; Yang, S.-M. *Angewandte Chemie International Edition* **2010**, *49*, 3786-90.
- (29) Djohari, H.; Dormidontova, E. E. *Biomacromolecules* **2009**, *10*, 3089-97.
- (30) Alexeev, A. Uspal, W. E.; Balazs, A. C. *ACS nano* **2008**, *2*, 1117-22.
- (31) Pradhan, S. Ghosh, D.; Chen, S. *ACS Applied Materials & Interfaces* **2009**, *1*, 2060-5.
- (32) Nisisako, T. Torii, T. Takahashi, T.; Takizawa, Y. *Advanced Materials* **2006**, *18*, 1152-1156.
- (33) Perro, A. Reculosa, S. Ravaine, S. Bourgeat-Lami, E.; Duguet, E. *Journal of Materials Chemistry* **2005**, *15*, 3745.
- (34) Gong, J. Zu, X. Li, Y. Mu, W.; Deng, Y. *Journal of Materials Chemistry* **2011**, *21*, 2067.
- (35) Anderson, K. D. Luo, M. Jakubiak, R. Naik, R. R. Bunning, T. J.; Tsukruk, V. V. *Chemistry of Materials* **2010**, *22*, 3259-3264.
- (36) Ling, X. Y. Phang, I. Y. Acikgoz, C. Yilmaz, M. D. Hempenius, M. Vancso, G. J.; Huskens, J. *Angewandte Chemie International Edition* **2009**, *48*, 7677-82.
- (37) Bao, Z. Chen, L. Weldon, M. Chandross, E. Cherniavskaya, O. Dai, Y.; Tok, J. B.-H. *Chemistry of Materials* **2002**, *14*, 24-26.
- (38) Paunov, V. N.; Cayre, O. J. *Advanced Materials* **2004**, *16*, 788-791.
- (39) Rahman, M. M. Montagne, F. Fessi, H.; Elaissari, A. *Soft Matter* **2011**, *7*, 1483.
- (40) Li, D. He, Y.; Wang, S. *The Journal of Physical Chemistry C* **2009**, *113*, 12927-12929.
- (41) Liu, B. Zhang, C. Liu, J. Qu, X.; Yang, Z. *Chemical Communications* **2009**, 3871-3.
- (42) Liu, B. Wei, W. Qu, X.; Yang, Z. *Angewandte Chemie International Edition* **2008**, *47*, 3973-5.
- (43) Perro, A. Meunier, F. Schmitt, V.; Ravaine, S. *Colloids and Surfaces A: Physicochemical and Engineering Aspects* **2009**, *332*, 57-62.
- (44) Suzuki, D. Tsuji, S.; Kawaguchi, H. *Journal of the American Chemical Society* **2007**, *129*, 8088-9.

- (45) He, Y.; Li, K. *Journal of Colloid and Interface Science* **2007**, *306*, 296-9.
- (46) Jiang, S.; Granick, S. *Langmuir* **2008**, *24*, 2438-45.
- (47) Yin, Y. Zhou, S. You, B.; Wu, L. *Journal of Polymer Science Part A: Polymer Chemistry* **2011**, *49*, 3272-3279.
- (48) Takei, H. *Langmuir* **1997**, *13*, 1865-1868.
- (49) Lu, Y. Xiong, H. Jiang, X. Xia, Y. Prentiss, M.; Whitesides, G. M. *Journal of the American Chemical Society* **2003**, *125*, 12724-5.
- (50) Hugonnot, E. Carles, A. Delville, M.; Panizza, P. *Langmuir* **2003**, 226-229.
- (51) Koo, H. Y. Yi, D. K. Yoo, S. J.; Kim, D.-Y. *Advanced Materials* **2004**, *16*, 274-277.
- (52) Cayre, O. Paunov, V. N.; Veleev, O. D. *Journal of Materials Chemistry* **2003**, *13*, 2445.
- (53) Cayre, O. Paunov, V. N.; Veleev, O. D. *Chemical Communications* **2003**, *44*, 2296-7.
- (54) Fujimoto, K. Nakahama, K.; Shidara, M. *Langmuir* **1999**, *15*, 4630-4635.
- (55) Nakahama, K. Kawaguchi, H.; Fujimoto, K. *Langmuir* **2000**, *16*, 7882-7886.
- (56) Petit, L. Manaud, J.-P. Mingotaud, C. Ravaine, S.; Duguet, E. *Materials Letters* **2001**, 478-484.
- (57) Petit, L. Sellier, E. Duguet, E. Ravaine, S.; Mingotaud, C. *Journal of Materials Chemistry* **2000**, *10*, 253-254.
- (58) Yin, Y. Lu, Y.; Xia, Y. *Journal of the American Chemical Society* **2001**, *123*, 771-2.
- (59) Nagle, L.; Fitzmaurice, D. *Advanced Materials* **2003**, *15*, 933-935.
- (60) Giersig, M. Ung, T. Liz-Marzán, L. M.; Mulvaney, P. *Advanced Materials* **2004**, *9*, 570-575.
- (61) Okubo, M. Yamashita, T. Minami, H.; Konishi, Y. *Colloid & Polymer Science* **1998**, *276*, 887-892.
- (62) Kirsch, S. Pfau, A. Landfester, K. Shaffer, O.; El-Aasser, M. S. *Macromolecular Symposia* **2000**, *151*, 413-418.
- (63) Pfau, A. Sander, R.; Kirsch, S. *Langmuir* **2002**, *18*, 2880-2887.
- (64) Teranishi, T. Inoue, Y. Nakaya, M. Oumi, Y.; Sano, T. *Journal of the American Chemical Society* **2004**, *126*, 9914-5.

- (65) Yu, H. Chen, M. Rice, P. M. Wang, S. X. White, R. L.; Sun, S. *Nano Letters* **2005**, *5*, 379-82.
- (66) Gao, X. Yu, L. MacCuspie, R.; Matsui, H. *Advanced Materials* **2005**, *17*, 426-429.
- (67) Wang, Y. Xu, H. Ma, Y. Guo, F. Wang, F.; Shi, D. *Langmuir* **2011**, *27*, 7207-12.
- (68) Meng, Z. Xue, C. Lu, L. Yuan, B. Yu, X. Xi, K.; Jia, X. *Journal of colloid and interface science* **2011**, *356*, 429-33.
- (69) Nguyen, D. Ravaine, S. Bourgeat-Lami, E.; Duguet, E. *Journal of Materials Chemistry* **2010**, *20*, 9392.
- (70) Tang, C. Zhang, C. Liu, J. Qu, X. Li, J.; Yang, Z. *Macromolecules* **2010**, *43*, 5114-5120.
- (71) Zhang, C. Liu, B. Tang, C. Liu, J. Qu, X. Li, J.; Yang, Z. *Chemical communications* **2010**, *46*, 4610-2.
- (72) Tanaka, T. Okayama, M. Kitayama, Y. Kagawa, Y.; Okubo, M. *Langmuir* **2010**, *26*, 7843-7.
- (73) Fujibayashi, T. Tanaka, T. Minami, H.; Okubo, M. *Colloid and Polymer Science* **2010**, *288*, 879-886.
- (74) Feyen, M. Weidenthaler, C. Schüth, F.; Lu, A.-H. *Journal of the American Chemical Society* **2010**, *132*, 6791-9.
- (75) Reculosa, S. Poncet-Legrand, C.; Perro, A. *Chemistry of Materials* **2005**, *17*, 3338-3344.
- (76) Wang, Y. Xu, H. Qiang, W. Gu, H.; Shi, D. *Journal of Nanomaterials* **2009**, *2009*, 1-5.
- (77) Lu, W. Chen, M.; Wu, L. *Journal of colloid and interface science* **2008**, *328*, 98-102.
- (78) Hoffmann, M. Lu, Y. Schrunner, M. Ballauff, M.; Harnau, L. *The Journal of Physical Chemistry B* **2008**, *112*, 14843-50.
- (79) Monteil, V. Stumbaum, J. Thomann, R.; Mecking, S. *Macromolecules* **2006**, *39*, 2056-2062.
- (80) Perro, A. Reculosa, S. Pereira, F. Delville, M.-H. Mingotaud, C. Duguet, E. Bourgeat-Lami, E.; Ravaine, S. *Chemical Communications* **2005**, 5542-3.

- (81) Prasad, N. Perumal, J. Choi, C.-H. Lee, C.-S.; Kim, D.-P. *Advanced Functional Materials* **2009**, *19*, 1656-1662.
- (82) Kim, S.-H. Jeon, S.-J. Jeong, W. C. Park, H. S.; Yang, S.-M. *Advanced Materials* **2008**, *20*, 4129.
- (83) Gangwal, S. Cayre, O. Bazant, M.; Velez, O. *Physical Review Letters* **2008**, *100*, 1-4.
- (84) Jang, J.-H. Dendukuri, D. Hatton, T. A. Thomas, E. L.; Doyle, P. S. *Angewandte Chemie International Edition* **2007**, *46*, 9027-31.
- (85) Nisisako, T.; Torii, T. *Advanced Materials* **2007**, *19*, 1489-1493.
- (86) Shepherd, R. F. Conrad, J. C. Rhodes, S. K. Link, D. R. Marquez, M. Weitz, D. A.; Lewis, J. A. *Langmuir* **2006**, *22*, 8618-22.
- (87) Nie, Z. Li, W. Seo, M. Xu, S.; Kumacheva, E. *Journal of the American Chemical Society* **2006**, *128*, 9408-12.
- (88) Yin, S.-N. Wang, C.-F. Yu, Z.-Y. Wang, J. Liu, S.-S.; Chen, S. *Advanced Materials* **2011**, *23*, 2915-9.
- (89) Zhao, Y. Shum, H. C. Chen, H. Adams, L. L. A. Gu, Z.; Weitz, D. A. *Journal of the American Chemical Society* **2011**, *133*, 8790-3.
- (90) Lone, S. Kim, S. H. Nam, S. W. Park, S. Joo, J.; Cheong, I. W. *Chemical Communications* **2011**, *47*, 2634-6.
- (91) Lone, S. Kim, S. H. Nam, S. W. Park, S.; Cheong, I. W. *Langmuir* **2010**, *26*, 17975-80.
- (92) Lee, C. Choi, C.-H.; Jung, J.-H. In *Proceedings of the 2010 5th IEEE International Conference on Nano/Micro Engineered and Molecular Systems*; 2010; pp. 902-905.
- (93) Ahn, S. Kim, D. W. Kim, Y. W.; Yoo, J. Y. *International Journal of Precision Engineering and Manufacturing* **2010**, *11*, 799-802.
- (94) Seiffert, S. Romanowsky, M. B.; Weitz, D. A. *Langmuir* **2010**, *26*, 14842-7.
- (95) Lewis, C. L. Lin, Y. Yang, C. Manocchi, A. K. Yuet, K. P. Doyle, P. S.; Yi, H. *Langmuir* **2010**, *26*, 13436-41.
- (96) Nisisako, T.; Hatsuzawa, T. *Microfluidics and Nanofluidics* **2009**, *9*, 427-437.
- (97) Yuet, K. P. Hwang, D. K. Haghgoie, R.; Doyle, P. S. *Langmuir* **2010**, *26*, 4281-7.

- (98) Torisawa, Y.-S. Mosadegh, B. Luker, G. D. Morell, M. O'Shea, K. S.; Takayama, S. *Integrative Biology* **2009**, *1*, 649-54.
- (99) Aguilar, M. R. Elvira, C. Gallardo, A. Vázquez, B.; Román, J. S. In *Topics in Tissue Engineering*; Ashammakhi, N. Reis, R. L.; Chiellini, E., Eds. Citeseer, 2007; Vol. 3, p. 6.
- (100) Nath, N.; Chilkoti, A. *Advanced Materials* **2002**, *14*, 1243-1247.
- (101) Dai, S. Ravi, P.; Tam, K. C. *Soft Matter* **2008**, *4*, 435.
- (102) Fujishige, S. Kubota, K.; Ando, I. *The Journal of Physical Chemistry* **1989**, *93*, 3311-3313.
- (103) Durme, K. Assche, G. Rahier, H.; Mele, B. *Journal of Thermal Analysis and Calorimetry* **2009**, *98*, 495-505.
- (104) Motornov, M. Roiter, Y. Tokarev, I.; Minko, S. *Progress in Polymer Science* **2010**, *35*, 174-211.
- (105) Chen, X. Randall, D. P. Perruchot, C. Watts, J. F. Patten, T. E. von Werne, T.; Armes, S. P. *Journal of Colloid and Interface Science* **2003**, *257*, 56-64.
- (106) Zhang, M. Liu, L. Wu, C. Fu, G. Zhao, H.; He, B. *Polymer* **2007**, *48*, 1989-1997.
- (107) Zhang, K. Ma, J. Zhang, B. Zhao, S. Li, Y. Xu, Y. Yu, W.; Wang, J. *Materials Letters* **2007**, *61*, 949-952.
- (108) Song, Y.-X. Wang, J.-Q. Su, Z.-X.; Chen, D.-Y. *Chromatographia* **2001**, *54*, 208-212.
- (109) Lyatskaya, Y.; Balazs, A. C. *Macromolecules* **1998**, *31*, 6676-6680.
- (110) Xie, L. Xu, F. Qiu, F. Lu, H.; Yang, Y. *Macromolecules* **2007**, *40*, 3296-3305.
- (111) Luzinov, I. Julthongpiput, D. Malz, H. Pionteck, J.; Tsukruk, V. V. *Macromolecules* **2000**, *33*, 1043-1048.
- (112) Buguin, A.; Brochard-Wyart, F. *Macromolecules* **1996**, *29*, 4937-4943.
- (113) Boven, G. Folkersma, R. Challa, G. Schouten, A. J.; Bosma, M. *Polymer* **1992**, *33*, 83-88.
- (114) Zhou, Q. Wang, S. Fan, X. Advincula, R.; Mays, J. *Langmuir* **2002**, *18*, 3324-3331.
- (115) Zhao, Y.; Perrier, S. *Macromolecules* **2007**, *40*, 9116-9124.
- (116) Carrot, G. Rutot-Houzé, D. Pottier, A. Degée, P. Hilborn, J.; Dubois, P. *Macromolecules* **2002**, *35*, 8400-8404.

- (117) Binder, W. H. Zirbs, R. Machl, D.; Gahleitner, M. *Macromolecules* **2009**, *42*, 7379-7387.
- (118) Wang, J.-S.; Matyjaszewski, K. *Journal of the American Chemical Society* **1995**, *117*, 5614-5615.
- (119) Minisci, F. *Accounts of Chemical Research* **1975**, *8*, 165-171.
- (120) Kato, M. Kamigaito, M. Sawamoto, M.; Higashimura, T. *Macromolecules* **1995**, *28*, 1721-1723.
- (121) Braunecker, W.; Matyjaszewski, K. *Progress in Polymer Science* **2007**, *32*, 93-146.
- (122) Matyjaszewski, K. In *Macromolecular Symposia*; Wiley Online Library, 1996; Vol. 111, pp. 47-61.
- (123) Matyjaszewski, K. Wei, M. Xia, J.; Gaynor, S. G. *Macromolecular Chemistry and Physics* **1998**, *2292*, 2289-2292.
- (124) Matyjaszewski, K. Patten, T. E.; Xia, J. *Journal of the American Chemical Society* **1997**, *119*, 674-680.
- (125) Coca, S. Paik, H.-J.; Matyjaszewski, K. *Macromolecules* **1997**, *30*, 6513-6516.
- (126) Böttcher, H. Hallensleben, M. L. Nuß, S.; Wurm, H. *Polymer Bulletin* **2000**, *44*, 223-229.
- (127) Matyjaszewski, K. Miller, P. J. Shukla, N. Immaraporn, B. Gelman, A. Luokala, B. B. Siclovan, T. M. Kickelbick, G. Vallant, T. Hoffmann, H.; Pakula, T. *Macromolecules* **1999**, *32*, 8716-8724.
- (128) Carlmark, A.; Malmström, E. E. *Biomacromolecules* **2003**, *4*, 1740-5.
- (129) Matyjaszewski, K. Wei, M. Xia, J.; McDermott, N. E. *Macromolecules* **1997**, *30*, 8161-8164.
- (130) Simal, F. Demonceau, A.; Noels, A. F. *Angewandte Chemie International Edition* **1999**, *38*, 538-540.
- (131) Braunecker, W. Itami, Y.; Matyjaszewski, K. *Macromolecules* **2005**, *38*, 9402-9404.
- (132) Matyjaszewski, K. Coca, S. Gaynor, S.; Wei, M. *Macromolecules* **1998**, *31*, 5967-5969.
- (133) Becer, C. R. Hoogenboom, R. Fournier, D.; Schubert, U. S. *Macromolecular Rapid Communications* **2007**, *28*, 1161-1166.

- (134) Bernaerts, K. V. Fustin, C.-A. Bomal-D'Haese, C. Gohy, J.-F. Martins, J. C.; Du Prez, F. E. *Macromolecules* **2008**, *41*, 2593-2606.

## **Chapter 2 | Experimental**

### **2.1 Materials and Methods**

#### **2.1.1 Materials**

2,2'-azobis(2-methylpropionitrile) (98%) was purchased from Acros Organics, hematoporphyrin dihydrochloride was acquired from Alfa Aesar and the silica particles were obtained from Fiber Optic Center Inc. ( $D = 250 \text{ nm}$ ,  $d = 2 \text{ g/cm}^3$ ). Ethanol, fluorescein and thionyl chloride (97%) were purchased from Fluka. (3-aminopropyl)triethoxysilane (99%), (3-aminopropyl)trimethoxysilane (97%), chloroform, fluorescein isothiocyanate isomer I (90%), *N,N*-dimethylformamide, ninhydrin, sodium bicarbonate, tetrahydrofuran, triethylamine,  $\alpha$ -bromoisobutyryl bromide (98%), styrene, methanol, toluene, methyl methacrylate (99%), isopropanol, 1-octanol, hexadecyltrimethylammonium bromide, ethyl  $\alpha$ -bromoisobutyrate (98%), 4,4'-dinonyl-2,2'-dipyridyl (97%), copper(I) chloride (99%), *tert*-butyl acrylate (98%), *N,N,N',N'',N''*-pentamethyldiethylenetriamine (99%), copper(I) bromide (99.9%), copper(II) bromide (99%), 2-(dimethylamino)ethyl methacrylate (98%), calcium hydride, glacial acetic acid, trifluoroacetic acid (99%), paraffin wax (mp 55-57 °C) and 1,1,4,7,10,10-hexamethyltriethylenetetramine (97%) were obtained from Sigma-Aldrich. Milli-Q water of a specific resistivity of 18 M $\Omega$ .cm was used in all experiments.

#### **2.1.2 Methods**

The monomers, methyl methacrylate (MMA), *tert*-butyl acrylate (*t*BuA) and 2-(dimethylamino)ethyl methacrylate (DMAEMA) were passed through a basic alumina column to remove the inhibitors prior to use. For the synthesis of the initiators, solvents were dried by distillation over calcium hydride and were kept under a dry nitrogen atmosphere until use.  $\alpha$ -bromoisobutyryl bromide was distilled under vacuum and was kept under nitrogen until use. Tetrahydrofuran (THF) was refluxed over potassium to remove traces of water and was freshly distilled, before use. Copper(I) chloride (Cu(I)Cl) and copper(I) bromide (Cu(I)Br) were washed with

glacial acetic acid and ethanol to remove traces of oxidized metal and were dried under reduced pressure before use. All other reagents were used as supplied.

## 2.2 Synthesis of the ATRP initiators and the fluorescent dyes

### 2.2.1 Synthesis of the 3-(2-bromoisobutyramido)propyl(trimethoxy) silane monofunctional initiator

The monofunctional ATRP initiator which was immobilized on the surface of the silica particles was synthesized according to the procedure described by Tugulu et al.<sup>1</sup> (Figure 2.1). In a dry round bottom flask 7 mL (40 mmol) of (3-aminopropyl)trimethoxysilane (APTMS) was added, followed by the addition of 60 mL of THF and 6.7 mL (48 mmol) of triethylamine (TEA) under a nitrogen flow and continuous stirring. The reaction mixture was cooled down to 0 °C and 6 mL (48 mmol) of  $\alpha$ -bromoisobutyryl bromide were added dropwise. The reaction was allowed to proceed under nitrogen for 3 hours at RT. The triethylammonium bromide salt produced was removed by filtration under nitrogen to avoid the hydrolysis of the trimethoxysilyl group of the molecule. The filtrate was evaporated to dryness under reduced pressure and the oily residue was stirred under vacuum at 50 °C for 7 h to remove traces of unreacted reagents. The product was characterized by <sup>1</sup>H NMR and was stored at 4 °C under nitrogen until use.

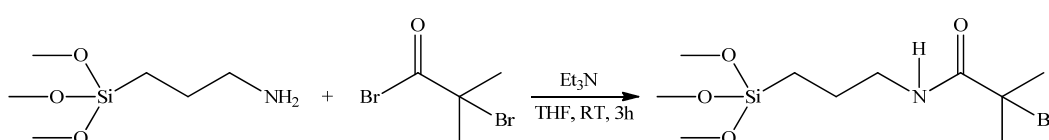


**Figure 2.1.** Reaction scheme of the synthesis of 3-(2-bromoisobutyramido)propyl(trimethoxy) silane.

### 2.2.2 Synthesis of the fluorescein-based bifunctional ATRP initiators

The free initiator, 3-oxo-3H-spiro[isobenzofuran-1,9'-xanthene]-3',6'-diyl bis(2-bromo-2-methylpropanoate) (Fluo-Br), was synthesized according to a procedure described in the literature (Figure 2.2, a).<sup>2</sup> Briefly, in a dry 250 mL round bottom flask 2.15 g (6.47 mmol) of fluorescein were added, followed by the addition of 100 mL of dry *N,N*-dimethylformamide (DMF) and 4.5 mL (32.4 mmol) of TEA under a

nitrogen flow and continuous stirring. Next, the reaction mixture was cooled down to 0 °C and 2 mL (16.2 mmol) of  $\alpha$ -bromoisobutyryl bromide were added. The reaction was allowed to proceed overnight before removing the excess of reagents under reduced pressure. The brown residue was diluted with chloroform and filtered in order to remove the triethylammonium bromide salt produced. The initiator was purified by extraction of the acid with saturated sodium bicarbonate and then water. The organic phase was isolated and dried under reduced pressure to retrieve the orange product which was characterized by NMR (yield 48 %). Using a similar procedure, 4-isothiocyanato-3-oxo-3H-spiro[isobenzofuran-1,9'-xanthene]-3',6'-diyl bis(2-bromo-2-methylpropanoate) (FITC-Br) was produced utilizing fluorescein isothiocyanate (FITC) to bind the ATRP initiator onto the surface of amine-functionalized silica particles via the isothiocyanate groups (Figure 2.2, b). The product was characterized by NMR spectroscopy.

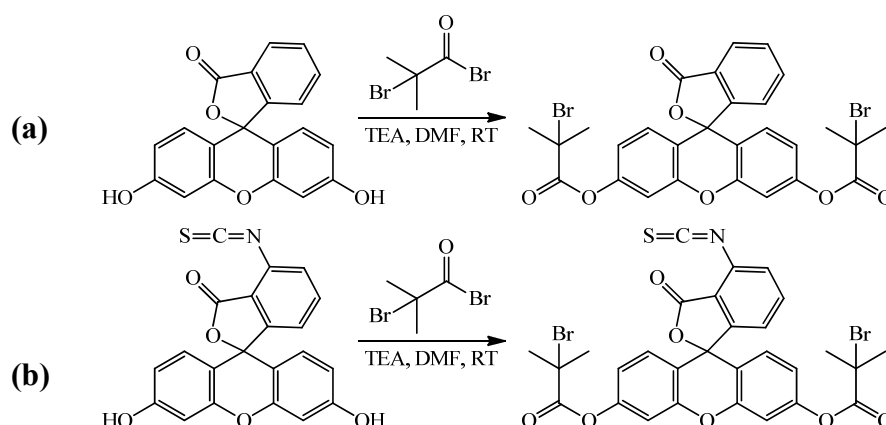


**Figure 2.2.** Reaction scheme for the synthesis of the bifunctional fluorescein-based ATRP initiators: (a) Fluo-Br and (b) FITC-Br.

### 2.2.3 Synthesis of hematoporphyrin dichloride (red dye)

Hematoporphyrin chloride was synthesized following a procedure reported in the literature.<sup>3</sup> In a dry 50 mL round bottom flask 19.8 mg (0.015 mmol) of hematoporphyrin dihydrochloride was added followed by the addition of 5 mL of dry DMF and 130.8  $\mu$ L (0.9 mmol) thionyl chloride. The reaction (Figure 2.3) was allowed to proceed under nitrogen for 5 hours in darkness and room temperature. The by-products ( $\text{SO}_2$ ,  $\text{HCl}$ ) were removed under reduced pressure and the resulting purple solid product was stored under nitrogen until use.

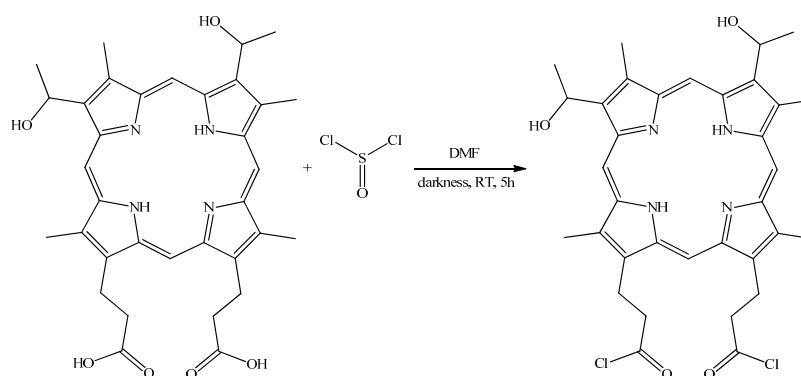


**Figure 2.3.** Schematic representation of the synthetic procedure followed for the synthesis of hematoporphyrin dichloride.

### 2.3 Atom transfer radical polymerization (ATRP) in bulk

In a dry 250 mL round-bottom flask the monomer, the ligand, the initiator and the catalyst (Cu salt) were added under dry nitrogen (Table 2.1). The system was degassed by three consecutive freeze-pump-thaw cycles and was immersed in a thermostatted bath at the required temperature. The polymerization kinetics were followed by withdrawing samples from the reaction mixture at predetermined time intervals followed by their characterization by  $^1\text{H}$  NMR and GPC.

**Table 2.1.** Amounts of reagents and temperature used for the ATRP of the monomers in bulk.

monomer		MMA		<i>t</i> BuA		DMAEMA	
	mol	0.20	0.65	0.34	0.48	0.48	
g	19.76	65.52	43.75	74.64	74.64		
initiator		<b>EBiB</b>	<b>Fluo-Br</b>	<b>EBiB</b>		<b>EBiB</b>	<b>EBiB</b>
	mmol	0.06	0.11	0.14	0.74	0.74	
mg	12.5	67.3	27.2	144.7	144.7		
ligand		<b>dNbp</b>	<b>dNbp</b>	<b>PMDETA</b>		<b>HMTETA</b>	<b>HMTETA</b>
	mmol	0.64	2.14	0.72	1.48	1.48	
mg	261.2	873.3	125.5	341.8	341.8		
metal salt		<b>Cu(I)Cl</b>	<b>Cu(I)Cl</b>	<b>Cu(I)Br</b>	<b>Cu(II)Br</b>	<b>Cu(I)Cl</b>	<b>Cu(I)Br</b>
	mmol	0.32	1.07	0.35	0.02	0.74	0.74
mg	31.6	105.8	50.0	4.0	73.4	106.4	
temperature	$^{\circ}\text{C}$	70	70	60		26	26

## 2.4 Synthesis of fully polymer-coated silica particles

### 2.4.1 Immobilization of the monofunctional ATRP initiator onto the surface of the silica particles

10 g of silica particles were dried in a high-vacuum oven at 120 °C overnight. Next, they were dispersed in dry DMF by mechanical agitation in order to obtain a 5 wt% silica dispersion. 0.33 g (1 mmol) of the monofunctional ATRP initiator was then transferred via a glass syringe in the particles dispersion and the reaction was allowed to proceed under nitrogen, at 30 °C for three days (Figure 2.4). The initiator-coated particles were isolated by centrifugation and were purified by 5 consecutive centrifugation and re-dispersion cycles in THF. The white solid obtained was dried under reduced pressure and was characterized by TGA before storage at room temperature until use.

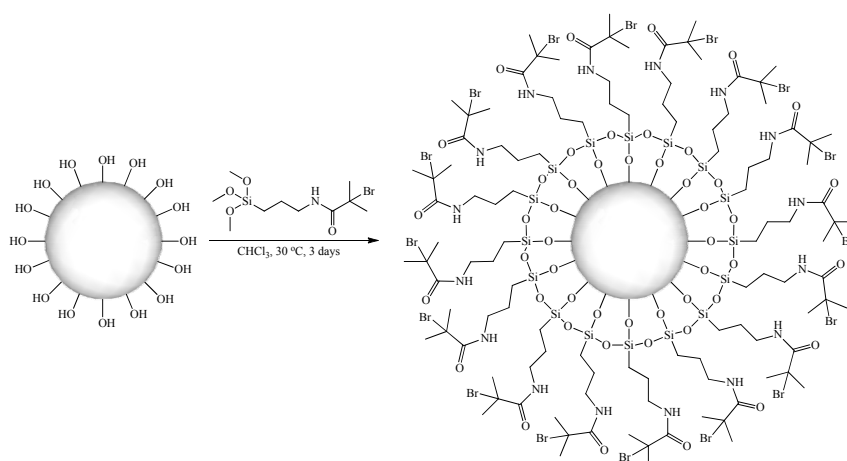


**Figure 2.4.** Reaction scheme for the immobilization of the monofunctional ATRP initiator onto the surface of the silica particles.

### 2.4.2 Immobilization of primary amine groups onto the surface of the silica particles

10 g of bare silica particles were dispersed in 400 mL of dry DMF followed by the addition of 0.3 mL (1.28 mmol) of APTES. The above mixture was stirred for three days at room temperature (Figure 2.5). Purification of the functionalized silica particles was carried out using five centrifugation-redispersion cycles (10,000 rpm for 30 min) in fresh ethanol. The presence of the amino groups onto the surface of the

silica particles was qualitatively verified by the ninhydrin test (formation of blue color in the presence of amine groups).

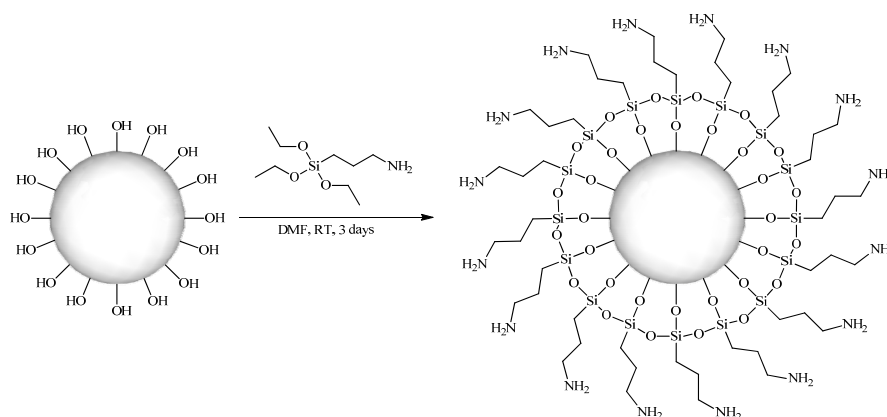


**Figure 2.5.** Reaction scheme for the functionalization of the silica particles with primary amine groups.

#### 2.4.3 Immobilization of the bifunctional ATRP initiator (FITC-Br) on the surface of the amine-functionalized silica particles

5 g of amine-functionalized silica particles were dispersed in 100 g DMF in order to obtain a 5 wt% silica suspension. Next, 0.5 g of freshly synthesized FITC-Br was added and the reaction was allowed to proceed overnight in dark. The FITC-Br functionalized particles were purified by five consecutive centrifugation-re-dispersion cycles in fresh THF and were dried under reduced pressure before characterization by TGA.

#### 2.4.4 Surface-initiated atom transfer radical polymerization (ATRP) for the formation of fully-coated particles

Before the polymerization, the initiator-coated particles dispersed in DMF were solvent-exchanged (5 cycles) with pure monomer to obtain a 2 wt % particle suspension in the monomer. A 100 mL round-bottom flask was charged with a predetermined amount of the particle suspension and prescribed amounts of monomer, ligand, catalyst (copper salt) and free initiator were added (Table 2.2). The system was immediately degassed by three freeze–pump–thaw cycles and subsequently sealed off under nitrogen. The polymerization (Figure 2.6) was carried out in a thermostatted bath under continuous stirring until highly viscous and was next

quenched by opening to air at room temperature. The reaction mixture was diluted with THF and was centrifuged to collect the polymer-grafted particles. This cycle of centrifugation and re-dispersion in fresh THF was repeated 8 times to obtain the purified polymer-grafted particles perfectly free of the unbound (free) polymer. The particles were dried under reduced pressure before characterization. The free polymer was analyzed by  $^1\text{H}$  NMR and next precipitated (in methanol for PMMA, in 9:1 methanol:water for *Pt*BuA and in hexane for PDMAEMA) and passed as a THF solution through a neutral alumina column in order to remove traces of copper before characterization by GPC.

Surface-initiated ATRP from the bifunctional initiator-coated silica particles was carried out under the same conditions.

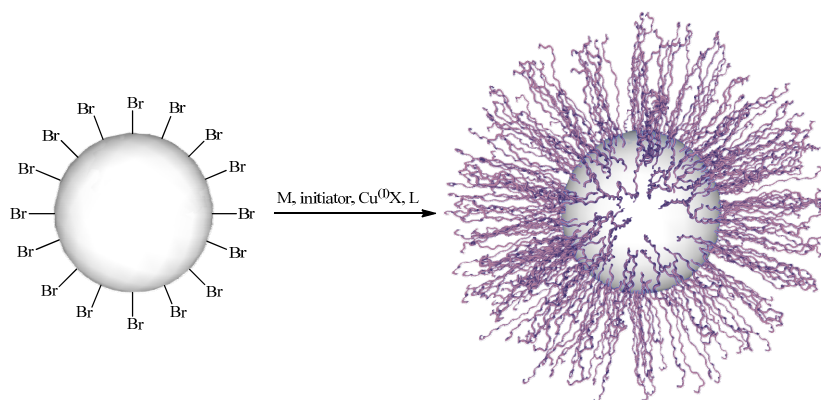


**Figure 2.6.** Reaction scheme of the surface-initiated ATRP for the synthesis of fully polymer-coated particles.

**Table 2.2.** Reagents and conditions employed for the synthesis of polymer brushes from the surface of the silica particles by ATRP.

	particles (g)	monomer		initiator		metal salt			ligand			T °C	t h		
		mol	(g)	mmol	mg	mmol	mg	mmol	mg						
Fully Coated (monofunctional initiator)	0.4	<b>MMA</b>	0.60	60.1	<b>EBiB</b>	0.10	20.5	<b>Cu(I)Cl</b>	1.05	104.0	<b>dNbpy</b>	2.10	858.8	70	7
	0.5	<b>tBuA</b>	0.67	86.1	<b>EBiB</b>	0.14	26.8	<b>Cu(I)Br</b>	0.69	68.3	<b>PMDETA</b>	1.43	247.0	60	24
								<b>Cu(II)Br</b>	0.03	7.8					48
0.36	<b>DMAEMA</b>	0.03	4.9	<b>EBiB</b>	-	-	<b>Cu(I)Cl</b>	0.10	10.0	<b>HMTETA</b>	0.20	46.0	26	14	
Fully Coated (bifunctional initiator)	1	<b>MMA</b>	1.22	122.2	<b>FluoBr</b>	0.10	62.8	<b>Cu(I)Cl</b>	1.99	197.2	<b>dNbpy</b>	3.98	1628.4	70	12 18
	0.5	<b>tBuA</b>	0.49	62.6	<b>FluoBr</b>	0.05	31.4	<b>Cu(I)Br</b>	0.05	71.5	<b>PMDETA</b>	0.52	108.2	60	240
								<b>Cu(II)Br</b>	0.03	5.7					
0.5	<b>DMAEMA</b>	0.13	21.5	<b>FluoBr</b>	0.05	31.4	<b>Cu(I)Cl</b>	0.20	19.7	<b>HMTETA</b>	0.40	91.8	26	40	
Janus	0.5	<b>MMA</b>	0.31	30.5	<b>FluoBr</b>	0.03	15.7	<b>Cu(I)Cl</b>	0.50	49.3	<b>dNbpy</b>	1.00	407.1	70	18
	0.4	<b>tBuA</b>	0.20	25.0	<b>FluoBr</b>	0.02	12.6	<b>Cu(I)Br</b>	0.20	28.6	<b>PMDETA</b>	0.21	43.3	60	72
								<b>Cu(II)Br</b>	0.01	2.3					
0.5	<b>DMAEMA</b>	0.06	10.7	<b>FluoBr</b>	0.03	15.7	<b>Cu(I)Cl</b>	0.10	9.9	<b>HMTETA</b>	0.20	45.9	26	40	

## 2.5 Synthesis of Janus polymer-silica particles

### 2.5.1 Synthesis of Janus particles using wax hybrid colloidosomes

Silica particle-stabilized paraffin-in-water emulsions were prepared following the protocol described by Giermanska-Kahn et al.<sup>4</sup> In a typical procedure (Figure 2.7), 1.3 g of silica particles were homogeneously dispersed in 100 mL of a selected solvent (water, methanol, ethanol, isopropanol or 1-octanol) and heated at 65°C. Since the silica particles are intrinsically hydrophilic, it was necessary to partially hydrophobize their surface in order to favor their adsorption at the oil–water interface. Therefore, 29 mg of hexadecyltrimethylammonium bromide (CTAB) was added into the particles suspension. Next, 10 g of wax with a narrow melting point (55-57 °C) was added in the particles suspension. After melting of the wax, the mixture was submitted to vigorous stirring by means of a Bosch MSM67 blender operating at 10,000 rpm for 80 s. The emulsion was allowed to cool down to room temperature in order to obtain solid droplets of paraffin wax. The specific functionalization of the unprotected surface of the silica particles on the wax droplet was carried out by directly adding APTES to the colloidosome suspension. After 12 h, the solid wax droplets were filtrated, washed several times with fresh solvent to remove unreacted APTES and the

wax was dissolved in warm chloroform. The resulting silica particles were collected by centrifugation and were washed with 8 consecutive centrifugation and redispersion cycles in fresh chloroform. The successful synthesis of the colloidosomes was verified by SEM.

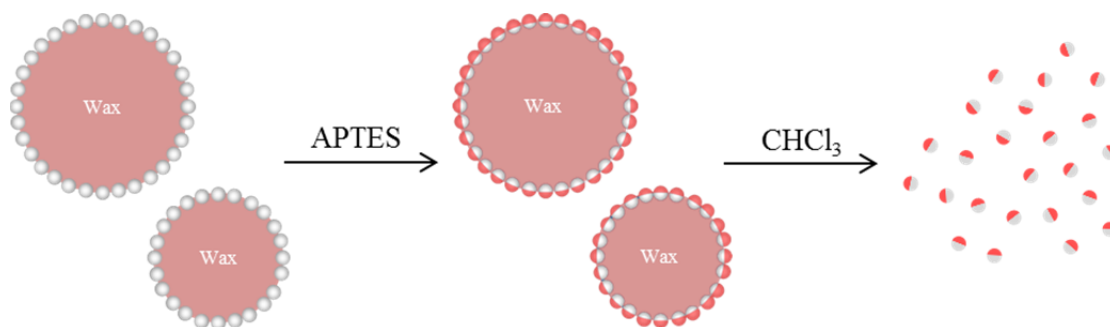


**Figure 2.7.** Schematic representation for the formation of amino functionalized Janus silica particles using wax colloidosomes.

### 2.5.2 Synthesis of polystyrene-silica (PS) hybrid colloidosomes

The silica stabilized polymer colloidosomes were synthesized by Pickering emulsion polymerization as follows. In a typical procedure, 17.24 mL (0.15 mol) styrene (St) monomer, 2.35 g amine-functionalized silica particles and 157 g methanol were added in turn to a 250 mL round bottomed flask under intense stirring. Next, 0.156 g (0.95 mmol) 2,2'-azobisisobutyronitrile (AIBN) initiator was added, and the reaction mixture was degassed with nitrogen prior to immersion in a 70 °C oil bath under a nitrogen blanket for 8 h (Figure 2.8). The resulting milky-white colloidal dispersion was purified by five consecutive sedimentation-re-dispersion cycles, with each successive supernatant being carefully decanted and replaced with fresh methanol. The formation of the colloidosomes was verified by SEM and TGA.

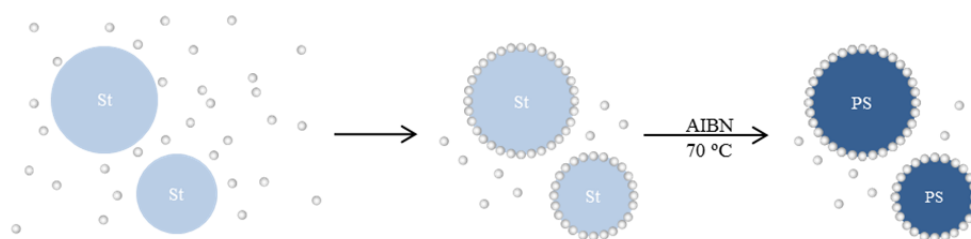


**Figure 2.8.** Reaction scheme for the formation of the PS colloidosomes via emulsion polymerization.

### 2.5.3 Synthesis of Janus colloidal initiator particles from the PS colloidosomes

In the above synthesized suspension of silica stabilized PS colloidosomes 78.7 mg of freshly synthesized FITC-Br was added. The reaction (Figure 2.9) was allowed to proceed overnight under vigorous stirring in the dark. Purification of the FITC-Br-functionalized colloidosomes was succeeded by eight consecutive sedimentation-re-dispersion cycles, with each successive supernatant being decanted and replaced with fresh methanol. The partially coated with FITC-Br ATRP initiator silica particles (J-FITCBr) were isolated by dissolving the PS colloidosomes in toluene followed by five centrifugation re-dispersion cycles in fresh toluene in order to remove all traces of polystyrene (Figure 2.10). The collected orange sediment was dried under reduced pressure and was kept in dark until use.

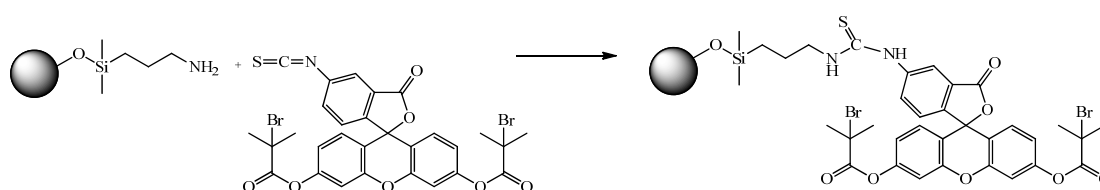


**Figure 2.9.** Reaction scheme for the covalent attachment of FITC-Br onto the exposed surface of the  $\text{NH}_2$ -functionalized silica particles.

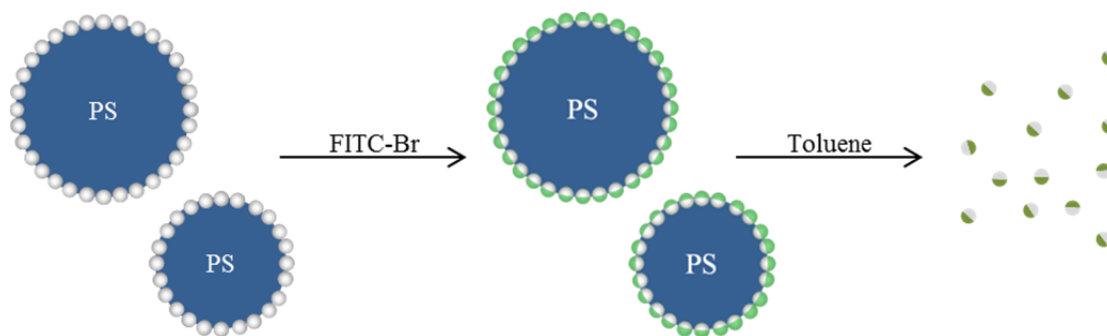


**Figure 2.10.** Formation of Janus FITC-Br and amine-functionalized silica particles.

#### 2.5.4 Immobilization of the red fluorescent dye onto the amine-functionalized surface of the Janus particles

In order to verify the Janus character of the above synthesized particles hematoporphyrin dichloride was used to dye the amine-functionalized surface of the particles (Figure 2.11). To achieve this, a 2 wt % suspension of the Janus (J-FITCBr) particles in 3 mL of DMF was added in a dry 25 mL round-bottom flask followed by the addition of 0.1 mL of TEA and 6.6 mg of freshly synthesized hematoporphyrin dichloride. The reaction was allowed to proceed overnight at room temperature. The dual-dyed particles were retrieved from the reaction mixture by five centrifugation-re-dispersion cycles in DMF. The brown sediment was dried under reduced pressure and was characterized by fluorescence microscopy.

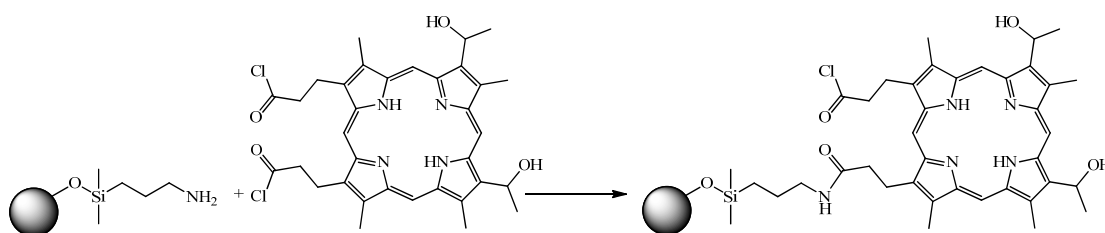


**Figure 2.11.** Reaction scheme for the immobilization of hematoporphyrin dichloride onto the amine-functionalized surface of the particles.

#### 2.5.5 Decoration of the amine-functionalized surface of the Janus particles with gold nanoparticles

The gold nanoparticles were synthesized by simply mixing 20 mL of a 0.25 nM  $\text{HAuCl}_4$ , 10 mL of a 0.1  $\mu\text{M}$  trisodium citrate solution and 10 mL of a 0.1  $\mu\text{M}$  sodium

borohydride aqueous solution. Next, a suspension of freshly synthesized gold nanoparticles was added to a dispersion of the Janus particles at low pH. Unbound gold nanoparticles were removed by 5 consecutive centrifugation-re-dispersion cycles in water. The purple sediment was characterized by TEM in order to verify the adsorption of the gold nanoparticles on the amine-functionalized surface of the Janus particles.

### **2.5.6 Surface-initiated ATRP from the initiator-functionalized surface of the Janus silica particles**

The Janus polymer-silica particles were prepared using a procedure similar to that described above for the fully polymer-coated particles with the Fluo-Br initiator. The Janus initiator-functionalized particles (J-FITCBr) were used as colloidal multi-initiators while the quantities of all utilized reagents (Table 2.2) were reduced by half, under the assumption that only half the surface of the particles is grafted with the initiating groups. The free polymers synthesized in solution were separately purified and characterized by GPC.

## **2.6 Deprotection of the *tert*-butyl acrylate polymer brushes**

*t*BuA is a protected ester which upon hydrolysis gives acrylic acid. Thus, after synthesis, the *Pt*BuA functionalized particles were deprotected by acid hydrolysis to obtain the PAA-functionalized particles. The hydrolysis was carried out in acidic media using trifluoroacetic acid (TFA) in dichloromethane. 100 mg of the *Pt*BuA-functionalized particles were dispersed in 10 mL dichloromethane and 10 fold molar excess (to the calculated number of *tert*-butyl groups present on the particles) of TFA was added. The reaction was allowed to proceed for 3 days before the hydrolyzed particles were purified by five consecutive centrifugation-re-dispersion cycles in fresh THF.

## **2.7 Characterization**

### **2.7.1 Thermogravimetric Analysis (TGA)**

Thermogravimetric analysis was performed on a Perkin Elmer Pyris Diamond TG/DTA instrument under a nitrogen atmosphere. For a typical measurement ~10 mg of solid sample were placed in a platinum holder and were heated under a constant nitrogen flow and a temperature ramp of 10 °C/min up to 900 °C. The data was analyzed using the Diamond Pyris software.

### **2.7.2 Gel Permeation Chromatography (GPC)**

The molecular weights and the molecular weight distributions were determined by gel permeation chromatography (GPC) utilizing a Thermo Finnigan chromatographer which included a TSP P1000 pump, two columns, Mixed-D and Mixed-E (Polymer Labs) and a refractive index (RI) detector (model ERC-RI 101). The software used for the analysis of the chromatograms was Atlas Workstation and Cirrus GPC Reanalysis Software. The eluent used was a THF:TEA (50:1) mixture at a 1 mL/min flow rate. The calibration curve was based on eight narrow molecular weight linear PMMA standards ranging from 850 to 342,900 g/mol. In a typical measurement a 2 wt% solution of the sample was prepared in THF/TEA (50:1) and was injected to the system (20µL) at a column temperature set to 40 °C.

### **2.7.3 Transmission Electron Microscopy (TEM)**

Samples for TEM were prepared by dispersing the particles in THF (0.01 %). Next, a drop of the diluted sample was placed on a carbon-coated copper grid (400 Mesh) and was left to dry in air overnight. A JEOL JEM-2100 instrument at an electron accelerating voltage of 80 kV was employed for the measurements.

### **2.7.4 Scanning Electron Microscopy (SEM)**

For a typical observation a 1 wt% dispersion of the sample in a good solvent was prepared and drop casted on a glass substrate. The sample was sputtered with gold to

obtain a uniform 10 nm film and avoid charging. The measurements were carried out utilizing a JEOL JSM-840 and a field emission JSM-7000F microscope operating at 10, 15, 20 or 30 kV.

### 2.7.5 Fluorescence Microscopy

For a typical fluorescence microscopy observation, a 0.1 wt% dispersion of the particles in DMF was prepared and a drop was placed between two glass slides. The instrument used was a Nikon Eclipse E800 microscope fitted with a B-2E/C filter (excitation, 450 to 490/510 nm) and a UV-2E/C filter (excitation, 330 to 380/485 nm). Images were captured by a Sony 655 DXC-950P camera.

### 2.7.6 Turbidimetry

A Lambda 25 Perkin-Elmer UV/vis spectrophotometer was used for the turbidity measurements. A 0.1 wt% dispersion of the particles was placed in a 10 mm path-length quartz cuvette containing a small magnetic bar, set in motion with the aid of a miniature magnetic stirrer. A small temperature probe was immersed in the upper part of the solution, which was heated from 20 to 85 °C. The optical density at 600 nm and the temperature were monitored using the UVWinLab (version 2.7) software. The cloud point was taken as the temperature where the first large increase in optical density occurred.

### 2.7.7 Dynamic Light Scattering (DLS)

The DLS measurements were carried out utilizing a custom-made system. The light source was an Adlas DPY 315 II Nd:YAG laser at a wavelength of 532 nm, polarized by two Glan-Thomson (Halle, Berlin) polarizers placed before and after the sample. A colorless lens was used to focus the beam onto the sample with a focal length of 200 mm. The scattered light is collected by an optical detector utilizing a 2F/2F system. Two pinholes are used before the photomultiplier (Thorn EMI) to define the scattering volume. The photon correlation was performed by an ALV-5000/E photon correlator. The thermostatted sample cell is placed on a motor-driven precision goniometer which enables the photomultiplier detector to be moved

accurately from 11 ° to 150 ° scattering angle. The sample is placed in a toluene bath and its temperature is monitored by a thermostat. The resulting correlation functions were fitted with a stretched exponential function, Kohlrausch-Williams-Watts (KWW) from which the relaxation time was derived, and allowed to calculate the diffusion coefficient of the scatterer. The hydrodynamic diameters were calculated from the Stokes-Einstein equation:

$$D = \frac{k_B T}{6\pi\eta R}$$

where D is the diffusion coefficient,  $k_B$  is Boltzmann's constant, T is the absolute temperature,  $\eta$  is the viscosity and R the hydrodynamic radius of the spherical particle.

### 2.7.8 Static Light Scattering (SLS)

Static light scattering experiments were performed over an angular range from 16° to 150° corresponding to a scattering vector (q) in a range of  $0.0047 < q < 0.03264 \text{ nm}^{-1}$ . From the minimum of the scattered intensity located at  $qR=4.49$  the effective  $R_G$  was calculated:

$$R_G = \sqrt{\frac{3}{5}} R$$

### 2.7.9 Nuclear Magnetic Resonance (NMR)

$^1\text{H}$  NMR and  $^{13}\text{C}$  NMR measurements were performed on a Bruker DPX-300 at 300 MHz. The software used for the analysis of the spectra was XWINNMR and Mestre-C. In a typical measurement a 2 wt% solution of the sample was prepared in deuterated chloroform ( $\text{CDCl}_3$ ) and the solvent peak was used as reference.

- 
- (1) Tugulu, S. Arnold, A. Sielaff, I. Johnsson, K.; Klok, H.-A. *Biomacromolecules* **2005**, *6*, 1602-7.
  - (2) Lu, X. Zhang, L. Meng, L.; Liu, Y. *Polymer Bulletin* **2007**, *59*, 195-206.
  - (3) Maravin, G. B. Ponomarev, G. V.; Shul'ga, A. M. *Chemistry of Heterocyclic Compounds* **1987**, 214-220.

- (4) Giermanska-Kahn, J. Laine, V. Arditto, S. Schmitt, V.; Leal-Calderon, F.  
*Langmuir* **2005**, *21*, 4316-23.

## Chapter 3 | Results and Discussion

### 3.1 Bare silica particles

#### 3.1.1 Dynamic Light Scattering (DLS)

The hydrodynamic size of the silica particles in ethanol was determined by DLS measurements. The single exponential decay of the autocorrelation functions and the linear increase of the decay rates implied well dispersed particles with uniform size (Figure 3.1). The diffusion coefficient of the single process was found to be  $1.39 \cdot 10^{-12} \text{ m}^2/\text{s}$  which corresponds to a hydrodynamic diameter of 247 nm.

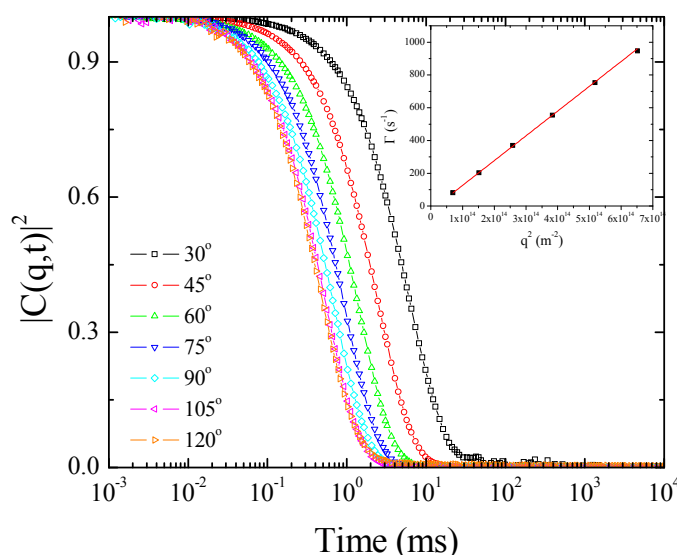


**Figure 3.1.** Intensity autocorrelation functions of the bare silica particles in ethanol at different scattering angles. Inset: Decay rates of the autocorrelation functions ( $\Gamma$ ) as a function of the square wavevector ( $q^2$ ).

#### 3.1.2 Scanning and Transmission Electron Microscopy (SEM and TEM)

Scanning electron microscopy verified the spherical shape of the bare silica particles as well as their uniform size (Figure 3.2). The smoothness of the surface of the particles was also noted. Transmission electron microscopy also verified the uniform size and shape of the bare silica particles (Figure 3.3).

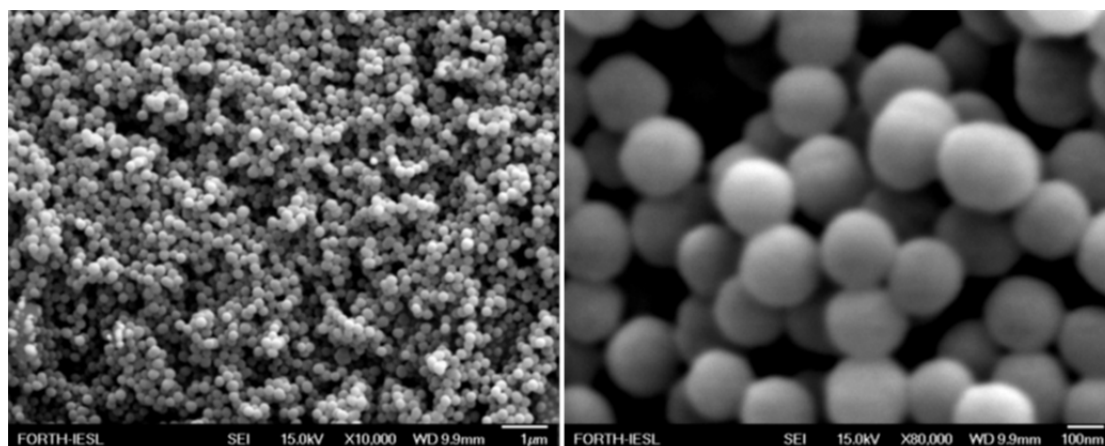


**Figure 3.2.** SEM images of the bare silica particles at different magnifications.

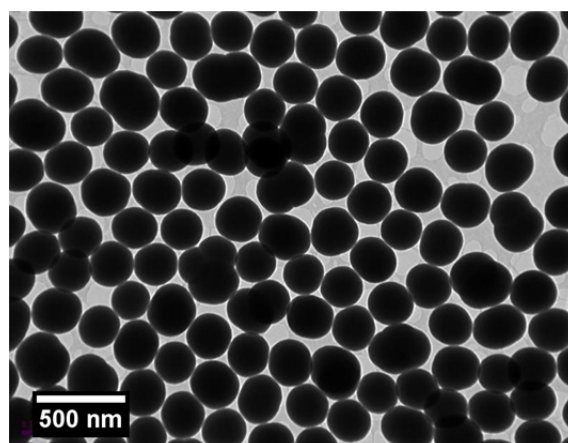


**Figure 3.3.** TEM image of the bare silica particles.

## **3.2 Synthesis of the ATRP initiators**

### **3.2.1 Synthesis of the monofunctional surface-bound ATRP initiator 3-(2-bromoisobutyramido)propyl(trimethoxy) silane**

The synthesis of the monofunctional initiator 3-(2-bromoisobutyramido)propyl(trimethoxysilane) was achieved by the condensation reaction of 3-aminopropyltrimethoxysilane with  $\alpha$ -bromoisobutyryl bromide in the presence of triethylamine. The product was characterized by  $^1\text{H}$  NMR in  $\text{CDCl}_3$ . The following spectrum (Figure 3.4) shows the characteristic peaks of the initiator and verifies its successful synthesis.

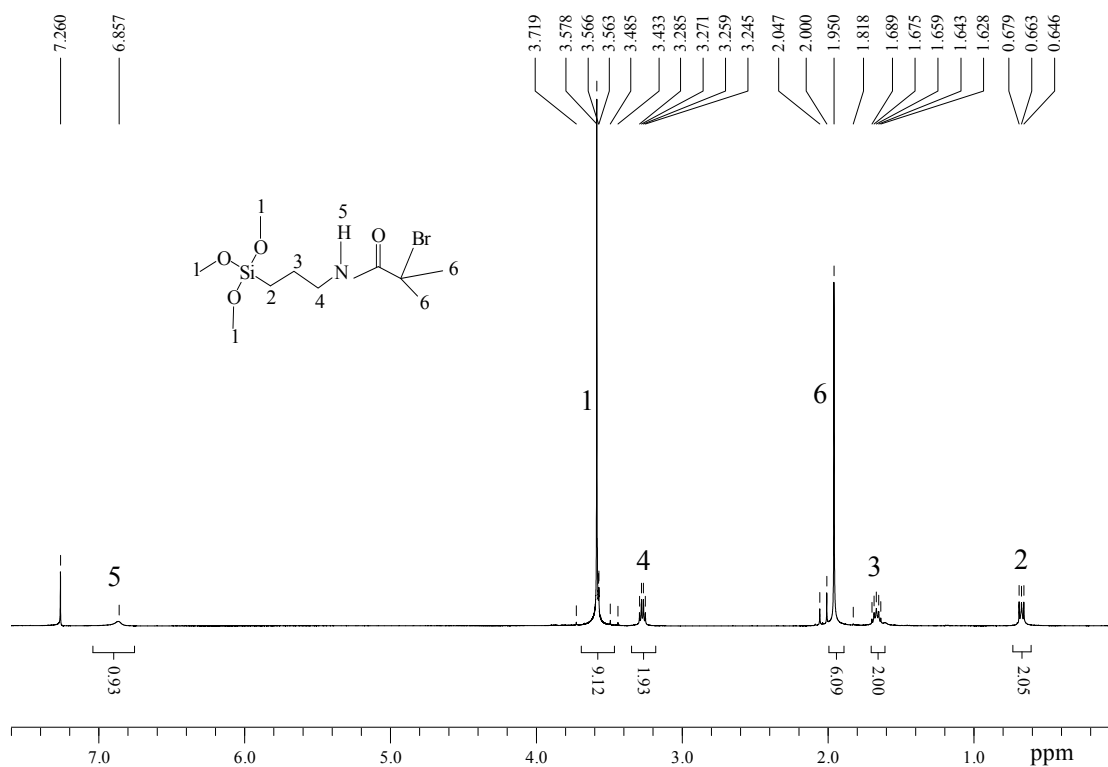


**Figure 3.4.**  $^1\text{H}$  NMR of the monofunctional ATRP initiator 3-(2-bromoisobutyramido)propyl(trimethoxy)silane.

$^1\text{H}$  NMR (500 MHz,  $\text{CDCl}_3$ )  $\delta$  (ppm) 6.86 (1H), 3.56 (9H), 3.26 (2H), 1.95 (6H), 1.66 (2H), 0.66 (2H). The presence of the peak at 1.95 ppm which corresponds to the protons of the two methyl groups next to the bromine atom as well as the appearance of the peak corresponding to the amide proton at 6.86 ppm verified the successful synthesis of the initiator. Moreover, a shift of the peak which corresponds to the two protons of the methylene group next to the nitrogen atom is observed from 2.64 to 3.26 ppm verifying the amide bond formation. Integration of the NMR peaks indicate the presence of 9 methoxy protons at 3.56 ppm and thus verifies the prevention of the hydrolysis of the methoxy silane groups during the initiator synthesis and purification steps. This is important since it is these methoxy groups that will hydrolyze and condense with the surface hydroxy silane groups allowing to bind the initiator onto the surface of the silica particles.

### 3.2.2 Synthesis of the bifunctional ATRP initiator 3-oxo-3H-spiro[isobenzofuran-1,9'-xanthene]-3',6'-diyl bis(2-bromo-2-methylpropanoate) (Fluo-Br)

The synthesis of the bifunctional ATRP initiator was achieved via the esterification reaction of the two phenol groups of fluorescein with  $\alpha$ -bromoisobutyryl bromide in the presence of triethylamine. The product was characterized by  $^1\text{H}$  NMR (Figure 3.5) in  $\text{CDCl}_3$  in order to verify the successful synthesis.

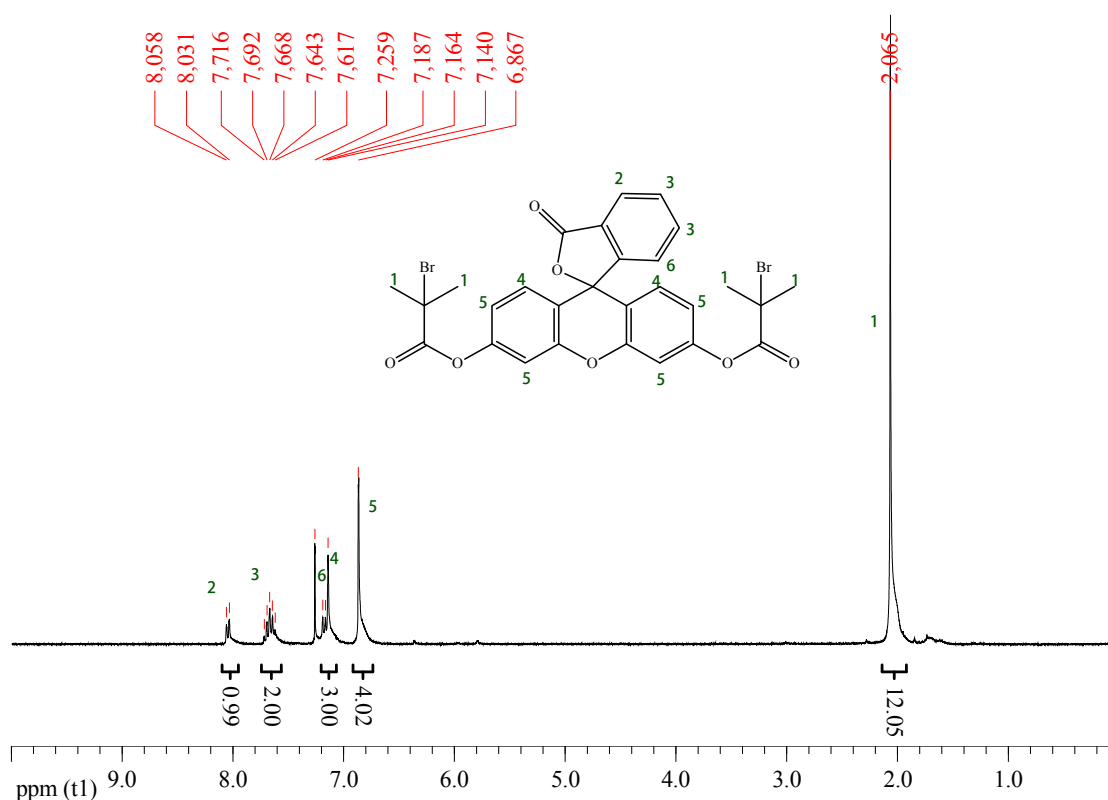


**Figure 3.5.**  $^1\text{H}$  NMR spectrum of the Fluo-Br bifunctional ATRP initiator 3-oxo-3H-spiro[isobenzofuran-1,9'-xanthene]-3',6'-diyl bis(2-bromo-2-methylpropanoate).

$^1\text{H}$  NMR (300 MHz,  $\text{CDCl}_3$ )  $\delta$  (ppm) 8.04 (1H), 7.70 (2H), 7.19 (1H), 7.15 (2H), 6.87 (4H), 2.07 (12H). The presence of the peak at 2.07 ppm which corresponds to the protons of the methyl groups next to the bromine atom indicates the successful synthesis of the initiator. This is also supported by the shift of the peaks corresponding to the protons of the phenyl groups adjacent to the formed ester group from 6.55 and 6.68 to 6.87 ppm. The peak integrals verify the synthesis of the

bifunctional species and the absence of monofunctionalized fluorescein initiator molecules.

The above results were also supported by  $^{13}\text{C}$  NMR spectroscopy (Figure 3.6).

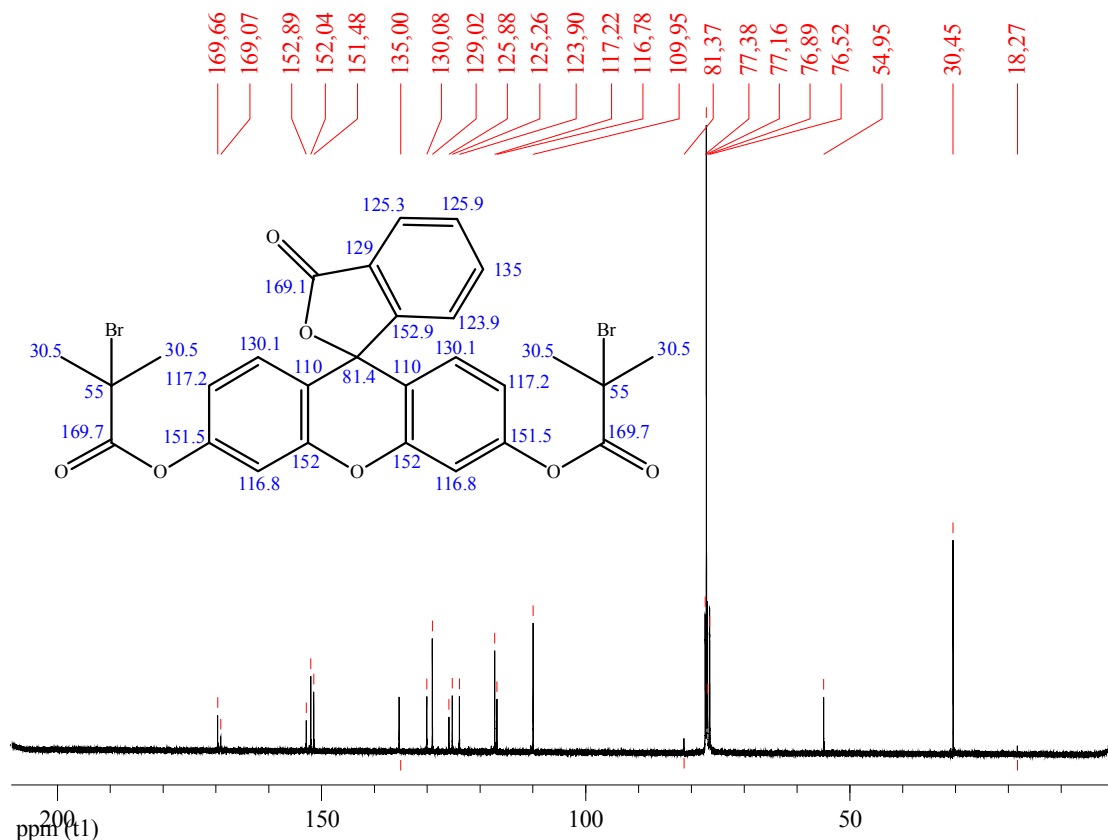


**Figure 3.6.**  $^{13}\text{C}$  NMR spectrum of the synthesized Fluo-Br bifunctional ATRP initiator 3-oxo-3H-spiro[isobenzofuran-1,9'-xanthene]-3',6'-diyl bis(2-bromo-2-methylpropanoate).

$^{13}\text{C}$  NMR (300 MHz,  $\text{CDCl}_3$ )  $\delta$  (ppm) 30.5, 55.0, 81.4, 110.0, 116.8, 117.2, 123.9, 125.3, 125.9, 129.0, 130.1, 135.0, 151.5, 152.0, 152.9, 169.1, 169.7. The presence of a peak at 30.5 ppm, attributed to the methyl carbons next to the bromine group, verified the successful synthesis of the initiator. This is also confirmed by the appearance of an extra peak at 169.7 ppm attributed to the carbonyl group of the ester. Moreover, the disappearance of the peak at 105 ppm, corresponding to the carbon adjacent to the hydroxyl group, confirms the absence of non-functionalized hydroxyl groups.

### 3.2.3 Synthesis of the surface-bound bifunctional ATRP initiator 4-isothiocyanato-3-oxo-3H-spiro[isobenzofuran-1,9'-xanthene]-3',6'-diyl bis(2-bromo-2-methylpropanoate) (FITC-Br)

The FITC-Br was synthesized using a similar procedure to that employed for the Fluo-Br initiator, by the esterification reaction of the two hydroxyl groups of FITC with  $\alpha$ -bromoisobutyryl bromide in the presence of triethylamine. The following  $^1\text{H}$  NMR spectrum (Figure 3.7) verifies its successful synthesis.

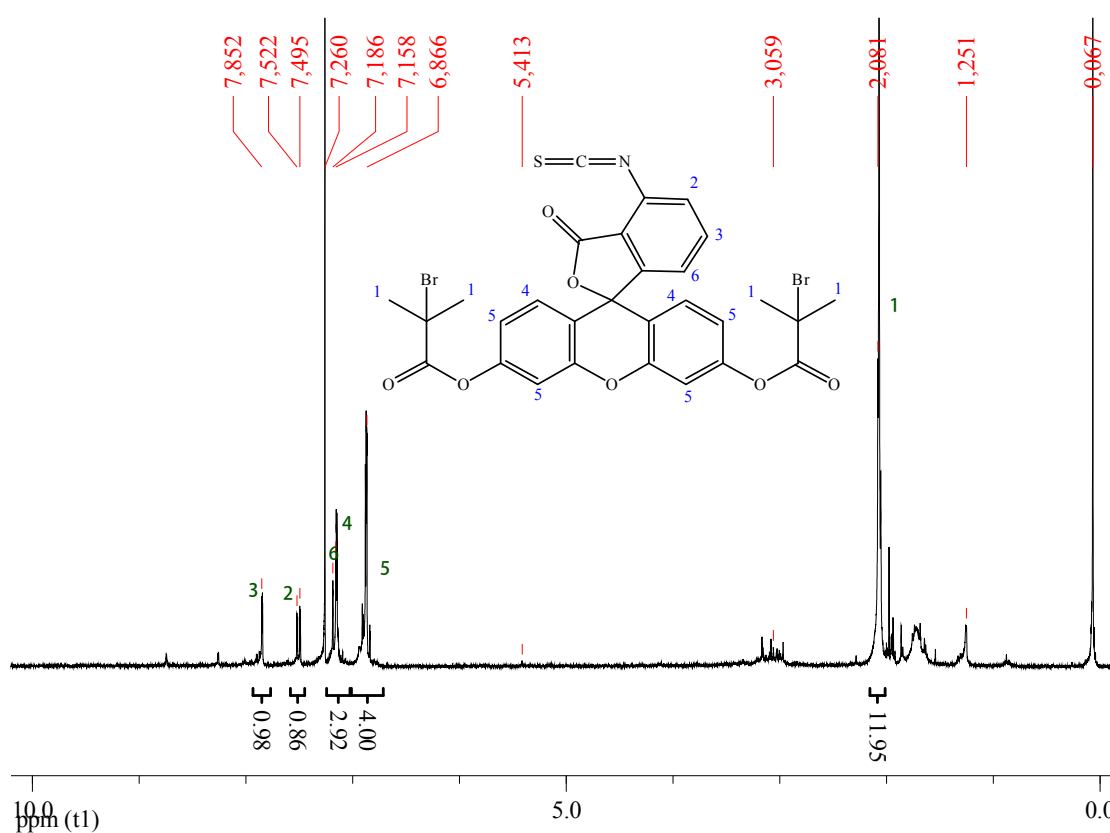


**Figure 3.7.**  $^1\text{H}$  NMR spectrum of the synthesized FITC-Br surface-bound bifunctional ATRP initiator.

$^1\text{H}$  NMR (300 MHz,  $\text{CDCl}_3$ )  $\delta$  (ppm) 7.85 (1H), 7.52 (1H), 7.19 (1H), 7.16 (2H), 6.87 (4H), 2.08 (12H). The presence of a peak at 2.08 ppm is attributed to the methyl protons next to the bromine group and indicates the successful synthesis of the initiator. In addition to that, the shift of the peaks corresponding to the phenyl protons adjacent to the hydroxyl groups 6.67 and 6.73 to 6.87 ppm support the complete transformation of the latter to the ester moieties. The peak integrals agree with the theoretical structure verifying the successful synthesis. The peaks at 3.06 ppm and

1.25 ppm are attributed to the triethylammonium bromide salt produced from the reaction.

The findings by  $^1\text{H}$  NMR spectroscopy were also verified by the following  $^{13}\text{C}$  NMR spectrum of the FITC-Br initiator (Figure 3.8).

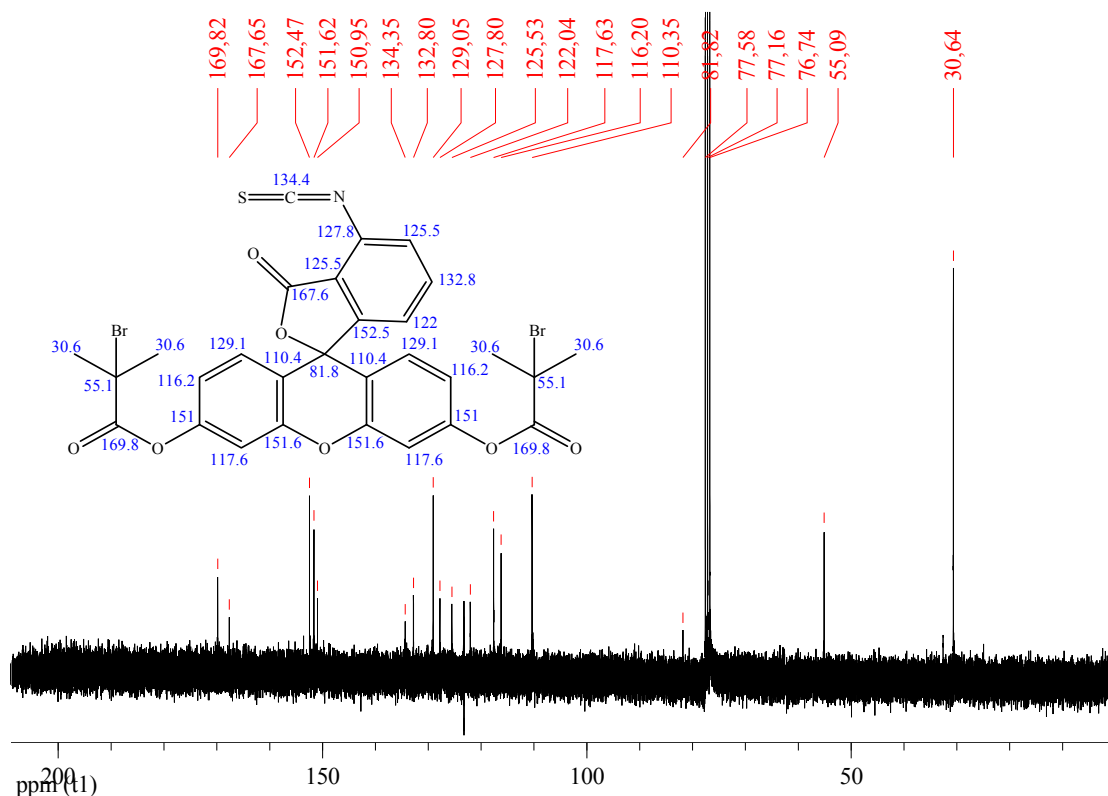


**Figure 3.8.**  $^{13}\text{C}$  NMR spectrum of the synthesized FITC-Br bifunctional surface-bound ATRP initiator.

$^{13}\text{C}$  NMR (300 MHz,  $\text{CDCl}_3$ )  $\delta$  (ppm) 30.6, 55.1, 81.8, 110.4, 116.2, 117.6, 122.0, 125.5, 127.8, 129.1, 132.8, 134.4, 151.0, 151.6, 152.5, 167.6, 169.8. The peak at 30.6 ppm is attributed to the methyl carbons next to the bromine group and verifies the successful synthesis of the initiator. Moreover, the appearance of a carbonyl carbon peak at 169.8 ppm confirms the successful esterification of  $\alpha$ -bromoisobutyryl bromide with the hydroxyl groups of FITC to form an ester bond. The absence of a peak at 105 ppm indicates the successful transformation of all hydroxyl groups to ester moieties.

### **3.3 NH<sub>2</sub>- and ATRP initiator-functionalized silica particles**

#### **3.3.1 Primary amino group functionalized silica particles**

First the silica particles were functionalized with a self-assembled monolayer of APTES. The successful grafting of APTES onto the surface of the silica particles was qualitatively verified by the ninhydrin test. As shown in Figure 3.9, a dispersion of the APTES-functionalized silica particles turned blue when boiled at the presence of ninhydrin. In contrast, a dispersion of the bare silica nanoparticles under the same conditions was yellow. The blue pigmentation is indicative of the presence of primary amine groups in the solution,<sup>1</sup> thus verifying the successful grafting of APTES onto the surface of the particles.

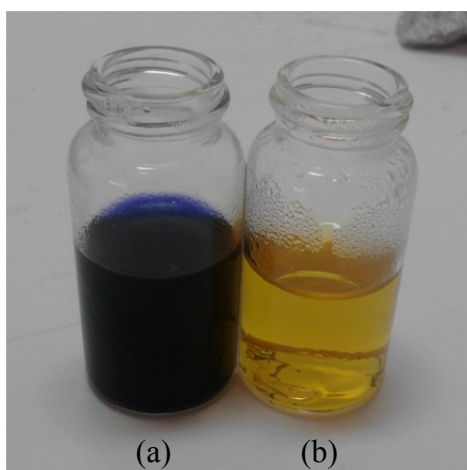


**Figure 3.9.** APTES-modified (a) and bare (b) silica nanoparticles subjected to the ninhydrin test.

#### **3.3.2 ATRP initiator-coated silica particles**

The monofunctional initiator was attached onto the surface of the silica particles by the hydrolysis and condensation of the methoxy groups with the surface hydroxyl silane groups. The bifunctional initiator was tethered on the silica particles by the coupling reaction of the isothiocyanate group with the amino moieties on the surface of the APTES-functionalized particles. The initiator-coated particles were characterized by TGA as shown in Figure 3.10. The particles grafted with the monofunctional initiator (FCA) exhibited a 10.7 % weight loss, while the particles

grafted with the bifunctional initiator (FCF) showed a 12.6 % weight loss. Both weight losses were attributed to the thermal decomposition of the organic content of the initiators. The weight loss in each case is determined by the molecular weight of the initiator and its grafting density onto the particle surface.

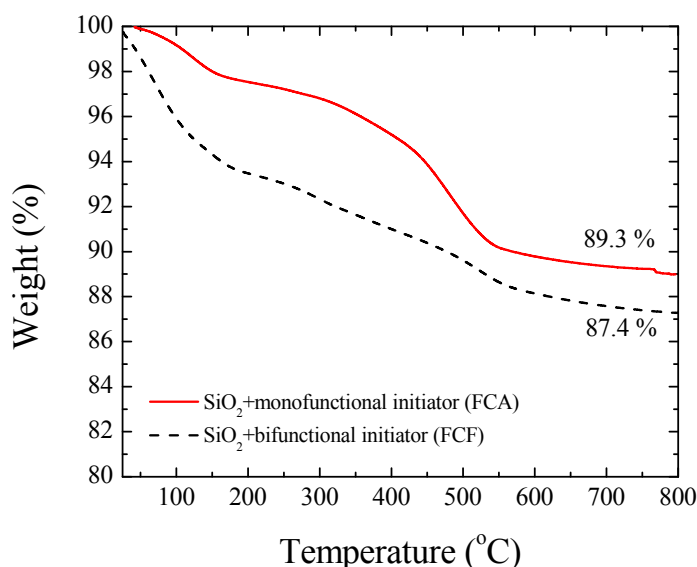


**Figure 3.10.** Thermograms of the initiator coated silica particles.

The FITC-Br functionalized particles (FCF) were characterized by DLS in order to determine their hydrodynamic size. A single exponential decay of the autocorrelation function was observed, while the autocorrelation decay rate increased in a linear fashion over  $q^2$ , indicating uniform size particles and the absence of aggregates (Figure 3.11). The diffusion coefficient of the particles in DMF derived from the linear fit of the intensity autocorrelation decay rates was found to be  $1.976 \cdot 10^{-12} \text{ m}^2/\text{s}$  which according to the Stokes-Einstein equation corresponds to a hydrodynamic diameter of 236 nm. Although this value is slightly smaller than the diameter calculated for the bare silica particles in ethanol, it will be used as a reference for the further results on the polymer-coated particles since DMF was the solvent chosen for most measurements.

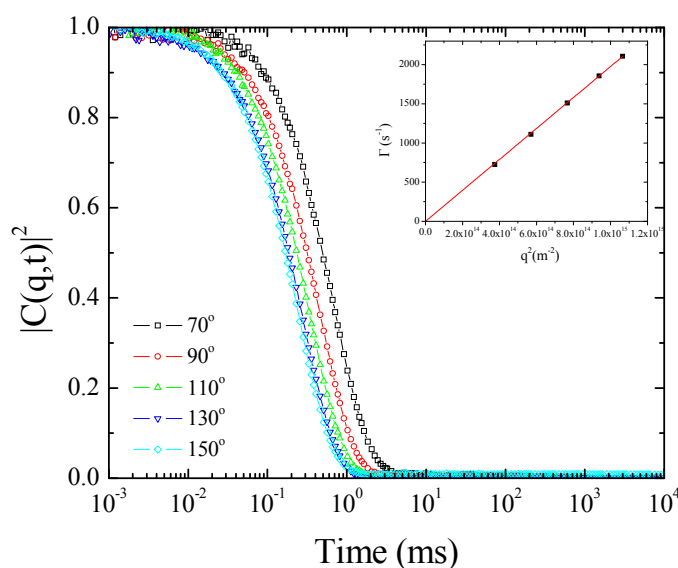


**Figure 3.11.** Intensity autocorrelation functions of the FITC-Br functionalized particles in DMF. Inset: Decay rates as a function of the square wavevector.

### 3.4 Colloidosomes

#### 3.4.1 Wax-silica hybrid colloidosomes

The synthesis of the wax-silica hybrid colloidosomes was achieved by the vigorous stirring of molten wax and the solvent at the presence of the silica particles. Upon cooling of the emulsion, the wax was solidified and the silica particles were trapped into the wax-solvent interface.

##### *(i) Wax-silica hybrid colloidosomes synthesized in methanol*

The bare silica particles were utilized to stabilize an emulsion of molten wax in methanol. The solidified wax-silica droplets were observed by SEM in order to verify the successful formation of the hybrid colloidosomes. Figure 3.12 shows the successful deposition of the silica particles onto the surface of the wax microspheres. However, the formation of multilayers of the silica particles is evidenced while unbound particles are also observed. The silica particles embedded in the wax surface cannot be determined due to the formation of multiple layers of silica particles onto the surface of the wax microparticles. Such multiple particle layers would result in a

much higher exposed surface area for the silica particles which will prohibit the formation of Janus particles.

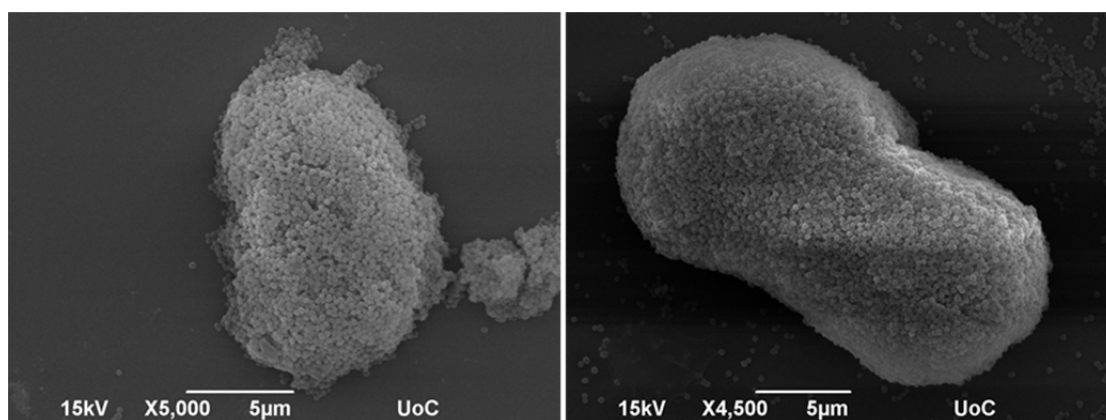


**Figure 3.12.** SEM images of the wax hybrid colloidosomes synthesized in methanol.

*(ii) Wax-silica hybrid colloidosomes synthesized in ethanol*

Ethanol was also utilized as the continuous phase in the formation of a wax emulsion stabilized by the bare silica particles. Figure 3.13 shows the hybrid structures formed as observed by SEM. Although some particles seem to be embedded in the surface of the wax microparticles, the failure to form stable colloidosomes is apparent. In fact, a mixture of the two components of irregular shapes and compositions is observed. Therefore, ethanol was also considered unsuitable for the successful synthesis of Janus particles.

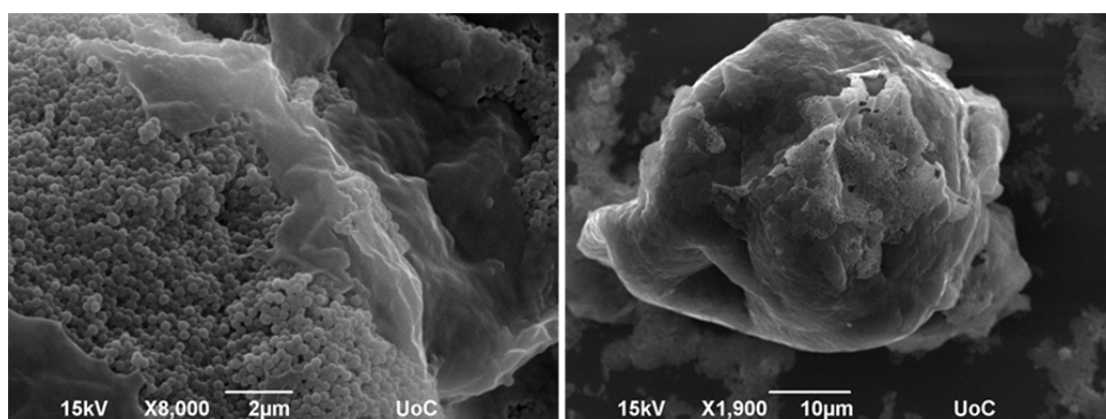


**Figure 3.13.** SEM images of the wax hybrid colloidosomes synthesized in ethanol.

*(iii) Wax-silica hybrid colloidosomes synthesized in isopropanol*

SEM was also employed for the observation of the wax hybrid colloidosomes synthesized in isopropanol as shown in Figure 3.14. The diversity of the sample was evidenced by the presence of multilayers of silica particles on the surface of the wax microparticles together with unbound silica particles, as well as by the presence of uncoated wax microparticles (Figure 3.14). The inability of the bare silica particles to form a monolayer embedded in the surface of the wax microparticles indicates the unsuitability of isopropanol as the continuous phase for the formation of the hybrid colloidosomes.

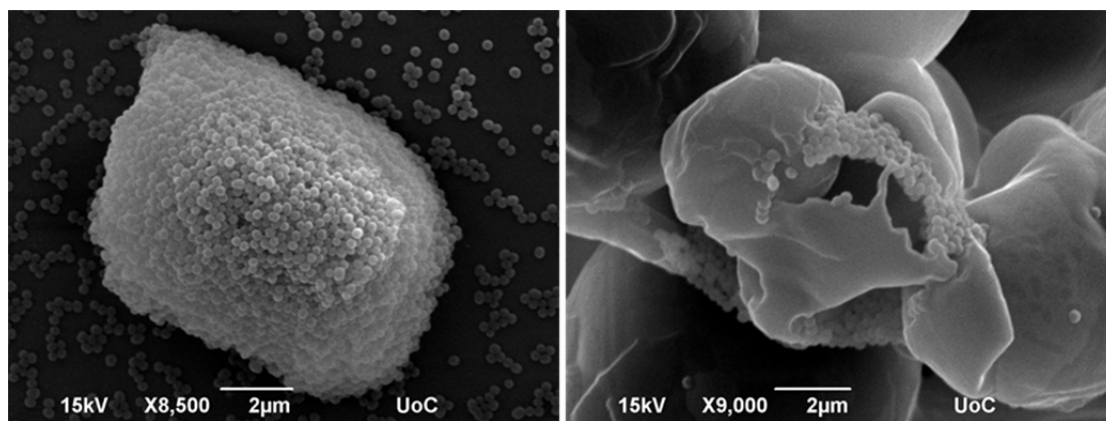


**Figure 3.14.** SEM images of the wax hybrid colloidosomes synthesized in isopropanol.

*(iv) Wax-silica hybrid colloidosomes synthesized in 1-octanol*

1-octanol was also utilized for the synthesis of wax-silica hybrid colloidosomes and the resulting hybrids were observed by SEM. As seen in Figure 3.15 the stabilization of wax microparticles by the bare silica particles was accomplished to some extent. However, the presence of unbound silica particles as well as the presence of bare wax indicates that the immobilization of the silica particles in the interface of wax and 1-octanol is not favored. Thus, 1-octanol was also considered to be unsuitable for the synthesis of the wax hybrid colloidosomes to be used for the synthesis of the Janus particles.

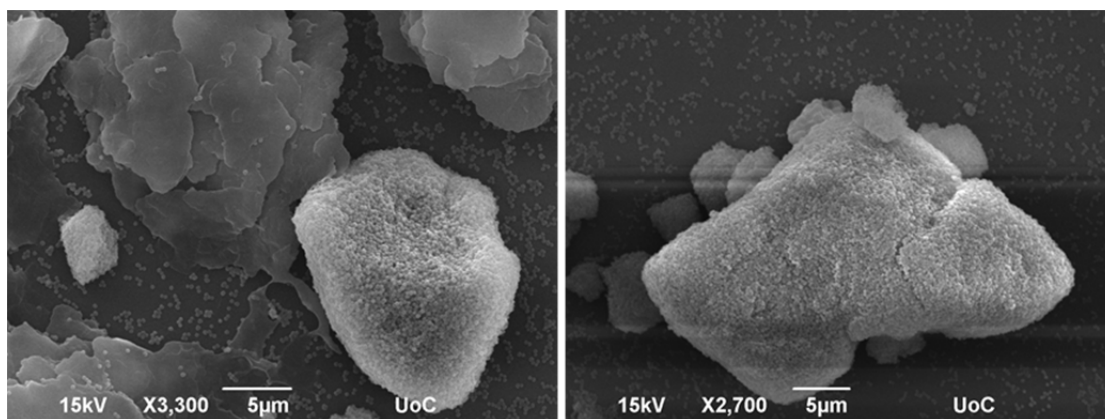


**Figure 3.15.** SEM images of the wax hybrid colloidosomes synthesized in 1-octanol.

*(v) Wax-silica hybrid colloidosomes synthesized in water*

Last, the bare silica particles were rendered hydrophobic by the use of a cationic surfactant in water.<sup>2</sup> The positively charged surfactant adsorbs onto the surface of the negatively charged silica particles due to electrostatic interactions exposing the alkyl chains to the solution, thus rendering the particles hydrophobic. The wax hybrid colloidosomes formed by the hydrophobized silica particles in water were observed by SEM (Figure 3.16). The successful synthesis of the hybrid colloidosomes was verified by the presence of spherical wax microparticles on the surface of which the silica particles were embedded. Although the colloidosomes are not homogeneous in terms of size and surface coverage, since the conditions utilized were not optimized, they are suitable for the formation of Janus particles. This is due to the fact that all the silica particles were embedded into the surface of the wax microparticles, while only a small number of unbound particles were observed and no multilayers of silica particles were found.

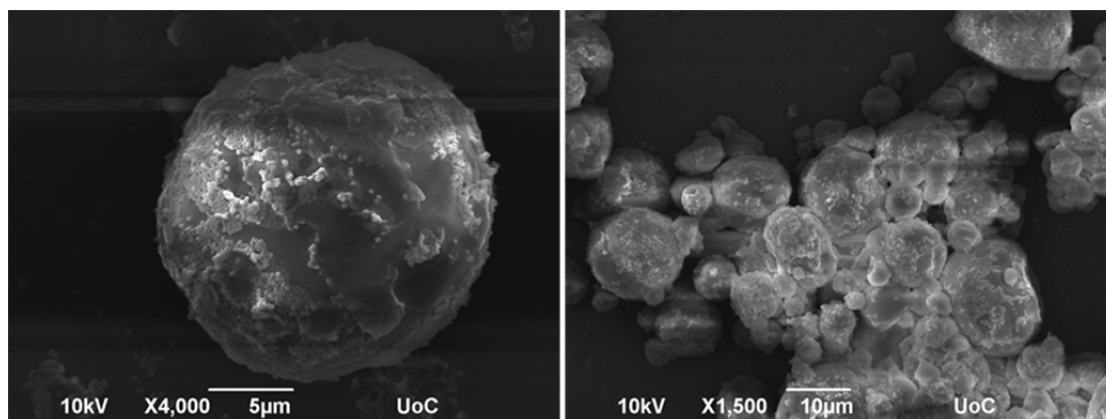


**Figure 3.16.** SEM images of the wax hybrid colloidosomes synthesized in water.

The effectiveness of the silica particles to emulsify the wax droplets was evaluated by TGA. As shown in Figure 3.17, a 95 % weight loss was found, attributed to the decomposition of the wax. This value is higher than the anticipated one (88.5 %) which is attributed to the unbound particles that were filtered out during the washing procedure of the wax colloidosomes.

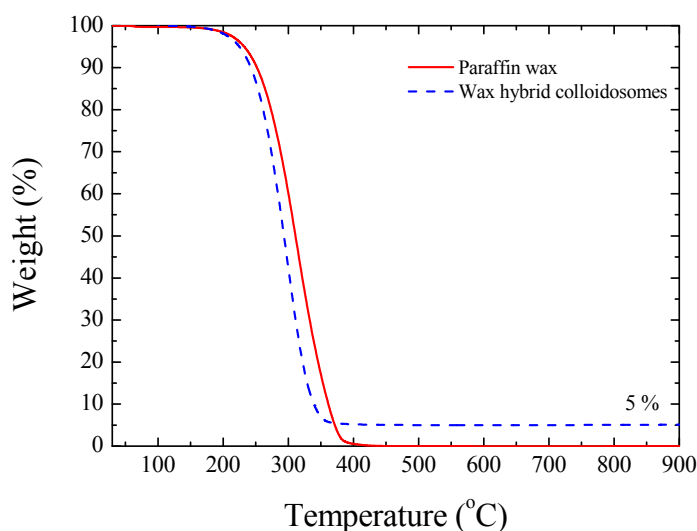


**Figure 3.17.** Thermogram of the wax hybrid colloidosomes compared to that of pure paraffin wax.

For the second step of the synthesis of the Janus particles, a dispersion of the wax hybrid colloidosomes prepared in water, was mixed with APTES. In this way, the exposed surface of the silica particles will react with the triethoxy group of APTES, to decorate it with primary amino groups, while the wax-embedded surface of the

particles will retain its hydroxy functionalities. Following this reaction, the APTES-modified wax hybrid colloidosomes were observed by SEM (Figure 3.18). Although the spherical shape of the wax microparticles was maintained, the majority of the wax surface was found bare of silica particles while presenting a holey pattern. This was attributed to the desorption of the silica particles from the surface of the wax microparticles during the reaction with APTES. The presence of unbound silica particles verified their desorption from the wax microparticles surface. The fact that an excess amount of APTES was used for the modification of the surface of the silica particles, together with the fact that the particles desorb from the colloidosomes are expected to result in a random grafting of APTES over the whole surface of the silica particles resulting in particles fully coated with the amine groups. This suggests that the wax colloidosomes are unsuitable for the synthesis of the Janus particles.

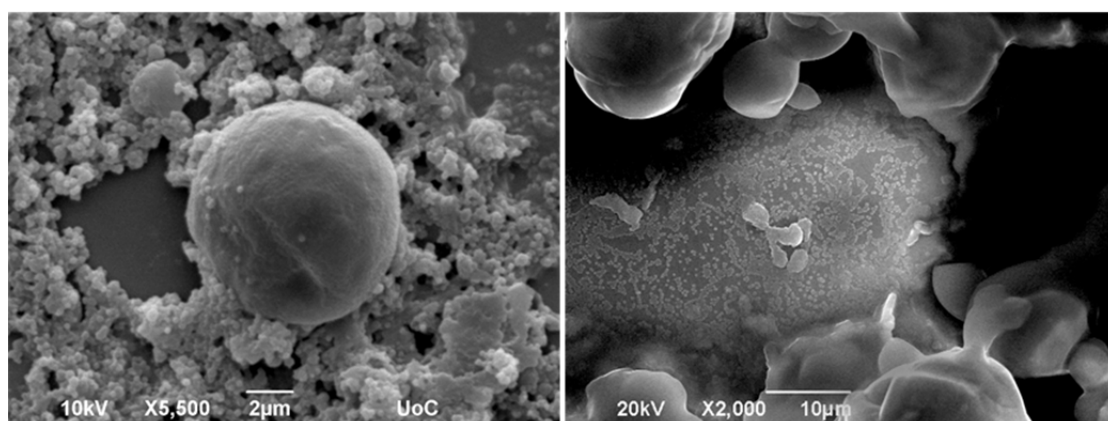


**Figure 3.18.** SEM images of the wax hybrid colloidosomes synthesized in water after modification of the exposed hydroxyl groups on the surface of the silica particles with APTES.

### 3.4.2 Polystyrene-silica hybrid colloidosomes

#### *(i) Synthesis of the PS-SiO<sub>2</sub> hybrid colloidosomes*

In order to successfully synthesize hybrid colloidosomes for the formation of Janus particles a different pathway was chosen which involves the emulsion polymerization of styrene in the presence of silica particles in methanol in order to form PS solid droplets emulsified by the silica particles. The silica particles utilized as the stabilizing entities were amine-functionalized prior to the synthesis of the colloidosomes with APTES in order to improve the particle-styrene affinity.<sup>3</sup> The

successful synthesis of the hybrid colloidosomes was verified by SEM as shown in Figure 3.19. Spherical polymeric microparticles were observed throughout the sample while the silica particles were embedded into the surface of the PS microparticles. A small amount of bare PS surface was observed and was attributed to the non-optimized synthetic conditions in terms of styrene/silica feed ratio. However, the lack of unbound silica particles as well as the absence of multilayers of silica particles on the surface of the PS particles rendered these PS-silica hybrid colloidosomes attractive candidates for the synthesis of the Janus particles.

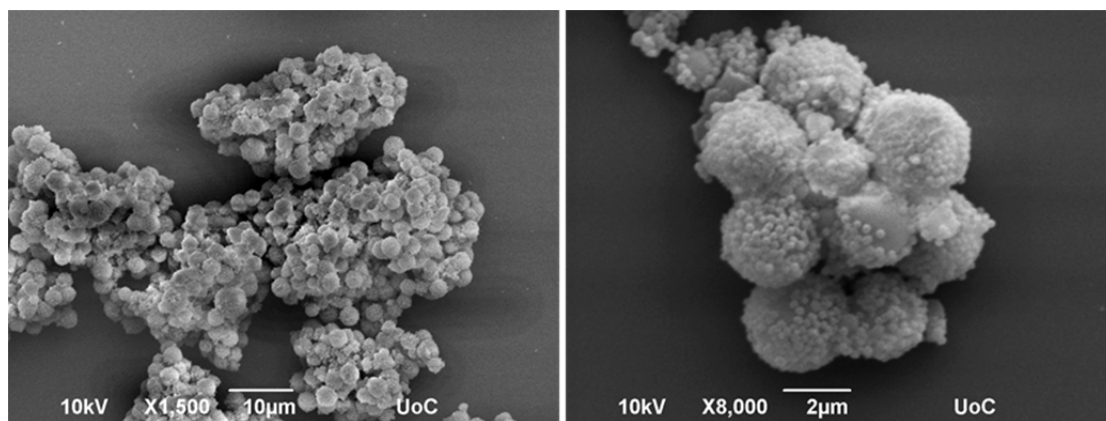


**Figure 3.19.** SEM images of the PS-SiO<sub>2</sub> hybrid colloidosomes synthesized in methanol.

The synthesized PS-SiO<sub>2</sub> hybrid particles were analyzed by TGA in order to quantify the amount of silica particles adsorbed onto the surface of the PS microparticles. Figure 3.20 shows a 74 % weight loss attributed to the decomposition of PS while the remaining 26 % is attributed to the silica particles. This value is higher than that anticipated from the monomer/silica feed ratio (13 %) which was attributed to the lower conversion of the styrene monomer during the polymerization.

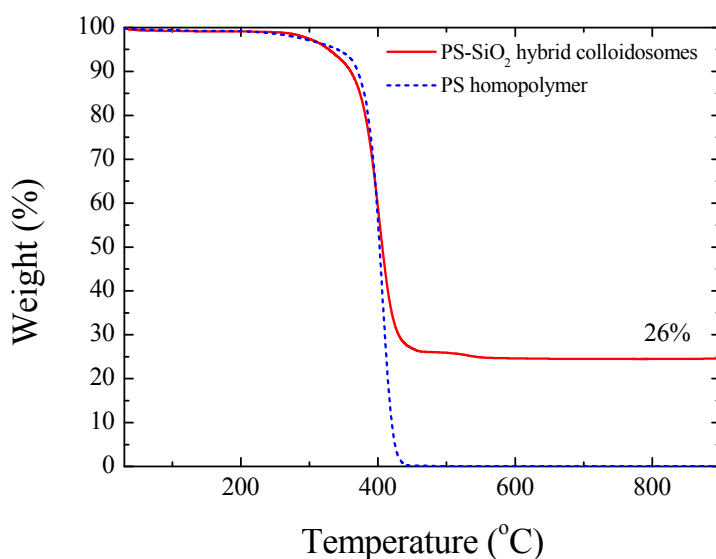


**Figure 3.20.** Thermogram of the PS-SiO<sub>2</sub> hybrid colloidosomes compared to a PS homopolymer.

*(ii) PS-SiO<sub>2</sub> hybrid colloidosomes after immobilization of FITC-Br on the exposed surface*

The amine functionality of the silica particles can be exploited in many ways in order to alter the surface properties of the particles. However, the solvent utilized for the synthesis of the colloidosomes prevents the acrylation of the amines by acid halides, such as  $\alpha$ -bromoisobutyryl bromide used in the synthesis of the monofunctional initiator. Therefore, isothiocyanate coupling with the amine group of APTES was achieved. FITC-Br was added in a dispersion of the PS-SiO<sub>2</sub> hybrid colloidosomes prepared above and the exposed amine groups on the surface of the silica particles were allowed to react with the isothiocyanate groups of FITC-Br. After their synthesis the colloidosomes were observed by SEM in order to verify the presence of the silica particles onto the surface of the PS microparticles during the reaction. Figure 3.21 shows that the colloidosomes retained their spherical shape and the silica particles remained on the PS surface, while the absence of unbound particles indicates that their affinity for the PS microparticles was not compromised during the reaction.

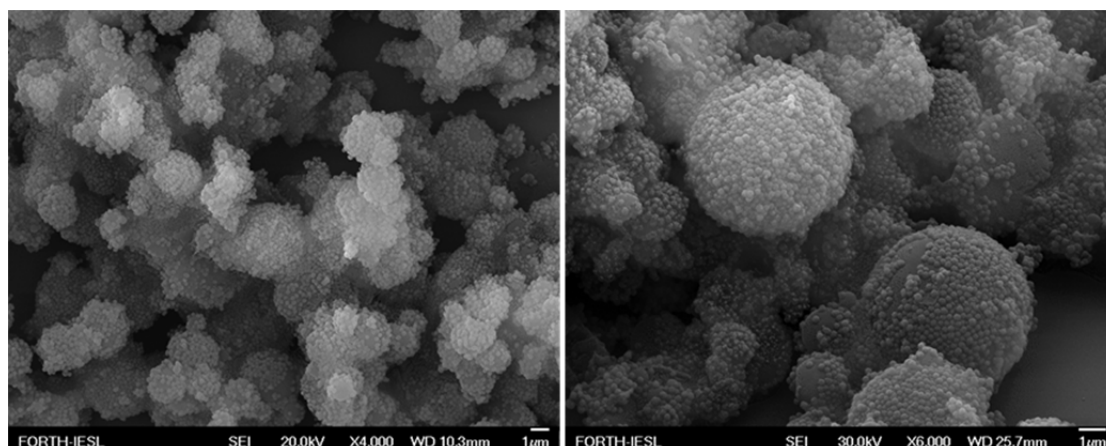


**Figure 3.21.** SEM images of the PS-SiO<sub>2</sub> hybrid colloidosomes synthesized in methanol following the reaction of the amine groups on the surface of the silica particles with FITC-Br.

The successful immobilization of the FITC-Br initiator onto the exposed surface of the silica particles was qualitatively verified by fluorescence microscopy. Figure 3.22 shows the images acquired for the colloidosomes dispersed in methanol. The intense green color was attributed to the fluorescence emission of FITC-Br which indicates the successful reaction of the exposed amine groups of the silica particles with the isothiocyanate moiety of the FITC-Br initiator.

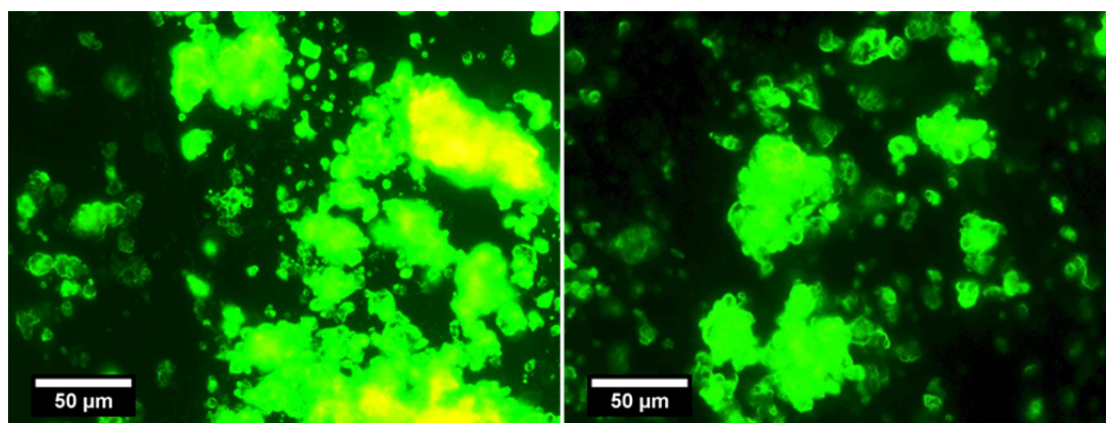


**Figure 3.22.** Fluorescence micrographs of the PS-SiO<sub>2</sub> hybrid colloidosomes after immobilization of FITC-Br on the exposed surface of the particles.

### 3.5 Janus colloidal initiator particles

Following the immobilization of FITC-Br onto the exposed surface of the silica particles on the PS-silica colloidosomes in methanol, the sample was dried and toluene was added in order to dissolve the PS microparticles. After dissolution of the PS microparticles, the silica particles were analyzed by TGA (Figure 3.23). The resulting curve was compared to that of the APTES -functionalized silica particles. An 8.6 % total weight loss was found for the Janus initiator particles (J-FITCBr) while a 13.5 % weight loss was observed for the APTES-functionalized particles. This is in contrast to the expected values, as the organic components of J-FITCBr are more compared to the APTES-functionalized particles. However, weight loss of the APTES-functionalized particles from room temperature up to 200 °C is attributed to physically adsorbed water molecules. Therefore, a total 8 % weight loss was attributed to the decomposition of APTES.

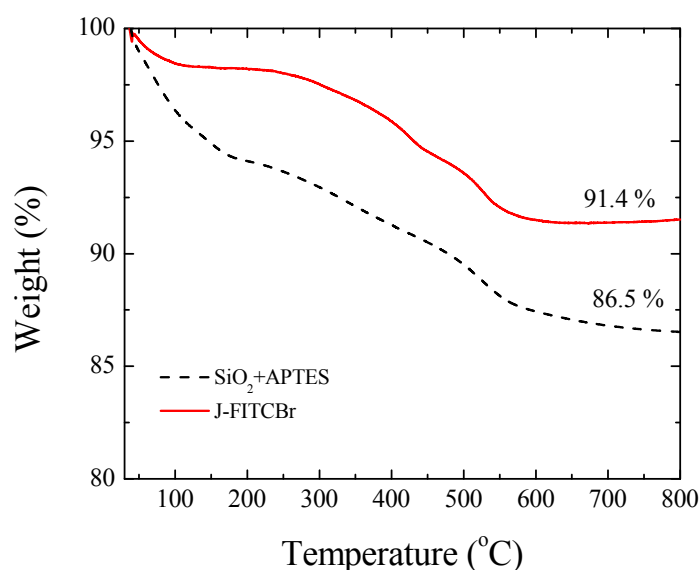


**Figure 3.23.** Thermogram of the Janus colloidal initiator particles and the amine-functionalized particles.

The decoration of the J-FITCBr particles with gold nanoparticles was achieved by the electrostatic interaction of the positively charged amine groups on the one hemisphere of the J-FITCBr particles at low pH values with the negatively charged gold nanoparticles. The successful decoration was verified by TEM (Figure 3.24). The

darker, due to their higher electron density, gold nanoparticles were only observed on one part of the surface of the lighter silica particles. This was attributed to the fact that only a part of the surface of the silica particles is functionalized with the amine groups and is thus positively charged and therefore capable to interact via electrostatic interactions with the gold nanoparticles.

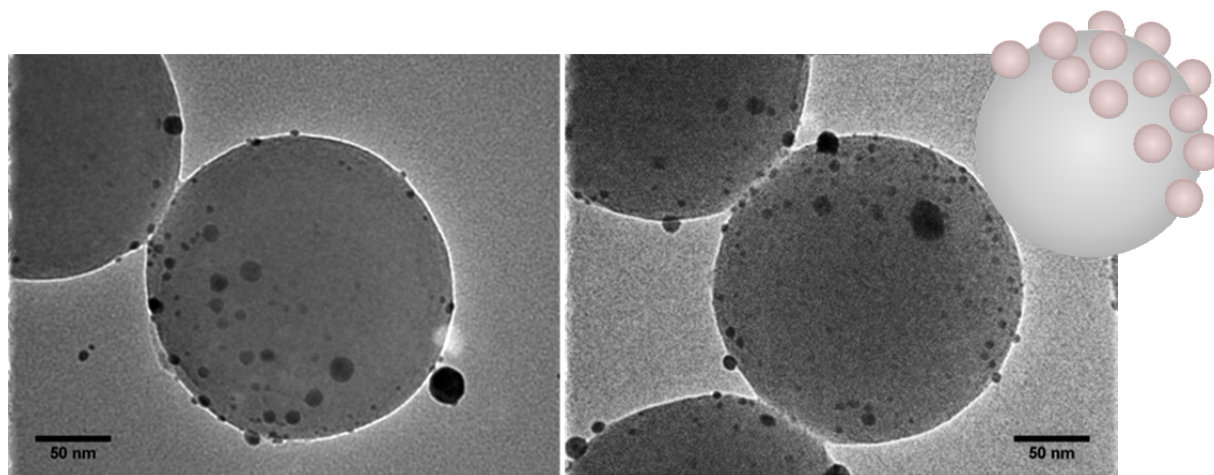


**Figure 3.24.** TEM images of the J-FITCBr particles decorated with gold nanoparticles.

Next, the J-FITCBr particles were reacted with hematoporphyrin chloride in order to synthesize dual-dyed green-red particles. The successful synthesis was verified by fluorescence microscopy (Figure 3.25) by overlaying the red and green fluorescence images. The appearance of green areas in the images is attributed to the immobilization of FITC-Br on one part of the surface of the particles (green), while the presence of red areas is attributed to the successful reaction of hematoporphyrine dichloride with the amine groups on the other part of the surface of the particles (red). Moreover, the magnified image (Figure 3.25, bottom) shows the localization of the two dyes on the surface of a larger particle, verifying the Janus character of the particles.

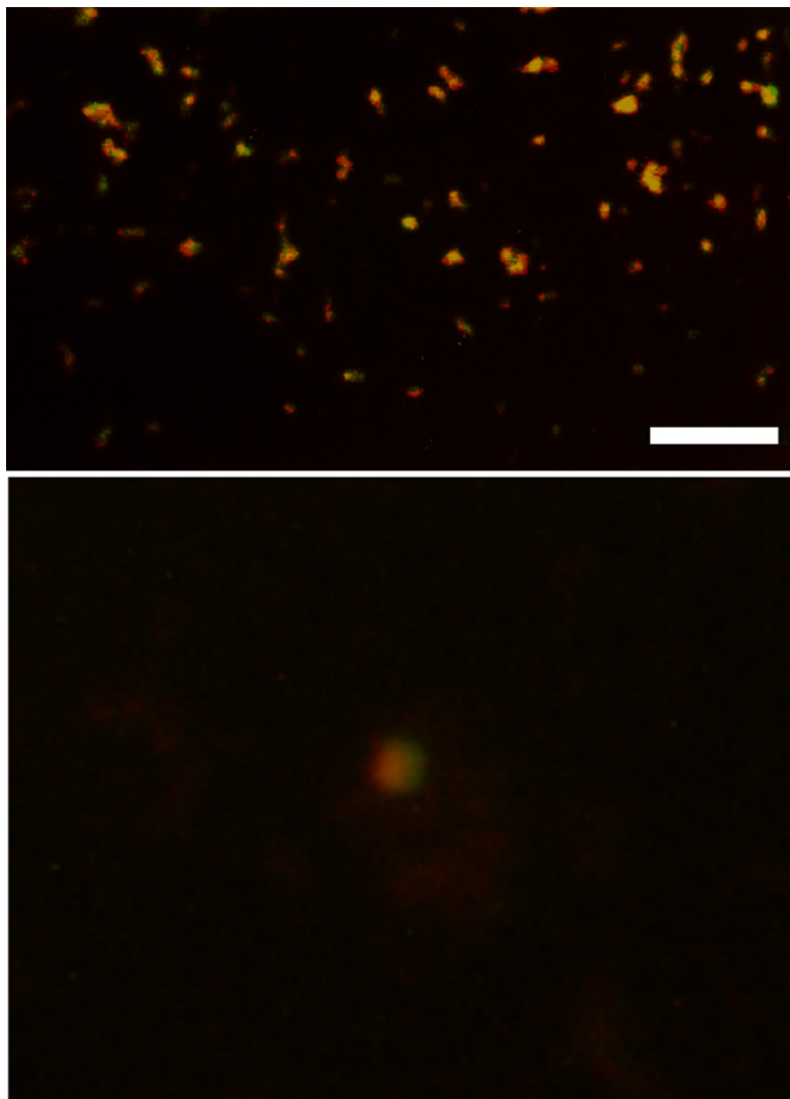


**Figure 3.25.** Red/Green fluorescence overlay image of the J-FITCBr particles (scale bar 10  $\mu\text{m}$ ) (top), magnified image (bottom).

### **3.6 Atom transfer radical polymerization in bulk**

#### **3.6.1 ATRP in bulk initiated by the monofunctional initiator**

##### *(i) ATRP of MMA in bulk*

The ATRP of MMA in bulk was investigated in order to determine the conditions that will allow controlled polymer growth. Figure 3.26 shows the chromatograms of the polymers retrieved after 1 hour and 2.25 hours of polymerization of MMA catalyzed by Cu(I)Cl at 70 °C. The narrow shape of the peaks revealed a low molecular weight distribution (PDI) of the polymer ( $M_w/M_n = 1.09$ ) while the molecular weights were found to be 77,000 g/mol after 1 hour of polymerization and 100,000 g/mol after 2.25 hours of polymerization. Therefore, control of the reaction is achieved, which renders these polymerization conditions attractive to be employed for the growth of PMMA brushes from the surface of the silica particles.

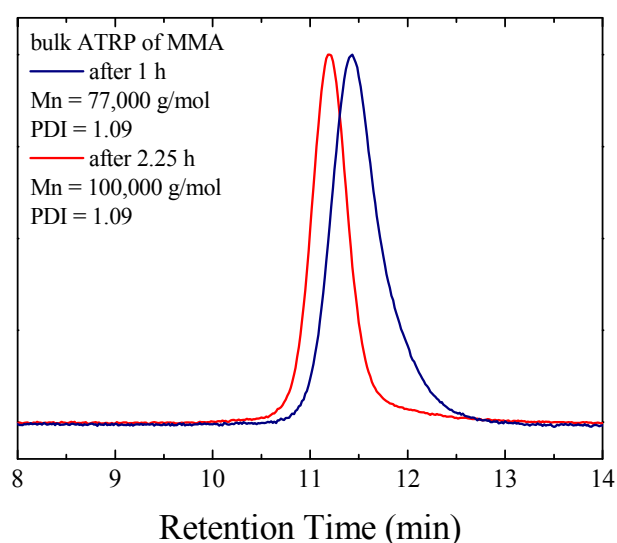


**Figure 3.26.** Chromatograms of PMMA homopolymers prepared by the bulk ATRP of MMA.

*(ii) ATRP of t-BuA in bulk*

Similar to the polymerization above for MMA, the controlled ATRP of t-BuA was also investigated using a mixture of Cu(I)Br and Cu(II)Br (19.7:1 ratio) as the metal salts and PMDETA as the ligand. The controlled nature of ATRP of tBuA in bulk was investigated by following the molecular weight and the molecular weight distribution of samples extracted from the polymerization mixture at predetermined time intervals. The resulting chromatograms are shown in Figure 3.27. Although at short reaction times the peaks appear to be broad and asymmetric, as the reaction proceeds, narrower peaks are obtained. Moreover, the peaks shift to lower retention times as the reaction proceeds, indicating the increase of the polymer molecular weight.

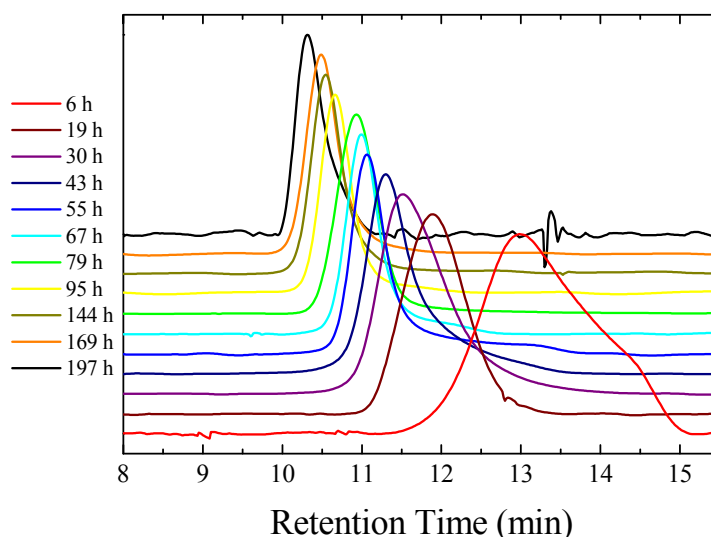


**Figure 3.27.** Chromatograms of the samples retrieved at predetermined time intervals from the ATRP of tBuA in bulk.

These observations were verified plotting the molecular weight and the molecular weight distribution of the polymer as a function of reaction time (Figure 3.28). The molecular weight increases in an almost linear fashion for 100 h of reaction time, while the increase of the molecular weight slows down from 100 h to 197 h of polymerization reaching a value of 193,200 g/mol at 197 h. The latter is attributed to the slower diffusion of the reactive chain ends in the reaction mixture at high monomer conversions which slows down the polymerization rate. Moreover, a

decrease of the molecular weight distribution of the polymer is observed as a function of polymerization time, reaching a minimum of 1.07 after 197 h of polymerization. These findings indicate the control of the polymerization process and the synthesis of controlled structure polymers, although the reaction kinetics are quite slow.

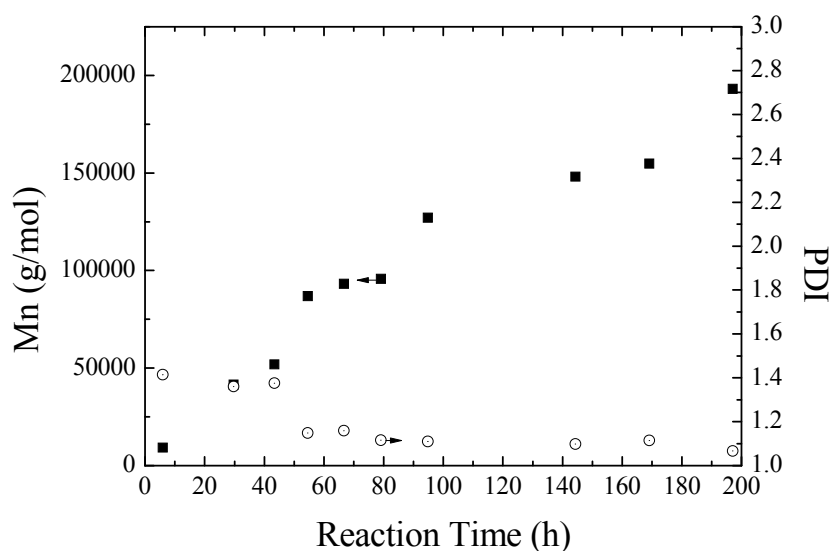


**Figure 3.28.** Dependence of the molecular weight ( $M_n$ ) and the molecular weight distribution (PDI) on the reaction time for the bulk ATRP of *t*BuA in bulk.

*(iii) ATRP of DMAEMA in bulk*

Two catalytic systems were investigated for the ATRP of DMAEMA in bulk. In both cases, DMAEMA was polymerized at 26 °C in the presence of HMTETA as the ligand and either Cu(I)Cl or Cu(I)Br as the metal salt. Figure 3.29 shows the chromatograms for the samples extracted from the reaction mixture of the ATRP of DMAEMA using Cu(I)Br as the metal salt. The shift of the peaks to lower retention times verified the increase of the molecular weight of the polymer with the reaction time. At short reaction times narrow peaks were obtained indicating a low molecular weight distribution of the polymer. However, as the reaction proceeds, tails appear at high retention times suggesting that termination reactions take place during the polymerization.

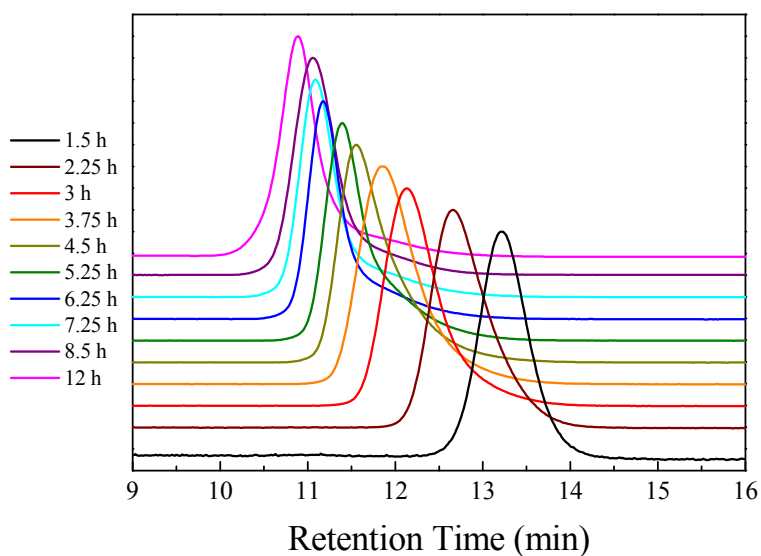


**Figure 3.29.** Chromatograms of the samples extracted from the ATRP of DMAEMA in bulk in the presence of Cu(I)Br as the metal salt.

These observations were quantitatively verified by the comparison of the molecular weights and the molecular weight distributions of the polymer as a function of monomer conversion (determined by  $^1\text{H}$  NMR) (Figure 3.30). A linear increase of the polymer molecular weight is evidenced reaching a maximum value of 101,300 g/mol after 12 h reaction time (93.7 %). The molecular weight distributions were found to be narrow at low conversions (1.07) and maintained a constant value (1.2) for higher conversions. Although such behavior is not typical for “living” polymerizations, the polymers retain a relatively low molecular weight distribution at high molecular weights and the reaction kinetics are quite fast.

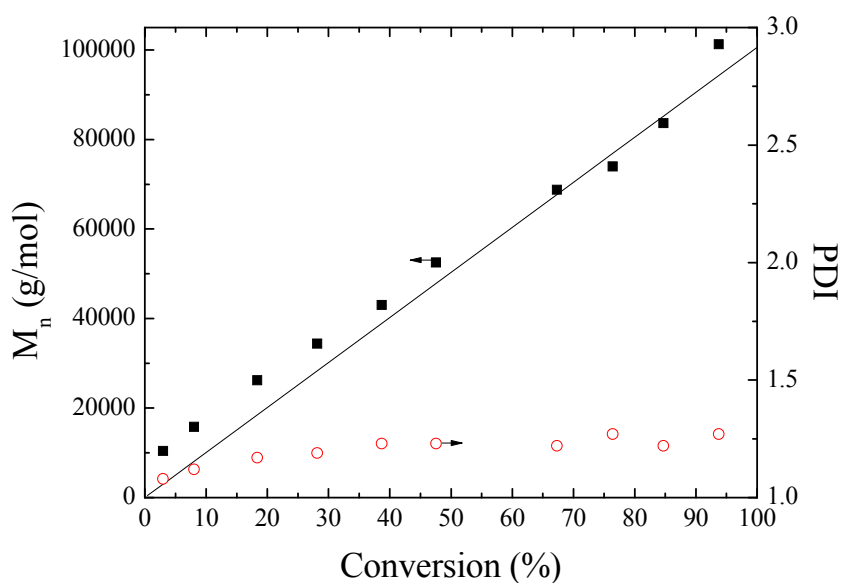


**Figure 3.30.** Dependence of the molecular weight and the molecular weight distribution from the monomer conversion for the polymerization of DMAEMA in the presence of Cu(I)Br as the metal salt.

Cu(I)Cl was also employed as the metal salt for the polymerization of DMAEMA in bulk and the results were compared to the ones obtained from the ATRP of DMAEMA in the presence of Cu(I)Br. Figure 3.31 shows the chromatograms obtained for the samples extracted at predetermined time intervals from the bulk ATRP of DMAEMA in the presence of Cu(I)Cl as the metal salt. The shift of the peaks to lower retention times as the reaction proceeds implies an increase of the molecular weight of the polymer. Although the peaks obtained for the shorter reaction times are broad suggesting a high molecular weight distribution, upon increase of the polymerization time narrower peaks are obtained suggesting the synthesis of a polymer with lower molecular weight distribution.

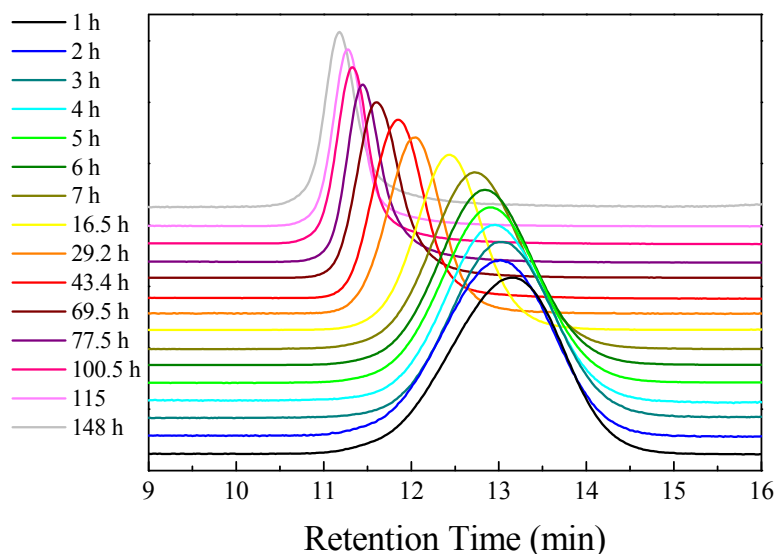


**Figure 3.31.** Chromatograms of the samples extracted from the bulk ATRP of DMAEMA in the presence of Cu(I)Cl as the metal salt.

These observations were verified by plotting the molecular weight and the molecular weight distribution of the polymer as a function of the monomer conversion (determined by  $^1\text{H}$  NMR) (Figure 3.32). Two distinctive regions were observed for the molecular weight, a fast increase up to 35 % conversion and a slower one up to 80 % conversion. This is attributed to the slower diffusion of the reactive chain ends in the reaction mixture. On the other hand the molecular weight distribution of the polymer is found to decrease as the reaction proceeds, reaching a minimum value of  $M_w/M_n = 1.12$  at a molecular weight of 70,000 g/mol, after 148 h of polymerization.

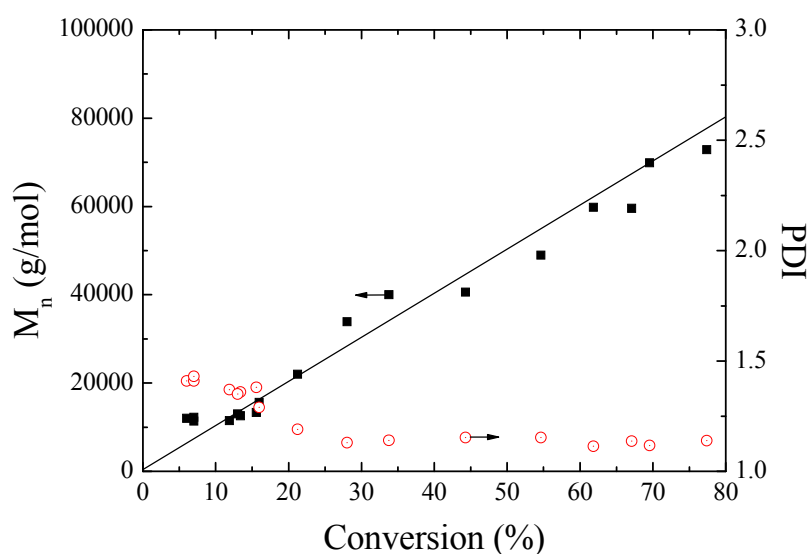


**Figure 3.32.** Dependence of the molecular weight and the molecular weight distribution from the monomer conversion of the ATRP of DMAEMA at the presence of Cu(I)Cl as the catalyst.

Comparing the results of the two polymerization systems, it is found that in both cases it is possible to achieve the synthesis of high molecular weight PDMAEMA in a controlled fashion. However, the use of Cu(I)Br as the metal salt provided narrow molecular weight distribution of the polymer at low conversions and wider at higher conversions. The termination reactions that take place will effectively compromise the presence of the bromine group at the growing chain end. This is not the case for the Cu(I)Cl catalyzed reaction where the molecular weight distribution of the polymer is narrow at high monomer conversions indicating the presence of the halide at the growing chain end which, however, comes at the price of long reaction times.

### 3.6.2 ATRP in bulk initiated by the bifunctional initiator

#### (i) ATRP of MMA in bulk

The effectiveness of Fluo-Br as a bifunctional ATRP initiator was examined for the polymerization of MMA in bulk employing the same reaction conditions as the ones used for the ATRP of MMA initiated by the monofunctional initiator. Figure 3.33 shows the chromatograms obtained for the samples extracted at predetermined time intervals from the reaction mixture. The resulting peaks are quite narrow suggesting a low molecular weight distribution of the polymer while the shift of the peaks to lower retention times is attributed to the increase of the polymer molecular weight as the polymerization proceeds.

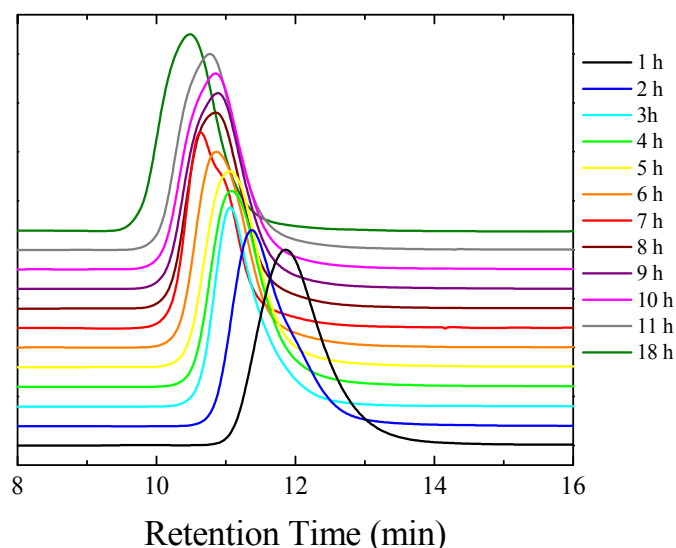


**Figure 3.33.** Chromatograms of the samples extracted from the bulk ATRP of MMA initiated by the bifunctional initiator Fluo-Br.

These observations were verified by plotting the molecular weight and the molecular weight distribution of the extracted polymers as a function of the polymerization time (Figure 3.34). A linear increase of the molecular weight up to 98,800 g/mol for 6 h reaction time is observed, while the molecular weight distributions remained almost constant at 1.3. However, for longer reaction times the increase in molecular weight is slow reaching a maximum value of 174,000 g/mol after 18 h reaction time. This deviation from the typical behavior of a “living”

polymerization was attributed to the fact that utilizing a bifunctional initiator, termination reactions on one initiating site may have a more pronounced effect. This was also evident in the chromatogram for the 7 h sample (Figure 3.33) for which a bimodal peak was observed.

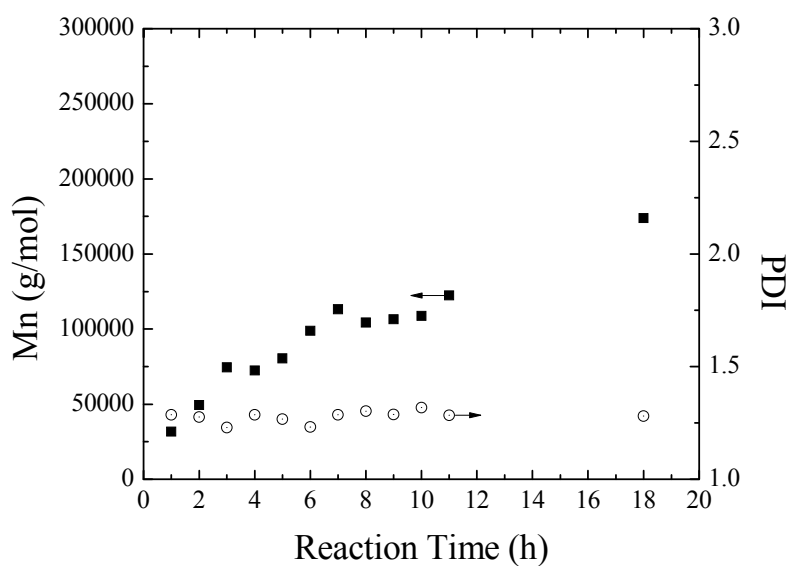


**Figure 3.34.** Dependence of the molecular weight and the molecular weight distribution on the reaction time for the ATRP of MMA initiated by the bifunctional Fluo-Br initiator.

### 3.7 Fully polymer-coated silica particles

#### 3.7.1 PMMA fully-coated particles

The ATRP of MMA in bulk was first initiated from the surface of the fully-coated with the monofunctional initiator silica particles (FCA). The successful growth of polymer chains from the surface of the particles was verified by TGA (Figure 3.35a). The sample exhibited a similar decomposition behavior to that of the PMMA homopolymer curve shown for comparison. The total weight loss of the hybrids was found to be 30 % and was attributed to the decomposition of the polymer component.

MMA was also utilized for the surface-initiated ATRP in bulk from the fully-coated with the bifunctional initiator silica particles (FCF). Two samples were prepared in order to produce particles with different polymer content, by allowing the polymerization to proceed for 12 and 18 h, respectively. The thermograms of the hybrid particles are shown in Figure 3.35b. A similar decomposition behavior is observed for both samples compared to the PMMA homopolymer, although an extra step is apparent at 220 °C for the hybrid particles attributed to the decomposition of the initiator. The total weight loss for the 12 h sample was found to be 46 %, while a higher weight loss (61 %) was found for the 18 h sample. This higher weight loss was attributed to the higher polymer weight fraction for the 18 h sample, suggesting further polymer growth as the polymerization proceeds.

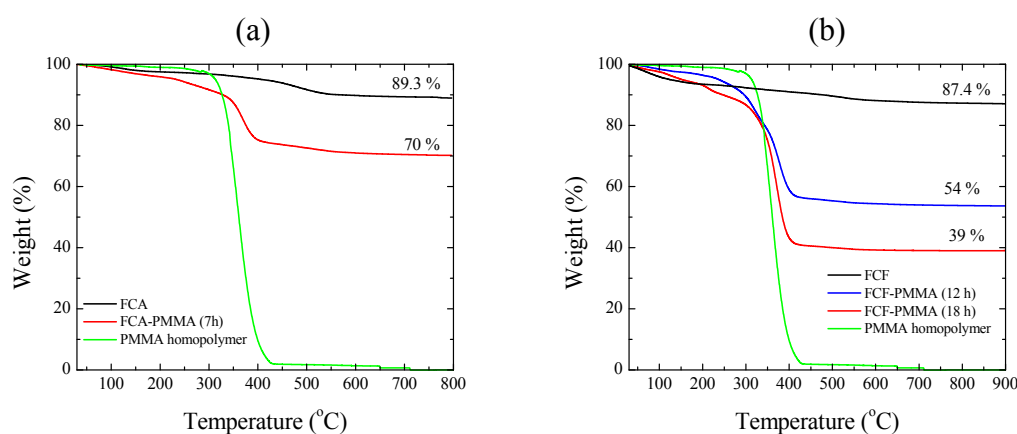


**Figure 3.35.** Thermogram of the FCA (a) and FCF (b) particles after the surface-initiated ATRP of PMMA in bulk.

In order to determine the molecular weight and the molecular weight distribution of the polymer chains grafted on the surface of the FCA-PMMA and FCF-PMMA particles, the free polymer produced in the reaction mixture from the unbound initiator added, was analyzed by GPC. For the FCA-PMMA particles (Figure 3.36a) a narrow peak was obtained suggesting a low molecular weight distribution of the polymer. Analysis of the results gave a molecular weight of 208,800 g/mol with polydispersity index 1.07, suggesting the presence of long polymer chains onto the surface of the particles with narrow size distribution.

The resulting chromatograms from the GPC analysis of the free polymers collected from the ATRP of MMA from the FCF particles are also shown in Figure 3.36b. Similarly to the reactions carried out in the absence of the particles (section 3.6.2 ATRP in bulk initiated by the bifunctional initiator), the resulting peaks are broad and a shoulder appears at low retention times. An increase of the molecular weight of the polymer with polymerization time is evidenced from the shift of the peak to lower retention times. For the 12 h sample, the molecular weight was found to be 135,000 g/mol with a polydispersity index of 1.21 while for the 18 h sample the molecular weight increased to 213,000 g/mol with a polydispersity index of 1.18. While these molecular weights are relatively high, it should be noted that they are produced from a bifunctional initiator. Thus, each arm should have half the molecular weight found by GPC. This is important when considering the grafted PMMA chains, as from each initiator molecule two polymer chains are grown. Therefore, the molecular weight of the PMMA chains extending from the surface of the particles is 67,700 g/mol and 106,600 g/mol, for the 12 h and the 18 h sample, respectively.

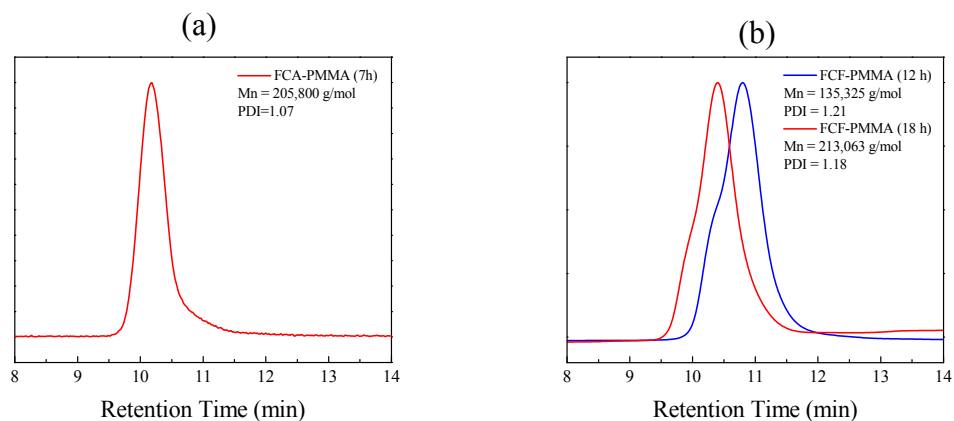


**Figure 3.36.** Chromatograms of the free polymers produced during the ATRP in bulk of MMA from the surface of the FCA (a) and FCF (b) particles.

The findings of the TGA and GPC measurements for the PMMA fully-coated particles are summarized in Table 3.1. A higher polymer weight fraction is found for the FCF-PMMA particles although the molecular weight of the grafted chains is significantly lower compared to that of the FCA-PMMA particles. This is quantitatively expressed from the calculation of the grafting densities of the polymer chains on the surface of the particles. For FCA-PMMA the grafting density was found to be 0.1 chains/nm<sup>2</sup>, whereas for the FCF-PMMA samples the grafting density increased from 0.64 to 0.73 chains/nm<sup>2</sup> from 12 h to 18 h polymerization time. This suggests that the amount of chains grafted per particle is more than 6 times higher for the FCF-PMMA particles compared to the FCA-PMMA particles (Table 3.1). Although a higher number of grafted chains per particle for the FCF particles was expected due to the use of a bifunctional initiator, the values obtained are surprising. This was attributed to the higher efficiency of the ester-based initiators compared to amide-based ones,<sup>4</sup> as well as to the accuracy limits of the TGA and GPC analysis.

**Table 3.1.** TGA and GPC results for the PMMA fully-coated particles and calculation of the grafting densities of the samples.

	FCA-PMMA	FCF-PMMA	FCF-PMMA
	7 h	12 h	18 h
Polymer weight fraction (TGA)	0.30	0.46	0.61
$M_n$ free polymer (g/mol)	205,800	135,300	213,100
$M_n$ grafted polymer (g/mol)	205,800	67,650	106,550
grafting density (chains/nm <sup>2</sup> )	0.10	0.64	0.73
chains per particle	20,500	125,000	144,000

The hydrodynamic size of the PMMA fully-coated particles was determined by DLS measurements in THF and DMF. As shown in Figure 3.37 a single exponential decay of the autocorrelation functions was observed for all the samples while the decay rate increases in a linear fashion as a function of the square wavevector, indicative of the uniform size of the particles and the absence of aggregates. The diffusion coefficient of the FCA-PMMA particles in THF was found to be  $1.617 \cdot 10^{-12}$  m<sup>2</sup>/s which corresponds to a hydrodynamic diameter of 566.9 nm. The diffusion coefficient of the FCF-PMMA particles in DMF was found to be  $1.055 \cdot 10^{-12}$  m<sup>2</sup>/s for the 12 h sample which corresponds to a hydrodynamic diameter of 422.0 nm, while for the 18 h sample the diffusion coefficient was found to be  $8.619 \cdot 10^{-13}$  m<sup>2</sup>/s which corresponds to a hydrodynamic diameter of 541.3 nm. These sizes are significantly higher than those found for the initiator-coated particles (236 nm) and were attributed to the PMMA chains extending from the surface of the particles.

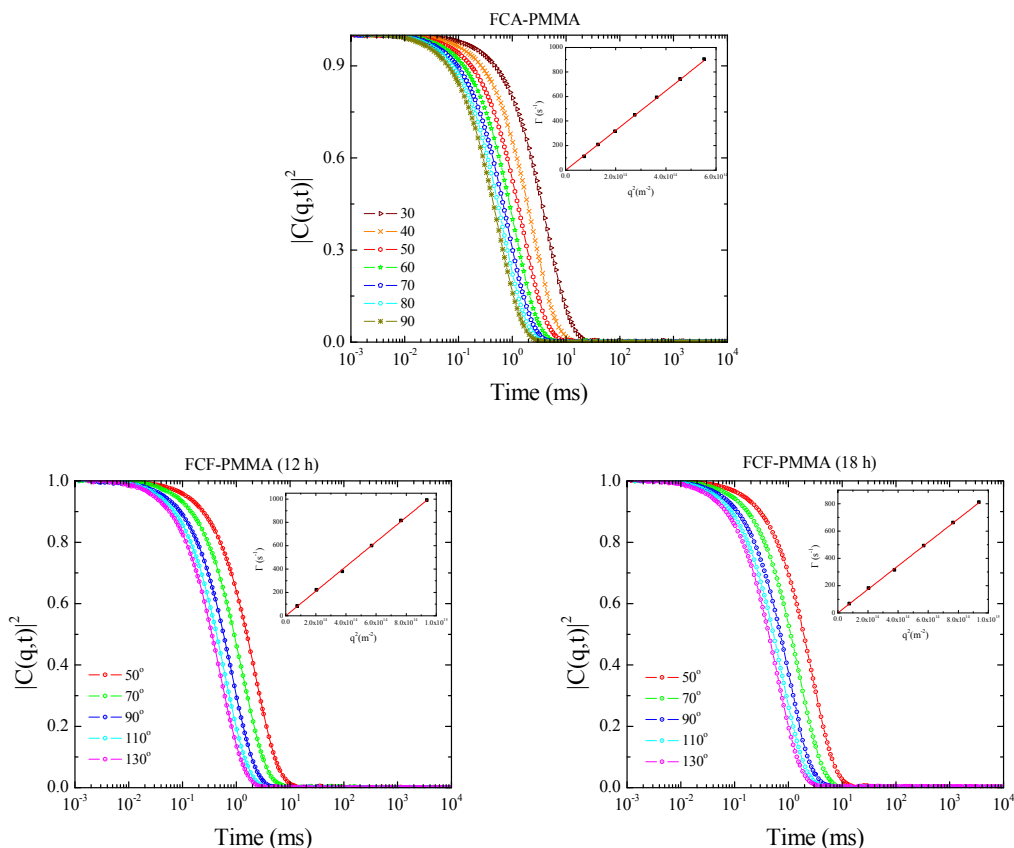


**Figure 3.37.** Intensity autocorrelation functions of the fully PMMA-coated particles. Insets: Autocorrelation decay rates calculated at different scattering angles.

The above results are summarized in Table 3.2 where the molecular weights of the PMMA grafts, the hydrodynamic diameters and the thickness of the polymer layer ( $h$ ) of the PMMA fully-coated particles are compared. The hydrodynamic diameter of the initiator-coated particles is also shown as a reference. It was found that the size of all the PMMA-coated particles has increased significantly. Also, the polymer thickness of the FCF-PMMA 18 h particles is 1.5 times higher than that of the FCF-PMMA 12 h particles, indicating a linear increase of the polymer thickness over reaction time. It should also be noted that although the FCA-PMMA particles bare polymer chains of double the molecular weight compared to the FCF-PMMA 18 h sample, the hydrodynamic diameter of the two samples is similar. This is attributed to the highly stretched conformation of the PMMA chains grafted on the FCF-PMMA 18 h sample, due to its particularly high grafting density.

**Table 3.2.** Molecular weights of the PMMA grafts and the hydrodynamic diameters of the PMMA fully-coated particles.

	SiO <sub>2</sub>	FCA-PMMA 7h	FCF-PMMA 12 h	FCF-PMMA 18 h
Mn (g/mol)		205,800	67,650	106,550
$D_h$ (nm)	236	566.9	422	541.3
h (nm)		165.45	93	152.65

The radius of gyration of the PMMA fully-coated particles was calculated from the minima of the scattering intensities as a function of the wavevector. The resulting curves are shown in Figure 3.38. The radius of gyration of the FCA-PMMA particles was found to be 169.1 nm while for the FCF-PMMA 12 h particles and the FCF-PMMA 18 h particles the radii of gyration were 187.9 nm and 206.6 nm respectively.

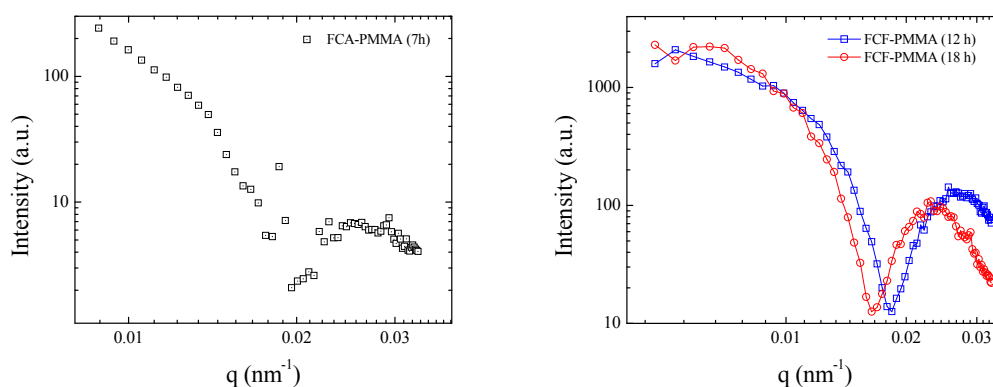


**Figure 3.38.** Scattering intensity of the PMMA fully-coated particles as a function of the wavevector ( $q$ ).

The above results are summarized in Table 3.3 together with the calculated shape factor ( $\rho = R_G/R_h$ ). While the FCA-PMMA particles were found to have the largest hydrodynamic radius, their radius of gyration is smaller than either of the FCF-PMMA particles. It should be noted that the shape factor of hard spheres is 0.774, which is close to the value found for the FCF-PMMA 18 h particles. This hard sphere behavior is attributed to the very high grafting density of the latter sample, as discussed above.

**Table 3.3.** Comparison of the radii of gyration ( $R_G$ ), the hydrodynamic radii ( $R_h$ ) and the shape factor ( $\rho$ ) of the PMMA fully-coated particles.

	FCA-PMMA	FCF-PMMA	FCF-PMMA
	7h	12 h	18 h
$R_G$ (nm)	169.1	187.9	206.6
$R_h$ (nm)	283.5	211.0	270.7
$\rho$	0.60	0.89	0.76

The FCF-PMMA particles were also observed by SEM as shown in Figure 3.39. In both cases, the particles have maintained their spherical shape while the roughness of the surface of the particles has increased due to the presence of the polymer shell. Neighboring particles are interconnected by a stretch neck ( $\circ$ ), attributed to the polymer component. Figure 3.39a and Figure 3.39c show two particles for the FCF-PMMA 12 h and 18 h samples, respectively, at the same magnification. An increase in the size of the particles is evident for the FCF-PMMA 18 h sample, attributed to the dense polymeric shell.

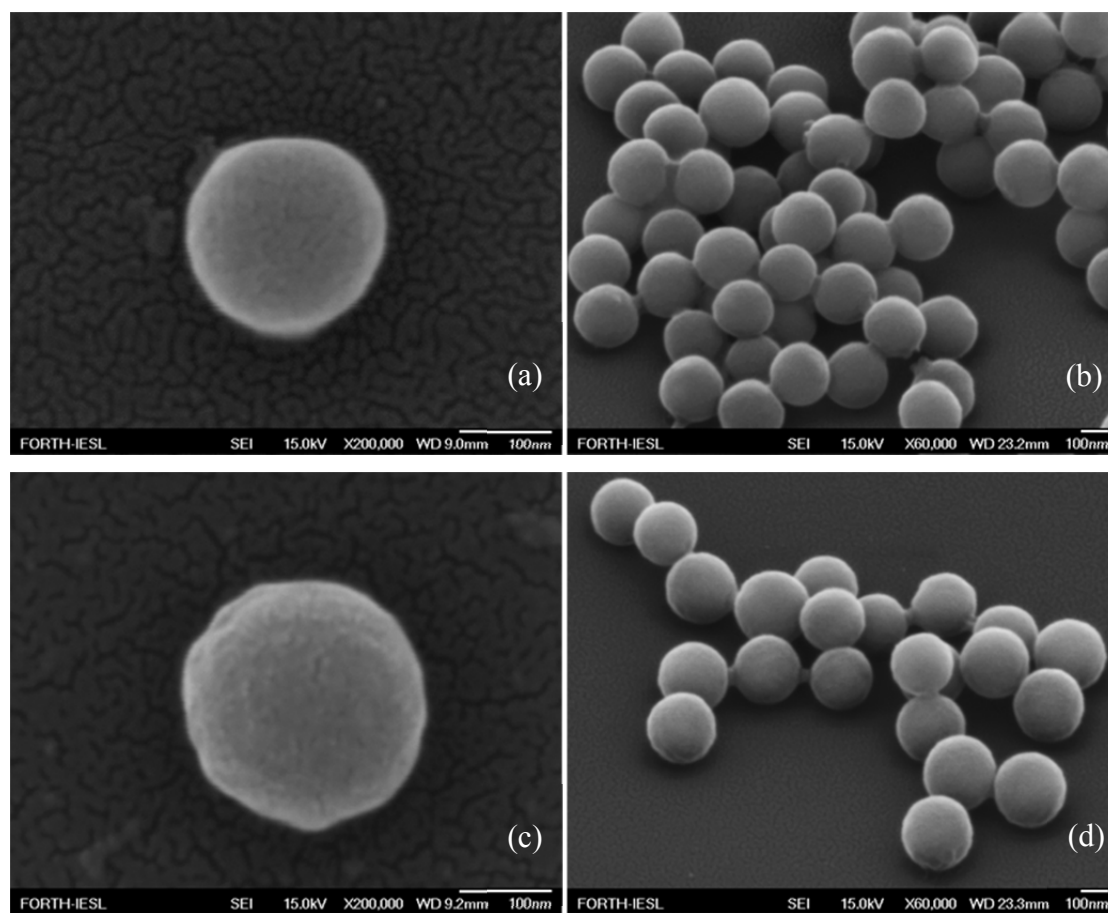


**Figure 3.39.** SEM images of the FCF-PMMA particles after 12 h (a,b) and 18 h (c,d) of polymerization.

### 3.7.2 PtBuA fully-coated particles

PtBuA is an attractive polymer since it can be hydrolyzed in order to form PAA. Although PtBuA is hydrophobic, PAA is anionic and would thus provide to the particles pH-responsive properties. *t*BuA was polymerized by ATRP in bulk from the surface of the silica particles bearing the monofunctional initiator (FCA). Two samples of different polymer contents were synthesized. This was achieved by extracting a sample from the reaction mixture after 24 h, while the polymerization was allowed to proceed for a total of 48 h. *t*BuA was also polymerized by ATRP in bulk for 240 h from the surface of the silica particles bearing the bifunctional initiator (FCF). The successful growth of the polymer chains from the surface of the particles was verified by TGA as shown in Figure 3.40. It was found that the FCA-PtBuA 24 h particles exhibited a 25.4 % total weight loss while the FCA-PtBuA 48 h particles exhibited a 17.5 % total weight loss (Figure 3.40a). However, the FCA-PtBuA 24 h particles exhibited a high weight loss at temperatures lower than 100 °C which was attributed to the evaporation of solvent. When this weight loss was subtracted from the total weight loss, the weight loss attributed to the thermal decomposition of the polymer was found to be 14 %. This verified the expected increase of the polymer content for the FCA-PtBuA 48 h sample due to the longer polymerization time. On the other hand, the FCF-PtBuA sample exhibited a 25 % total weight loss (Figure 3.40b) which was attributed to the thermal decomposition of the polymer.

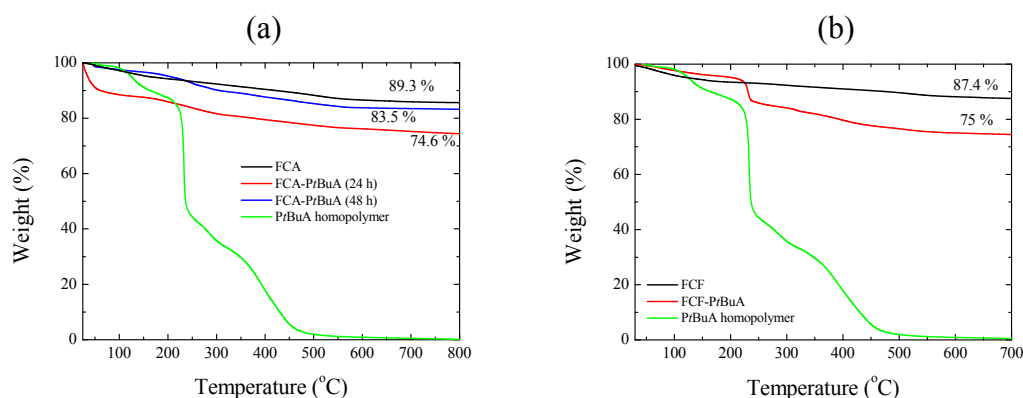


**Figure 3.40.** Thermograms of the FCA (a) and the FCF (b) PtBuA fully-coated particles.

The free *t*BuA chains polymerized from the unbound initiator present during the surface-initiated ATRP of *t*BuA were collected and analyzed by GPC as shown in Figure 3.41. The free polymer isolated from the ATRP of *t*BuA from the FCA particles shows narrow peaks for 24 h and 48 h of reaction, while shift of the peak, corresponding to the FCA-*Pt*BuA 48 h polymer, to lower retention times indicates the increase of the polymer molecular weight (Figure 3.41a). For the FCA-*Pt*BuA 24 h sample the molecular weight of the free polymer was found to be 35,800 g/mol with a polydispersity index of 1.24 while the molecular weight increased to 59,800 g/mol for the FCA-*Pt*BuA 48 h sample and the polydispersity index decreased to  $M_w/M_n = 1.16$ . These results verify the controlled growth of *Pt*BuA chains from the FCA particles surface. However, for the FCF-*Pt*BuA sample, a bimodal peak is observed with the two molecular weights being 160,500 g/mol and 20,000 g/mol suggesting the presence of two distinct polymer chain populations on the surface of the particles (Figure 3.41b). This contradicts the “living” character of ATRP, and is attributed to the long polymerization time required (240 h) which rendered the growing chains prone to side reactions.

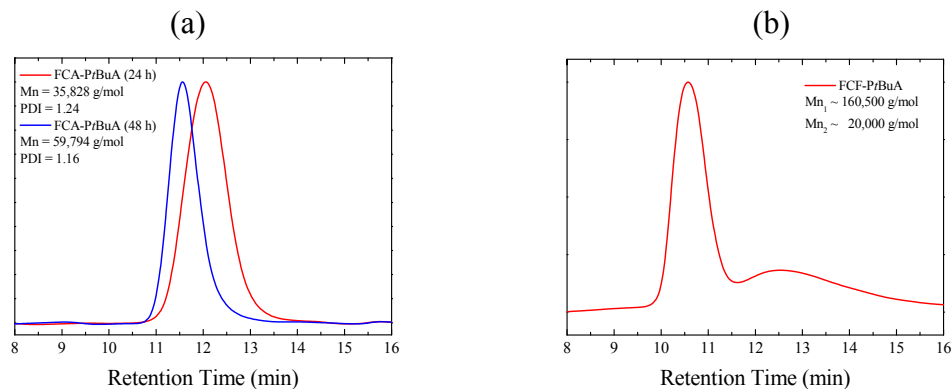


**Figure 3.41.** Chromatograms of the free polymer synthesized during the surface-initiated ATRP of *t*BuA.

The TGA and GPC characterization results for the FCA-*Pt*BuA and FCF-*Pt*BuA particles are summarized in Table 3.4. It is found that upon increasing the polymerization time, for the FCA-*Pt*BuA particles, the polymer weight fraction increased. The grafting density of the FCA-*Pt*BuA 24 h particles is found to be 0.23 chains/nm<sup>2</sup> which corresponds to 44,800 chains per particles while for the FCA-*Pt*BuA 48 h particles the grafting density is found to be 0.18 corresponding to 35,000

chains per particle. This difference is not considered to be significant given the accuracy of the results of the two characterization techniques. On the other hand, the bimodal polymer molecular weight distribution found for the FCF-*Pt*BuA prohibits the accurate calculation of the grafting density. In Table 3.4 we have calculated the two extreme values, assuming that the particles are fully coated with the longer and the shorter chains, respectively 0.89 chains/nm<sup>2</sup> was found in the case of all grafted chains having a molecular weight of 10,000 g/mol, and a value of 0.11 chains/nm<sup>2</sup> in the case of all grafted chains having a molecular weight of 80,250 g/mol. It is expected that the actual value is in between these two extreme values and therefore the number of grafted polymer chains per particle is expected to be between 173,900 and 21,700, respectively.

Taking into account the area of the peaks and the molecular weights found from the GPC analysis for the FCF-*Pt*BuA polymer and assuming a homogeneous distribution of the polymer chains onto the surface of the silica particles, the average grafting density was found to be 0.37 chains/nm<sup>2</sup> and therefore 72,600 polymer grafted chains per particle. These values are between the two extremes calculated above. It should also be noted that the number of grafted chains per particle is twice as high as the number found for the FCA-*Pt*BuA particles which is consistent with the bifunctional initiator used.

**Table 3.4.** TGA and GPC results for the surface-initiated polymerization of *t*BuA, grafting density and number of chains per particle.

	FCA- <i>Pt</i> BuA 24 h	FCA- <i>Pt</i> BuA 48 h	FCF- <i>Pt</i> BuA 240 h	
Polymer weight fraction	0.14	0.18	0.25	
M <sub>n</sub> free polymer (g/mol)	35,800	59,800	20,000	160,500
M <sub>n</sub> grafted polymer (g/mol)	35,800	59,800	10,000	80,250
grafting density (chains/nm <sup>2</sup> )	0.23	0.18	0.89	0.11
chains per particle	44,813	35,000	173,900	21,700

The hydrodynamic diameter of the *Pt*BuA fully-coated particles was measured by DLS. Figure 3.42 shows the autocorrelation functions and the decay rates of the autocorrelation functions for each sample. Single exponential decay autocorrelation functions were observed for all samples and together with the linear increase of the

decay rates with  $q^2$  suggest the presence of particles with uniform size and the absence of aggregates. The diffusion coefficient of the FCA-*Pt*BuA 24 h sample in THF was found to be  $2.918 \cdot 10^{-12}$  m<sup>2</sup>/s which corresponds to a hydrodynamic diameter of 314.1 nm while the diffusion coefficient of the FCA-*Pt*BuA 48 h sample in THF was found to be  $2.548 \cdot 10^{-12}$  m<sup>2</sup>/s corresponding to a hydrodynamic diameter of 359.7 nm. In a similar way, the diffusion coefficient of the FCF-*Pt*BuA particles in DMF was found to be  $1.440 \cdot 10^{-12}$  m<sup>2</sup>/s which corresponds to a hydrodynamic diameter of 323.9 nm. It is thus evidenced that all the *Pt*BuA fully-coated particles have sizes which are higher than the initial particles, while the size of the FCA-*Pt*BuA 48 h particles is as expected, larger than that of the FCA-*Pt*BuA 24 h sample, attributed to the further growth of the grafted polymer chains.

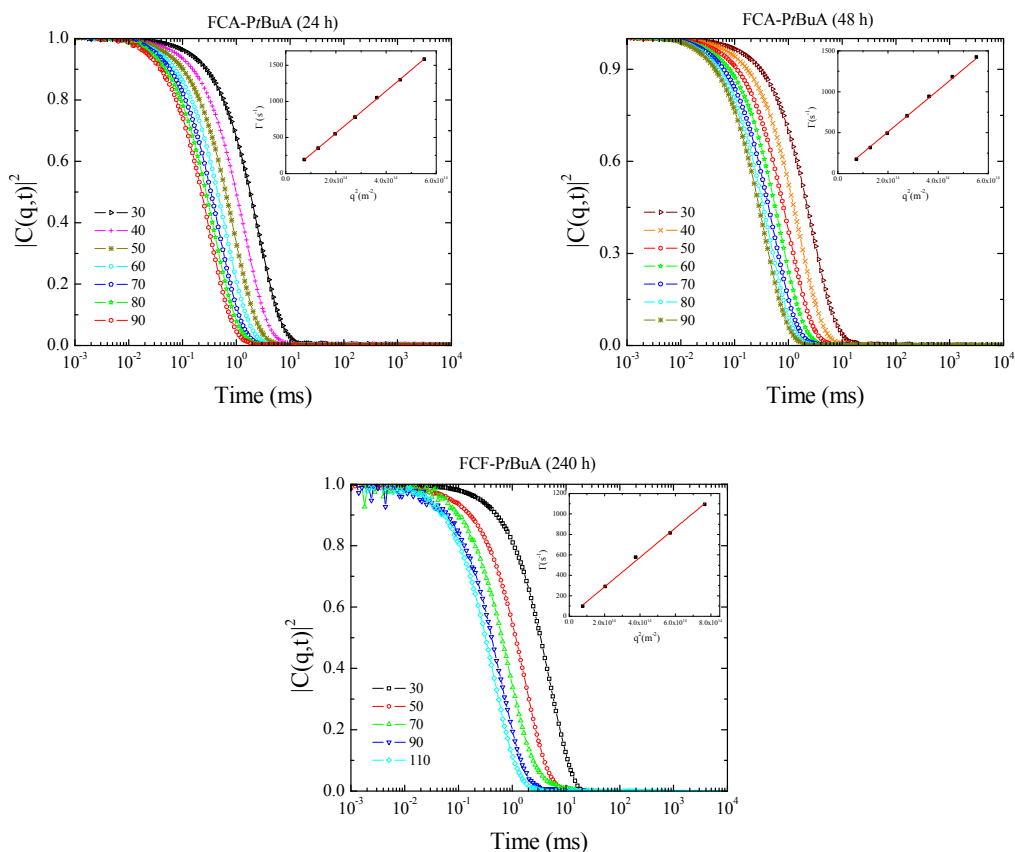


**Figure 3.42.** Intensity autocorrelation functions of the *Pt*BuA fully-coated particles. Insets: Decay rates of the autocorrelation functions as a function of the square wavenumber.

### 3.7.3 PDMAEMA fully-coated particles

PDMAEMA is a polymer which at high pH values is neutral. It also exhibits a lower critical solution temperature (LCST) in water at  $\sim 40$  °C. Tethering of PDMAEMA chains onto the surface of the silica particles will result in pH- and temperature-responsive hybrid particles.

The ATRP of DMAEMA was carried out from the surface of both FCA and FCF silica particles. The successful growth of the polymer chains was verified by TGA as shown in Figure 3.43. The decomposition behavior of both FCA-PDMAEMA and FCF-PDMAEMA particles is similar to the PDMAEMA homopolymer exhibiting a two-step decay. The FCA-PDMAEMA sample (Figure 3.43a) presented a 22.8 % weight loss attributed to the thermal decomposition of the polymer while the FCF-PDMAEMA sample (Figure 3.43b) presented a 43.5 % weight loss also attributed to the thermal decomposition of the polymer chains.

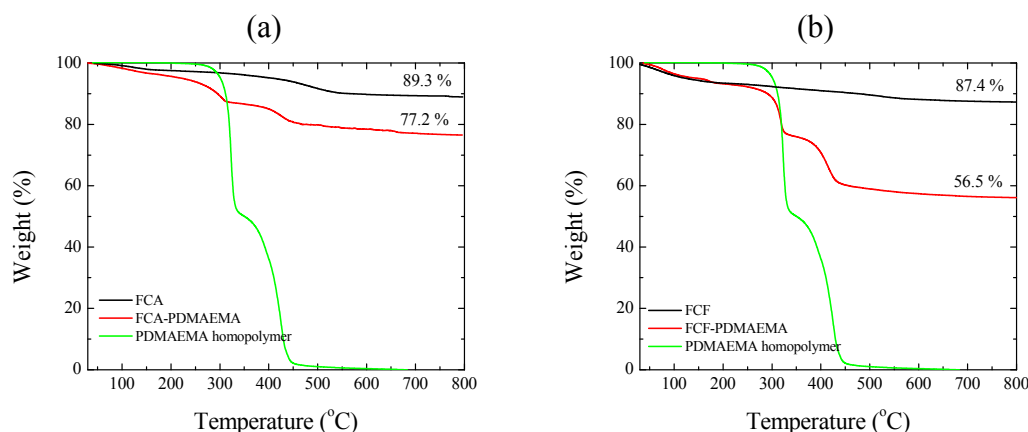


**Figure 3.43.** Thermograms of the FCA (a) and the FCF (b) PDMAEMA fully-coated particles.

The polymers retrieved from the polymerization by the free initiator present in the ATRP mixture were analyzed by GPC in order to determine the molecular characteristics of the grafted PDMAEMA chains. Narrow peaks were obtained indicating good control of the polymerization. The molecular weight of the free polymer for the FCA-PDMAEMA sample (Figure 3.44a) was found to be 114,200 g/mol with a polydispersity index of 1.11 while the molecular weight of the free polymer for the FCF-PDMAEMA sample (Figure 3.44b) was found to be 152,500 g/mol with a polydispersity index of 1.21. These results confirm the controlled nature

of the polymerization. It should be noted that the molecular weight of the grafted chains of the FCF-PDMAEMA particles is 76,300 g/mol, since the surface-bound initiator is bifunctional.

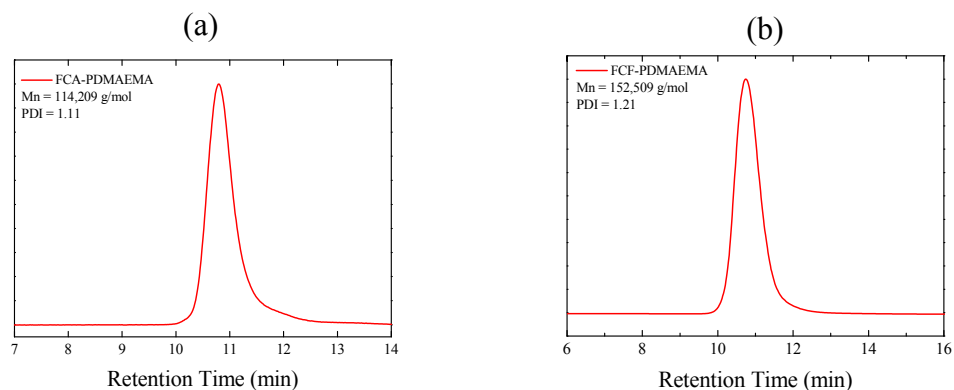


**Figure 3.44.** Chromatograms of the free PDMAEMA extracted from the polymerization mixture of the surface initiated ATRP of DMAEMA in bulk.

The TGA and GPC results are summarized in Table 3.5, where the calculation of the grafting density of the particles is also shown. It is apparent that although the FCF-PDMAEMA particles have shorter grafted polymer chains, the polymer weight fraction is much higher. This is quantitatively demonstrated by the calculated grafting density which is 0.13 chains/nm<sup>2</sup> for the FCA-PDMAEMA particles and 0.51 chains/nm<sup>2</sup> for the FCF-PDMAEMA particles. Thus, the number of chains grafted per particle is four times higher for the FCF-PDMAEMA particles indicating closely grafted chains. Although a higher number of grafted chains per particle for the FCF particles was expected due to the use of a bifunctional initiator, the values obtained are surprising. This was attributed to the higher efficiency of the ester-based initiator compared to the amide-based one, as well as to the accuracy limits of the TGA and GPC analysis.

**Table 3.5.** TGA and GPC results, grafting densities and chains per particle for the PDMAEMA-coated particles.

	FCA-PDMAEMA	FCF-PDMAEMA
	40 h	40 h
Polymer weight fraction	0.23	0.44
$M_n$ free polymer (g/mol)	114,200	152,500
$M_n$ grafted polymer (g/mol)	114,200	76,250
grafting density (chains/nm <sup>2</sup> )	0.13	0.51
chains per particle	25,500	99,400

The PDMAEMA-grafted particles were observed by SEM as shown in Figure 3.45. In both cases spherical particles are observed with a sticky material at the contact points of neighboring particles, attributed to the polymer content. The amount of the sticky segments is higher for the FCF-PDMAEMA sample which is in agreement with the higher polymer weight fraction found by TGA for this sample.

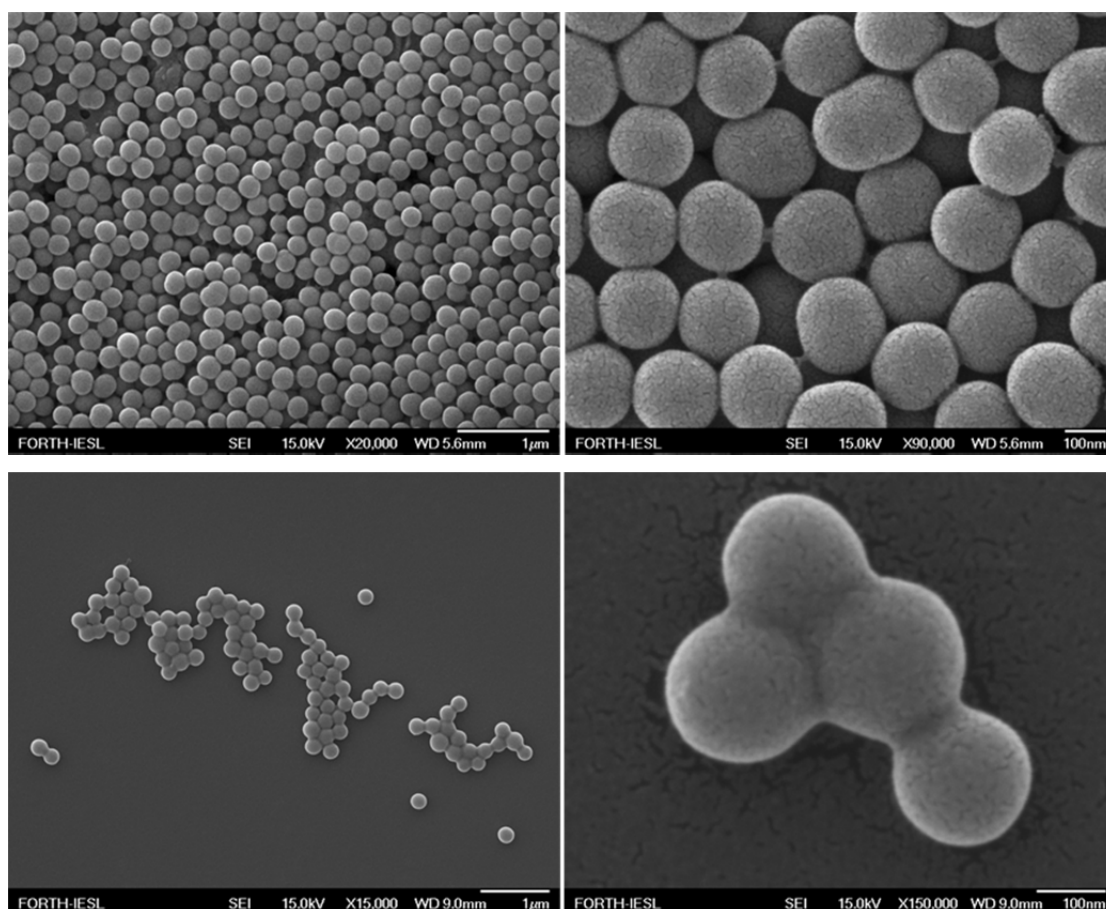


**Figure 3.45.** SEM images of the FCA-PDMAEMA (top) and the FCF-PDMAEMA (bottom) particles.

The hydrodynamic size of the FCF-PDMAEMA particles in DMF was measured by DLS. As seen in Figure 3.46, a single exponential decay of the intensity autocorrelation functions was observed, while the decay rates were found to increase linearly as a function of the square wavevector. This is indicative of the uniform size of the particles, as well as the lack of aggregates. The diffusion coefficient was found to be  $1.136 \cdot 10^{-12} \text{ m}^2/\text{s}$  which corresponds to a hydrodynamic diameter of 390 nm.

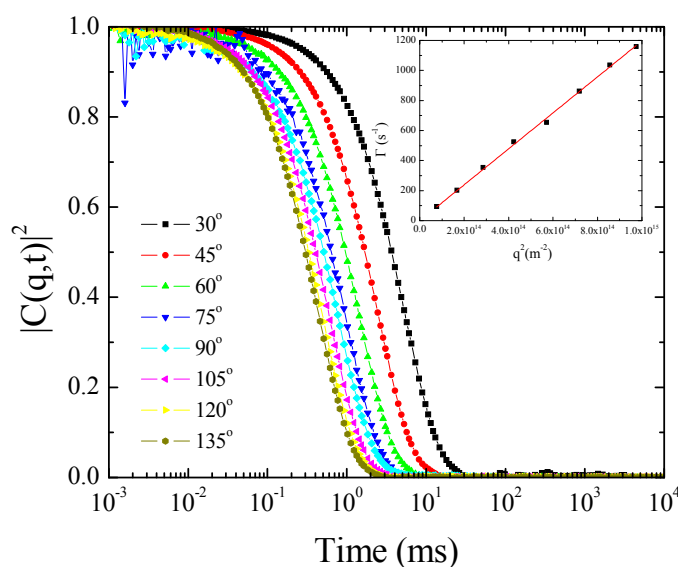


**Figure 3.46.** Intensity autocorrelation functions of the FCF-PDMAEMA particles in DMF. Inset: Decay rates as a function of the square wavevector.

The scattering intensity of the FCF-PDMAEMA particles was measured as a function of the wavevector as shown in Figure 3.47. The radius of gyration was extracted from the minimum observed at  $0.0226 \text{ nm}^{-1}$  and was found to be 152.5 nm. The shape factor ( $\rho$ ) of the FCF-PDMAEMA particles was found to be 0.782 which is close to the theoretical value of hard spheres (0.774). This was attributed to the fact that although the polymer chains that extend from the surface of the particles are soft, their high grafting density results in their stretching and thus, the particles behave more like hard spheres.

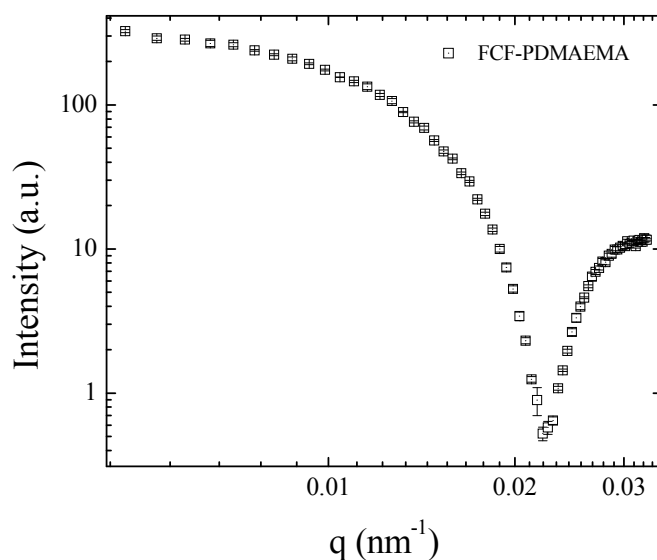


**Figure 3.47.** Scattering intensity of the FCF-PDMAEMA particles in DMF as a function of the wavevector.

*(i) pH responsive behavior*

PDMAEMA is a pH-responsive polymer which becomes protonated at low pH values. The pH-dependent behavior of the PDMAEMA-coated particles was investigated by the potentiometric titration of the FCF-PDMAEMA particles upon the addition of NaOH (0.1 M). The resulting curve shown in Figure 3.48 exhibits a plateau is observed at a pH value of 6.7. At low pH values the particles are well dispersed while addition of base results in the macroscopic precipitation of the particles at pH values higher than 9.45. This was attributed to the complete deprotonation of the tertiary amine groups of the DMAEMA moieties which renders the polymer shell hydrophobic.

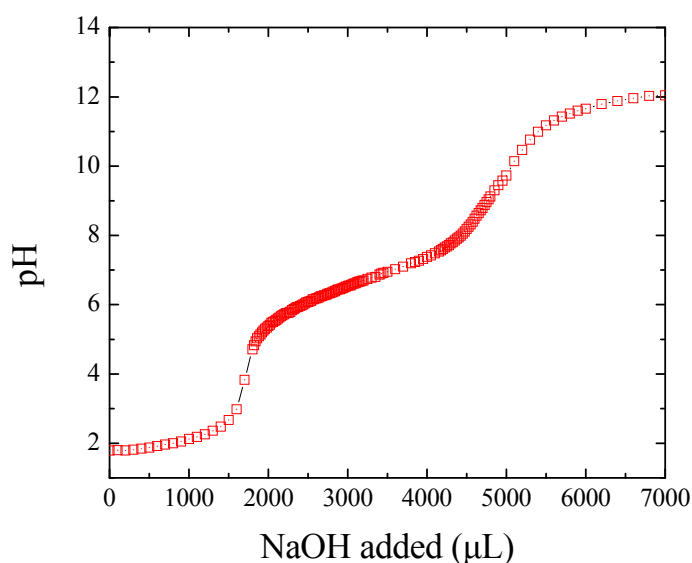


**Figure 3.48.** Potentiometric titration of the FCF-PDMAEMA particles upon addition of NaOH solution.

The degree of ionization ( $\alpha$ ) of the tertiary amine groups was calculated from the plateau region of the titration curve of the FCF-PDMAEMA particles according to the equation:

$$\alpha = \frac{1}{10^{pH-pK_a} + 1}$$

Figure 3.49 shows the resulting curve from the relation of the solution pH as a function of the degree of ionization of the DMAEMA moieties of the FCF-PDMAEMA particles. For  $\alpha = 0.5$ , thus half the amine groups are protonated, the pH value of 6.7 is equivalent to the  $pK_a$  of the particles.

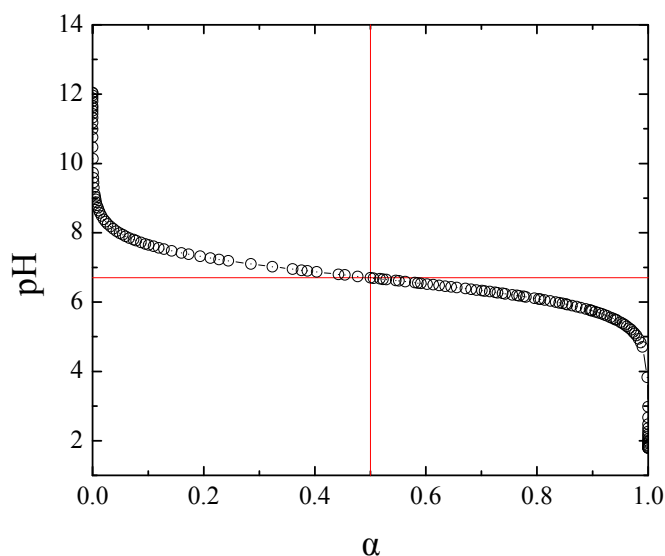


**Figure 3.49.** Solution pH as a function of the degree of ionization for the FCF-PDMAEMA particles in water.

The size of the FCF-PDMAEMA particles as a function of the degree of ionization ( $\alpha$ ) of the tertiary amine groups was studied by DLS measurements. The results shown in Figure 3.50 indicate that for degrees of ionization between 0.02 and 1 the intensity autocorrelation functions exhibit a single exponential decay which is accompanied by linear increase of the decay rates with  $q^2$ . This suggests particles with uniform size and the absence of aggregates. However, at a degree of ionization equal to zero a second relaxation process is observed, attributed to the formation of larger aggregates. For  $\alpha = 1$ , therefore fully protonated amines, the diffusion coefficient of the particles was found to be  $7.280 \cdot 10^{-13} \text{ m}^2/\text{s}$  which is equivalent to a hydrodynamic diameter of 588.4 nm. This value is much larger than the size found for the dispersion of the particles in DMF (390 nm) which was attributed to the stretching of the polymer chains due to the electrostatic repulsion of the neighboring DMAEMA units. Deprotonation of the amine groups to a degree of ionization 0.13 resulted in a faster process with a diffusion coefficient equal to  $8.625 \cdot 10^{-13} \text{ m}^2/\text{s}$  which corresponds to a hydrodynamic diameter of 496.6 nm. Further decrease of the degree of ionization to 0.02 resulted in the increase of the diffusion coefficient to  $9.699 \cdot 10^{-13} \text{ m}^2/\text{s}$  which is equivalent of a hydrodynamic diameter of 441.6 nm. Upon complete deprotonation of the tertiary amine groups ( $\alpha = 0$ ) the diffusion coefficient of the particles increased to  $1.550 \cdot 10^{-12} \text{ m}^2/\text{s}$  which corresponds to a hydrodynamic diameter of 276.4 nm, while a

second diffusive process was observed with a diffusion coefficient equal to  $2.179 \cdot 10^{-13} \text{ m}^2/\text{s}$  corresponding to a hydrodynamic diameter of 1965.4 nm and was attributed to large aggregates.

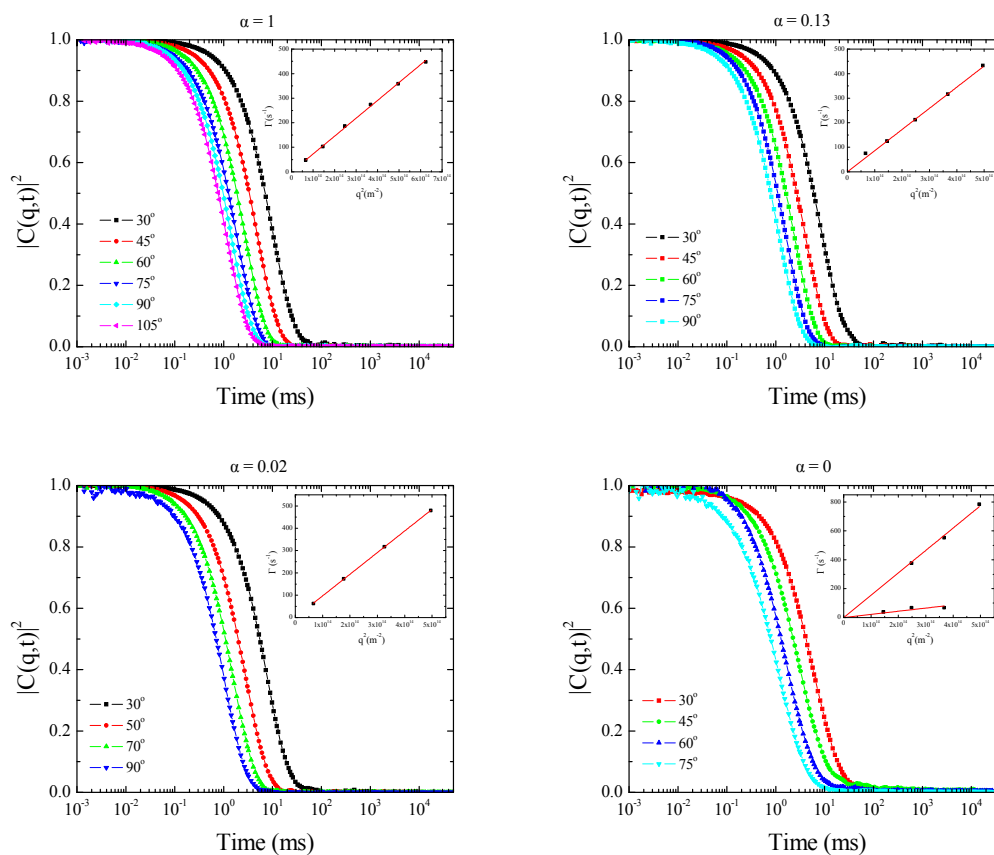


**Figure 3.50.** Intensity autocorrelation functions of the FCF-PDMAEMA particles in water at different degrees of ionization. Insets: decay rates as a function of the square wavevector.

The above results are depicted in Figure 3.51 where the hydrodynamic diameter of the FCF-PDMAEMA particles is shown as a function of the degree of ionization of the amine groups. Compared to the initiator-coated FCF particles in DMF, the fully protonated FCF-PDMAEMA particles in water have a much larger hydrodynamic diameter. Gradual decrease of the degree of ionization results in the decrease of the hydrodynamic diameter of the particles until, upon complete deprotonation, the size of the FCF-PDMAEMA particles becomes comparable to that of the FCF particles in DMF. This is attributed to the collapse of the polymer chains onto the surface of the

particles. At the same time large aggregates appear which are consistent with the macroscopic precipitation observed in the titration curve at high pH values.

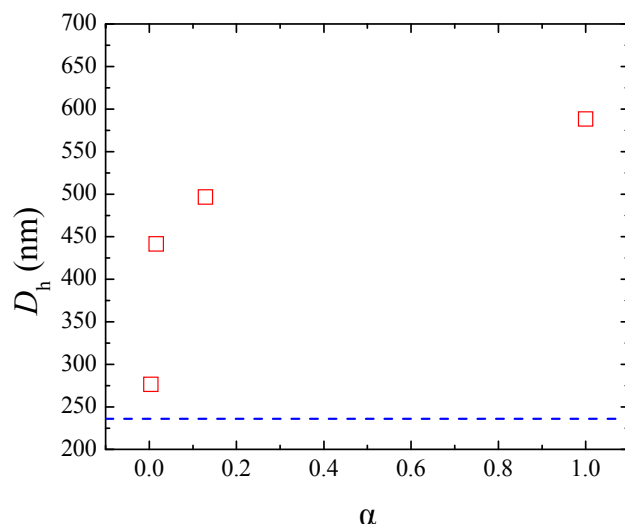


**Figure 3.51.** Dependence of the hydrodynamic diameter of the FCF-PDMAEMA particles on the degree of ionization of the tertiary amines of the polymer. The blue line shows the hydrodynamic diameter of the initiator-coated FCF particles for comparison.

*(ii) Temperature-responsive properties*

Since PDMAEMA is a temperature-responsive polymer, the temperature-dependent behavior of the FCF-PDMAEMA particles in water was studied by turbidimetry. The curves presented in Figure 3.52 show the sharp decrease of the optical transmittance of the FCF-PDMAEMA dispersions at two different pH values. The temperature where the quenching of the transmittance is first observed is assigned as the lower critical solution temperature (LCST) of the hybrids. It was found that the LCST of the FCF-PDMAEMA particles at a degree of ionization equal to 0.02 was at 37.5 °C while upon protonation of the polymer chains ( $\alpha=0.15$ ) the LCST of the particles increases to 59 °C. This was attributed to the increase of the charged monomer units that increase the hydrophilicity of the polymer layer and thus the LCST of the polymer and prevents the collapsing of the chains onto the surface of the

particles. The increase of the transmittance observed at temperatures above the LCST of the particles was attributed to the macroscopic precipitation of the particles.

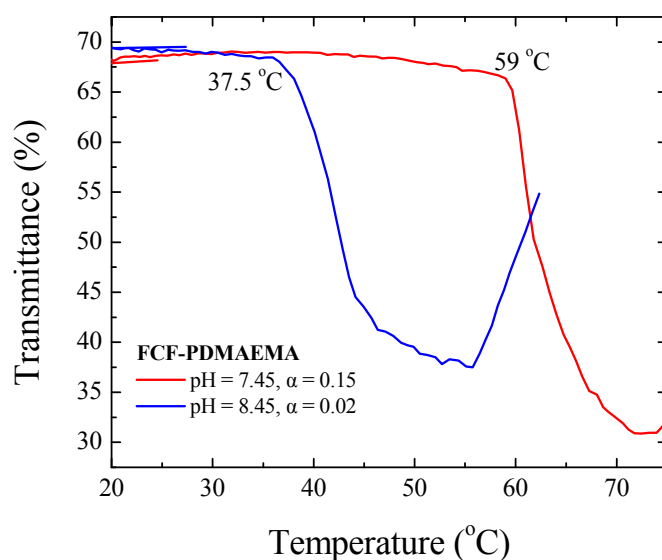


**Figure 3.52.** Transmittance of the FCF-PDMAEMA particles as a function of temperature in aqueous media, at a wavelength of 600 nm.

The effect of the solution temperature on the size of the FCF-PDMAEMA particles was studied by DLS. Figure 3.53 shows the intensity autocorrelation functions of a dispersion of the particles at different temperatures, for a constant degree of ionization of the DMAEMA units equal to 0.02. In all cases a single exponential decay was observed accompanied by a linear increase of the decay rates indicating the uniform size of the particles and the absence of aggregates. At 20 °C the diffusion coefficient was found to be  $9.699 \cdot 10^{-13} \text{ m}^2/\text{s}$  which is equivalent of a hydrodynamic diameter of 441.6 nm. Similarly, at 30 °C the diffusion coefficient of the particles was found to be  $1.227 \cdot 10^{-12} \text{ m}^2/\text{s}$  which corresponds to a hydrodynamic diameter of 453.6 nm. Upon increasing the temperature to 35 °C a higher diffusion coefficient equal to  $1.499 \cdot 10^{-12} \text{ m}^2/\text{s}$  was observed which corresponds to a hydrodynamic diameter of 418 nm. At 37 °C the diffusion coefficient increased further to  $1.578 \cdot 10^{-12} \text{ m}^2/\text{s}$  which corresponds to a hydrodynamic diameter of 415.8 nm. Finally, at a solution temperature of 40 °C the diffusion coefficient was  $6.968 \cdot 10^{-13} \text{ m}^2/\text{s}$  that corresponds to a much larger hydrodynamic diameter of 1007.8 nm.

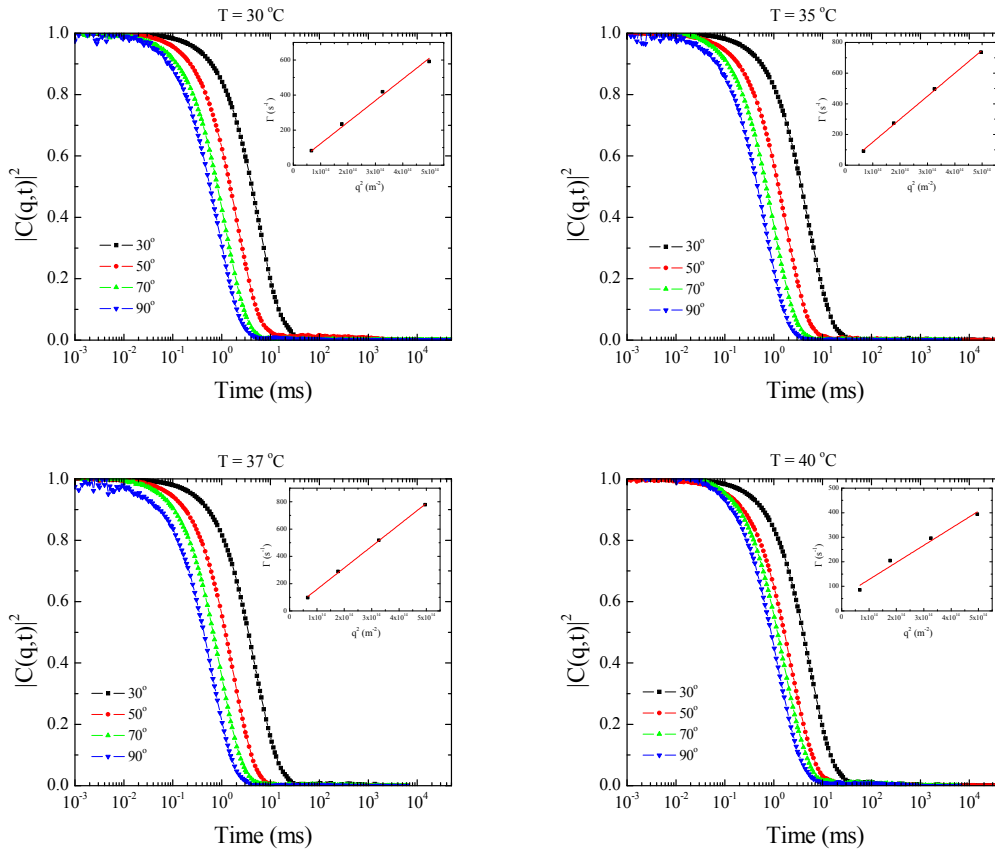


**Figure 3.53.** Intensity autocorrelation functions of the FCF-PDMAEMA particles at different solution temperatures. Inset: Decay rates as a function of the square wavevector.

The above results are summarized in Figure 3.54 where the hydrodynamic diameter of the particles is depicted as a function of the temperature of the solution. The gradual decrease of the hydrodynamic diameter of the particles above 30 °C was observed, attributed to the gradual collapse of the polymer shell as the LCST is approached. Moreover, above 37 °C a sharp increase of the size of the measured particles was found, which was attributed to the aggregation of the particles due to the temperature-induced hydrophobic interactions. The transition temperature of 37 °C is in good agreement with the LCST value measured above by turbidimetry (37.5 °C) for degree of ionization equal to 0.02.

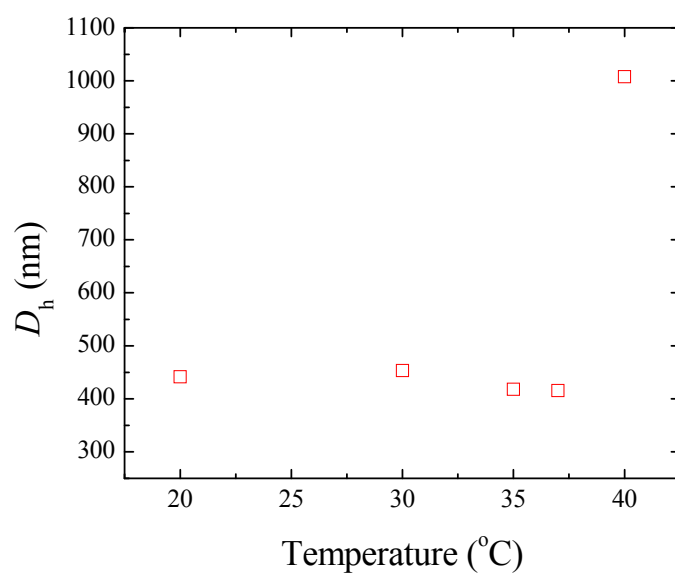


**Figure 3.54.** Dependence of the hydrodynamic diameter of the FCF-PDMAEMA particles on the solution temperature.

### 3.8 Janus particles with a polymer-coated hemisphere

#### 3.8.1 PMMA Janus particles (JF-PMMA)

The successful grafting of PMMA chains from the FITC-Br initiator-functionalized surface of the Janus particles was verified by TGA. Figure 3.55 shows the % weight loss for the JF-PMMA particles as a function of temperature. The sample exhibits a similar decomposition behavior to the PMMA homopolymer (also shown for comparison). A total 43.5 % weight loss was observed which was attributed to the decomposition of the organic content of the hybrids.

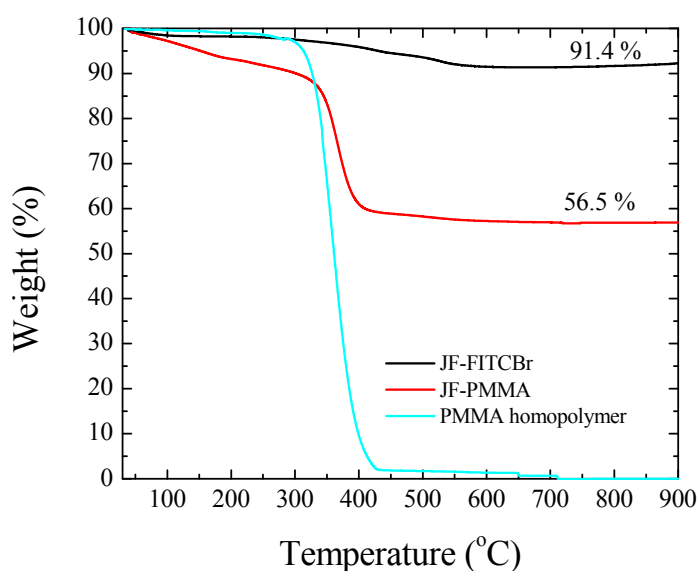


**Figure 3.55.** Thermogram of the JF-PMMA particles.

The unbound polymer obtained during the polymerization reaction from the added free Fluo-Br bifunctional initiator was analyzed by GPC. Figure 3.56 shows the chromatogram in which a narrow peak is observed, indicative of a controlled polymerization. The molecular weight of the polymer was found to be 292,800 g/mol with a polydispersity index of 1.33. Assuming that the polymerization is carried out in the same way both for the unbound initiator and the surface-bound initiator, the molecular weight of the grafted chains is considered to be half the molecular weight of the free polymer. This because both the free and the bound initiator are bifunctional, therefore the GPC measurement shows the total molecular weight of the

chain. Thereby, the molecular weight of the grafted chains is found to be 146,400 g/mol.

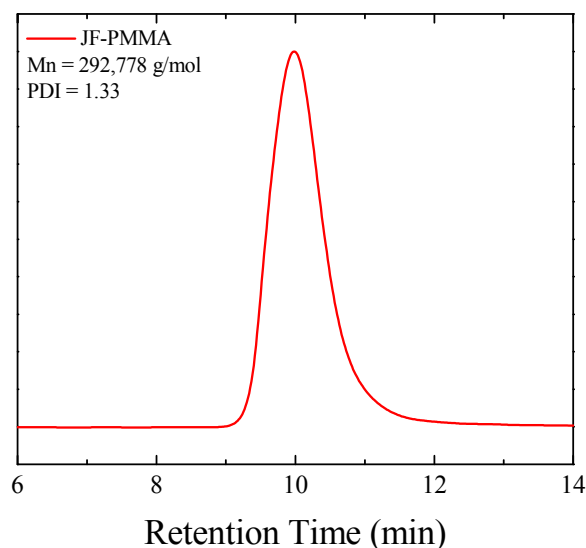


**Figure 3.56.** Chromatogram of the free polymer obtained for the surface initiated ATRP of MMA from the Janus particles.

The results from the TGA and GPC measurements for the JF-PMMA particles are summarized in Table 3.6. It is found that the effective grafting density is 0.26 chains/nm<sup>2</sup> which corresponds to 50,700 grafted chains per particle. The grafting density is not an absolute number, as the chains are not distributed in a uniform manner on the whole surface of the particles but are rather a patch on one side of the particle surface.

Comparing the results of the JF-PMMA particles to those of the FCF-PMMA 18 h particles, it was found that although the molecular weight of the grafted polymer is 1.5 time higher for the former particles, that is 146,400 g/mol and 106,550 g/mol for the JF-PMMA and the FCF-PMMA 18 h respectively, a higher weight loss (61 %) was found for the latter which resulted in a higher grafting density (0.73 chains/nm<sup>2</sup>). The lower grafting density of the JF-PMMA particles (0.26) was attributed to the partial functionalization of the surface of the silica particles with the ATRP initiator and therefore the growth of the PMMA chains from a patch of the particles surface.

**Table 3.6.** TGA and GPC results, grafting density and number of chains per particle for the JF-PMMA particles.

	JF-PMMA 18 h
Polymer weight fraction	0.44
$M_n$ free polymer (g/mol)	292,800
$M_n$ grafted polymer (g/mol)	146,400
grafting density (chains/nm <sup>2</sup> )	0.26
chains per particle	50,700

SEM was utilized to identify the topology of the JF-PMMA particles. Figure 3.57a shows spherical particles interconnected with a sticky polymeric neck which was attributed to the polymer chains. In the tilted view (Figure 3.57b), acorn-like particles are observed. The internal spherical entities are attributed to the silica particles while the outer hemispherical coating is attributed to the grafted polymer layer. This is supported by the fact that the coating is stretched at the contact points with neighboring particles, while the core retains its shape.

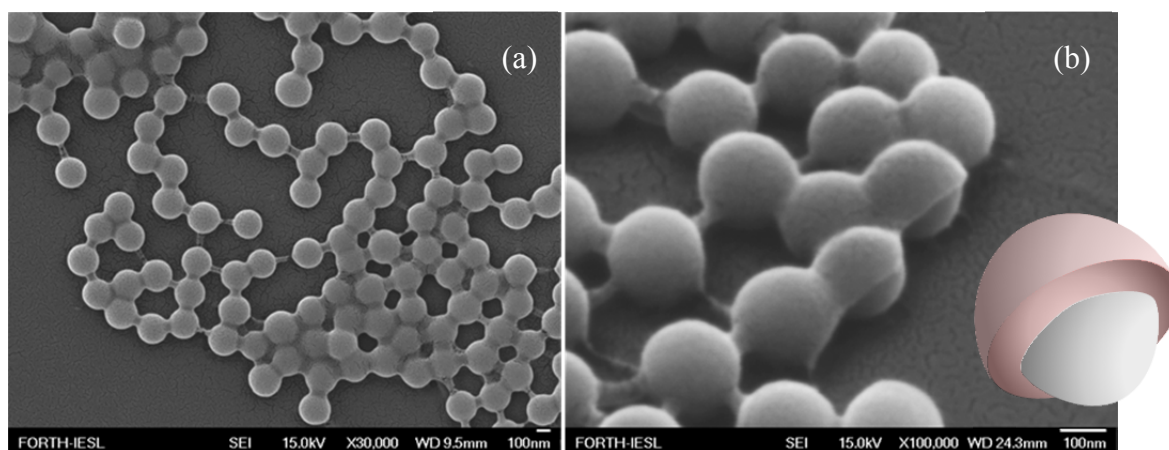


**Figure 3.57.** SEM images of the JF-PMMA particles from a top view (a) and a 45° tilted view (b).

The effective hydrodynamic diameter of the JF-PMMA particles was calculated by DLS in DMF. The resulting intensity autocorrelation functions shown in Figure 3.58 show a single exponential decay while the decay rates increase in a linear fashion as a function of the square wavevector. This is indicative of particles with uniform size as well as the absence of aggregates. The diffusion coefficient was found to be

$1.180 \cdot 10^{-12} \text{ m}^2/\text{s}$  which is equivalent to an effective hydrodynamic diameter of 395.5 nm. It is noted that the calculated size is only an effective value assuming a hard sphere model.

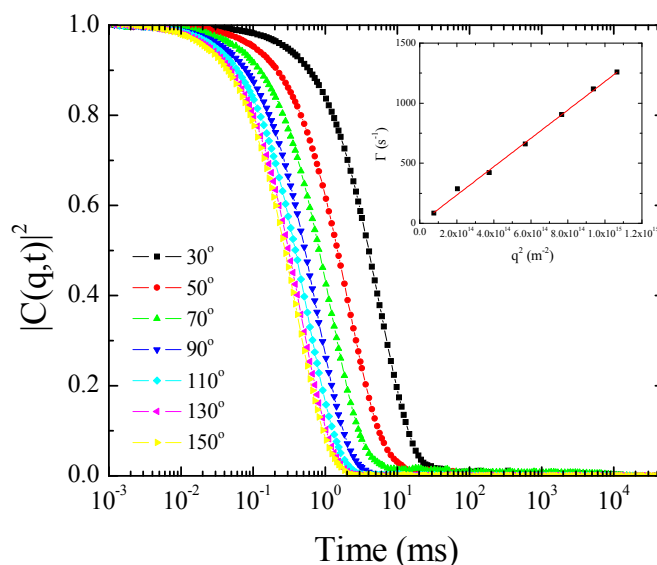


**Figure 3.58.** Intensity correlation functions for the JF-PMMA particles. Inset: Decay rates as a function of the square wavevector.

The radius of gyration was calculated from the minimum of the scattered intensity as a function of the wavevector shown in Figure 3.59. The minimum was found to be at  $0.0163 \text{ nm}^{-1}$  which is equivalent to a radius of gyration of 211.2 nm. Calculation of the shape factor of the JF-PMMA particles was found to be 1.07, which deviates from the hard sphere shape factor (0.774), however it cannot be attributed to the acorn-like shape of the particles since to our knowledge no such model exists.

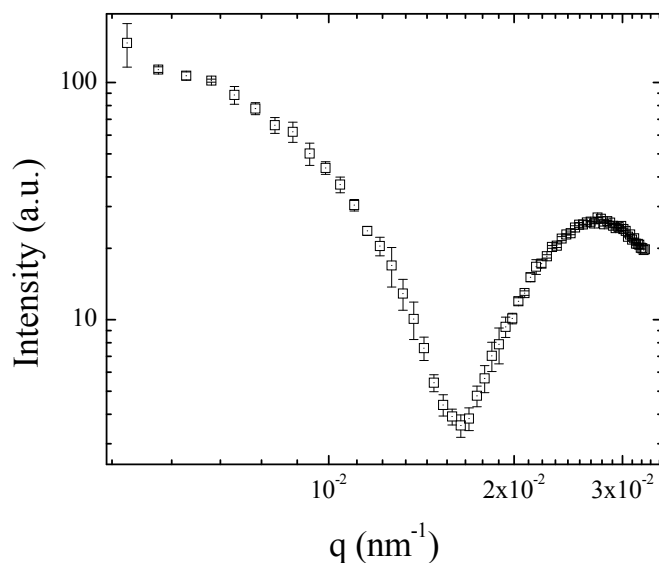


**Figure 3.59.** Scattered intensity for a dispersion of the JF-PMMA particles in DMF as a function of the wavevector.

The findings from DLS and SLS for the JF-PMMA particles are summarized in Table 3.7 and compared to the respective results from the FCF-PMMA particles. Taking into account the similar radii of gyration of the FCF-PMMA 18 h particles and the JF-PMMA particles it is observed that the hydrodynamic sizes of the two samples differ significantly. This is attributed to the different shapes of the two particles.

**Table 3.7.** Comparison of the  $R_G$ ,  $R_h$  and  $\rho$  values for the FCF-PMMA and JF-PMMA particles.

	FCF-PMMA 18 h	JF-PMMA 18 h
$R_G$ (nm)	206.6	211.2
$R_h$ (nm)	270.7	197.8
$\rho$	0.76	1.07

Due to the amphiphilic character of the JF-PMMA particles (one hemisphere is coated with hydrophobic PMMA chains whereas the other hemisphere with a monolayer of ionizable primary amino groups), their ability to stabilize toluene/water Pickering emulsions was evaluated. Toluene and acidic water were mixed at the presence of the particles. PMMA, a hydrophobic polymer, is expected to orient the PMMA-coated surface of the particles towards the organic toluene phase, while the

APTES-coated surface of the particles at low pH values becomes protonated and therefore is expected to orient towards the water phase. The test was repeated and compared for the fully APTES-coated particles and the two emulsions were well mixed and allowed to rest. Figure 3.60 shows the images taken for the two emulsions after 24 hours. The mixture containing the APTES-functionalized particles (Figure 3.60a) was phase-separated, and the particles were dispersed in the aqueous phase, indicated by the turbidity of the lower phase. On the other hand, the JF-PMMA particles have successfully stabilized the emulsion (Figure 3.60b), at the interface of the water and toluene phase. It is noted that neither the particle concentration, nor the toluene to water ratio was optimized in this experiment and thus the excess aqueous and organic phase were phase separated from the emulsion phase. This result verifies the Janus character of the JF-PMMA particles prepared in this study.



**Figure 3.60.** Image of the two phase system, toluene and water, in the presence of the APTES-modified particles (a) and the JF-PMMA particles (b).

Comparison of the FCF-PMMA 18 h particles and the JF-PMMA particles verifies the successful transformation of the silica particles to PMMA-silica Janus particles. The lower polymer weight fraction (thus the lower grafting density of the

polymer chains) and the smaller hydrodynamic size of the JF-PMMA particles, accompanied by the SEM images showing the acorn-like topology of the particles and the successful stabilization of a toluene/water emulsion, verify their Janus character.

### 3.8.2 PtBuA Janus particles (JF-PtBuA)

*t*BuA was polymerized from the FITC-Br –coated surface of the silica particles in order to obtain amphiphilic Janus particles with a hydrophobic polymer-coated hemisphere and a hydrophilic hemisphere decorated with ionizable primary amine groups. PtBuA can be hydrolyzed to produce the anionic PAA grafted chains which will render the particles zwitterionic and thus, give them interesting pH-responsive properties.

The successful grafting of PtBuA from the surface of the Janus initiator-coated particles was verified by TGA. Figure 3.61 shows the TGA curve for the JF-PtBuA particles in comparison to a PtBuA homopolymer. A similar decomposition behavior is observed while the total 17 % weight loss obtained was attributed to the pyrolysis of the organic content of the hybrids.

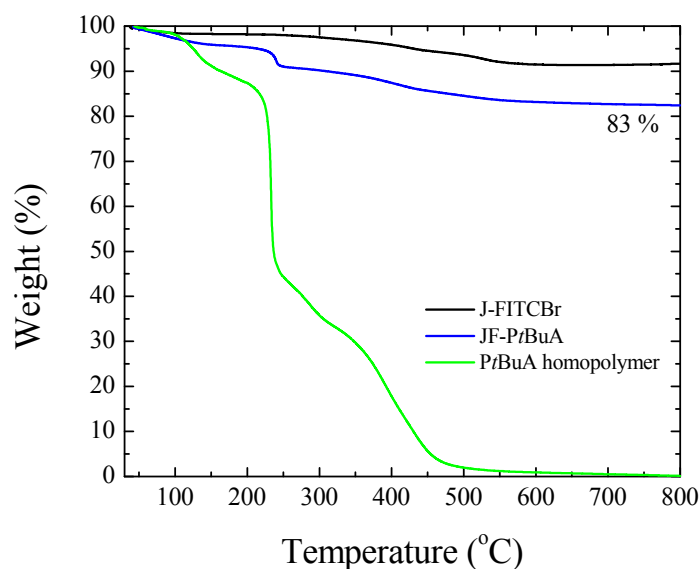


**Figure 3.61.** Thermogram of the Janus PtBuA-coated particles.

The PtBuA polymer grown from the unbound initiator added in the surface-initiated ATRP of *t*BuA from the Janus initiator-coated particles was analyzed by GPC. The chromatogram (Figure 3.62) shows a narrow peak indicating a good control of the polymerization. The molecular weight was found to be 219,300 g/mol with a polydispersity index of 1.26. Assuming that the polymerization of *t*BuA is carried out in a similar manner from the surface of the particles, the molecular weight of the

grafted chains is 109,650 g/mol. This is due to the fact that both the free and the surface-bound initiators are bifunctional, and thus two grafted polymer chains are grown from each bound initiator molecule.

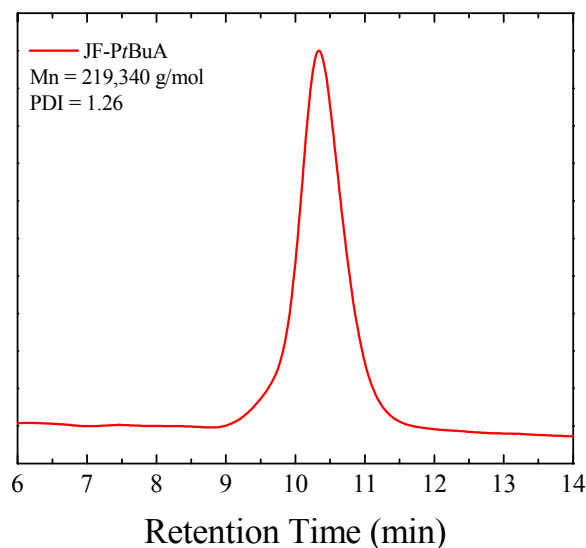


**Figure 3.62.** Chromatogram of the free polymer obtained for the surface-initiated ATRP of *t*BuA from the Janus particles.

The TGA and GPC results are summarized in Table 3.8 where the grafting density of the chains is also calculated. An effective 0.11 chains/nm<sup>2</sup> was found, assuming that the chains are homogeneously distributed on the whole particle surface. The lower grafting density found for the JF-*Pt*BuA particles compared to the value calculated above for the JF-PMMA particles is attributed to the bulkier nature of the *t*BuA monomer repeat units. The amount of chains grafted per particle was found 21,100 which is considerably lower compared to that calculated for the FCF-*Pt*BuA particles (72,600 chains per particle).

**Table 3.8.** TGA and GPC results, grafting density and number of chains per particle for the JF-*Pt*BuA particles.

	JF- <i>Pt</i> BuA 72 h
Polymer weight fraction	0.17
$M_n$ free polymer (g/mol)	219,300
$M_n$ grafted polymer (g/mol)	109,650
grafting density (chains/nm <sup>2</sup> )	0.11
chains per particle	21,100

SEM was utilized in order to observe the topology of the JF-*Pt*BuA particles. Figure 3.63a shows uniform sized spherical particles while at higher magnifications (Figure 3.63b) a sticky neck appears between the particles which was attributed to interpenetrating polymer chains between neighboring particles. However, no specific Janus topology is observed in the tilted view (Figure 3.63b) which is attributed to the low polymer content of the hybrid particles.

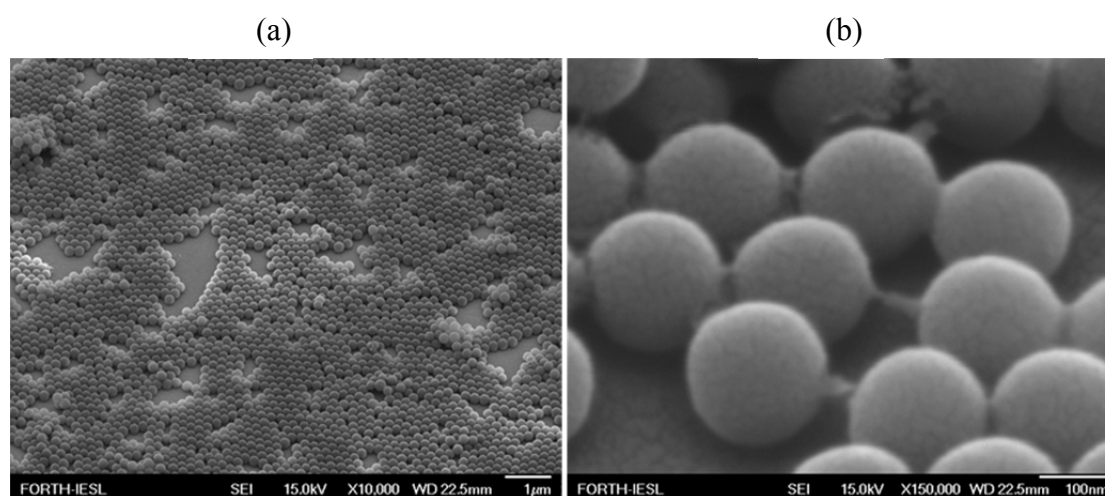


**Figure 3.63.** SEM images of the JF-*Pt*BuA particles from a top view (a) and a 45° tilted view (b).

The hydrodynamic size of the JF-*Pt*BuA particles was measured by DLS. Figure 3.64 shows a single exponential decay of the intensity autocorrelation functions while the decay rates increase in a linear fashion as a function of  $q^2$ . This is indicative of particles with a uniform size as well as the absence of aggregates. The diffusion coefficient of the particles in DMF was found to be  $1.658 \cdot 10^{-12}$  m<sup>2</sup>/s which is equivalent to a hydrodynamic diameter of 281.4 nm.

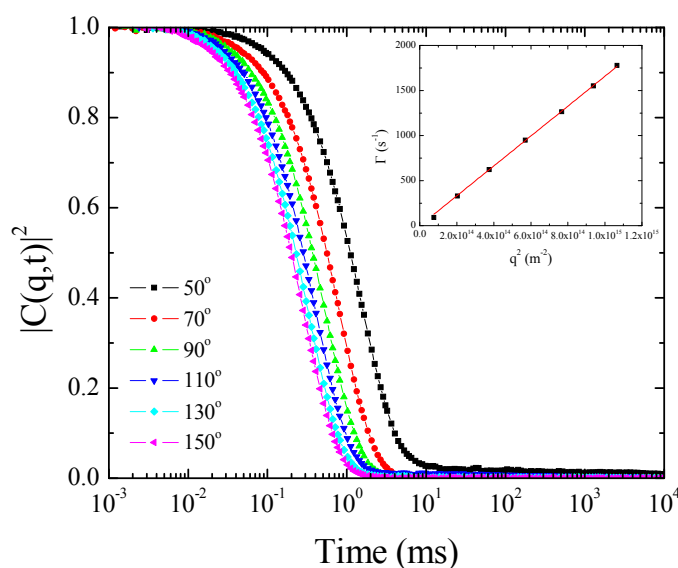


**Figure 3.64.** Intensity autocorrelation functions for the JF-PtBuA particles. Inset: Decay rates as a function of the square wavevector.

Hydrolysis of the PtBuA in order to produce PAA was carried out by the reaction with TFA in an organic solvent (dichloromethane). However, aggregation of the particles was observed upon purification in water which was attributed to the opposite charge on the two parts of the PAA-silica Janus particles. Therefore, extensive investigation of the pH-dependent aggregation of the particles is required.

Comparison of the JF-PtBuA and the FCF-PtBuA particles shows that although the molecular weight of the grafted polymer chains is similar, the calculated number of chains per particle is over 3 times lower for the JF-PtBuA particles. In addition to that, the smaller hydrodynamic size of the JF-PtBuA particles suggests the successful transformation of the silica particles into PtBuA-silica Janus particles.

### 3.8.3 PDMAEMA Janus particles (JF-PDMAEMA)

DMAEMA was polymerized by bulk ATRP from the initiator-functionalized surface of the Janus particles in order to provide the attractive properties of PDMAEMA in aqueous solutions to the Janus particles. The PDMAEMA-coated surface of the particles will demonstrate pH and temperature-responsive behavior while the APTES-modified hemisphere is only protonated at low pH values.

The successful grafting of the PDMAEMA chains from the surface of the Janus initiator-coated particles was verified by TGA. Figure 3.65 shows the TGA curve for the JF-PDMAEMA particles which is compared to a PDMAEMA homopolymer that exhibits a similar decomposition behavior (a two-step decomposition process). The total weight loss was found to be 21.5 % and was attributed to the thermal decomposition of the organic content of the hybrids.

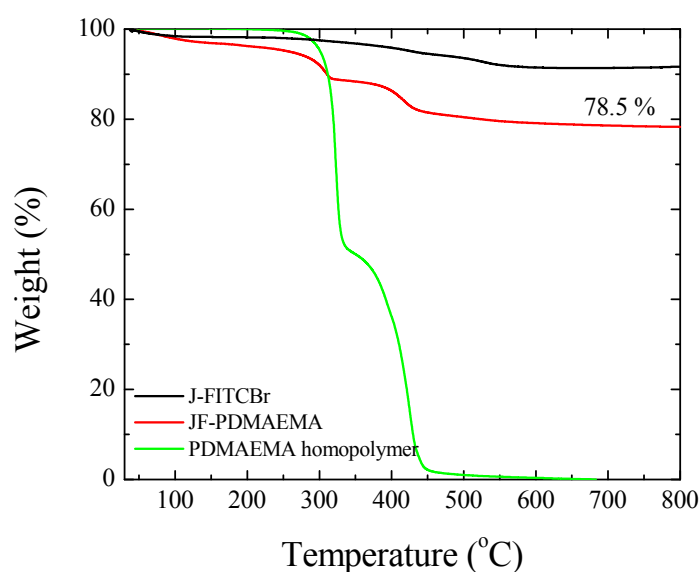


**Figure 3.65.** Thermogram of the PDMAEMA-coated Janus particles.

The free polymer, grown from the unbound initiator present in the ATRP of DMAEMA from the surface of the Janus particles, was analyzed by GPC (Figure 3.66). The resulting peak was narrow indicating good control of the polymerization reaction and the absence of side-reactions. The molecular weight of the polymer was found to be 238,400 g/mol with a polydispersity index of 1.18. Assuming that the surface-initiated polymerization was carried out in a similar fashion as that in the

solution, the molecular weight of the grafted chains is found to be 119,200 g/mol, since from each surface-bound initiator molecule two polymer chains are grown.

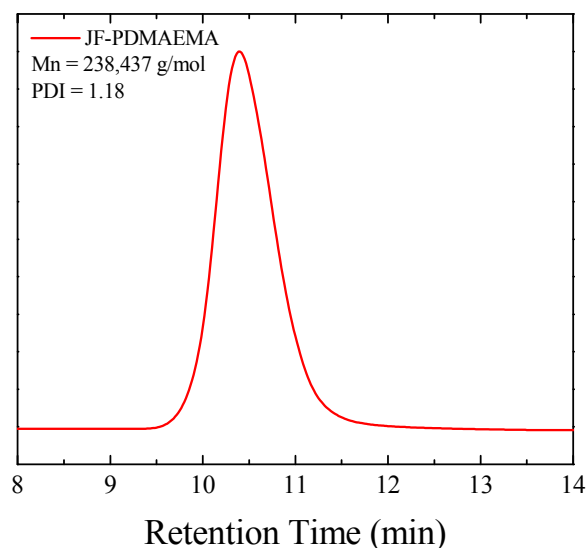


**Figure 3.66.** Chromatogram of the free polymer synthesized for the surface-initiated ATRP of DMAEMA from the Janus initiator-coated particles.

The TGA and GPC results for the JF-PDMAEMA particles are summarized in Table 3.9 where the grafting density and the number of chains per particle is also calculated. It is found that 0.11 chains/nm<sup>2</sup> are grafted on the particle surface assuming a homogeneous distribution of the chains on the total particle surface. The number of chains per particles is found 22,100 chains per particle, a value significantly lower than the one found for the FCF-PDMAEMA particles (99,400 chains per particle) but similar to the JF-P*t*BuA particles. The lower grafting density is attributed to the partial surface coverage of the particles with polymer.

**Table 3.9.** TGA and GPC results, calculation of the grafting density and number of chains per particle for the JF-PDMAEMA particles.

	JF-PDMAEMA 40 h
Polymer weight fraction	0.22
$M_n$ free polymer (g/mol)	238,400
$M_n$ grafted polymer (g/mol)	119,200
grafting density (chains/nm <sup>2</sup> )	0.11
chains per particle	22,100

The JF-PDMAEMA particles were observed by SEM in order to determine their topology. Figure 3.67 shows spherical particles with a nodule attached on one side. This topology is consistently observed throughout the sample. The larger spherical particles are attributed to the silica particles while the nodule is attributed to the collapsed PDMAEMA chains on one side of the particles surface. From these results it is concluded that the JF-PDMAEMA particles have a snowman-like topology.

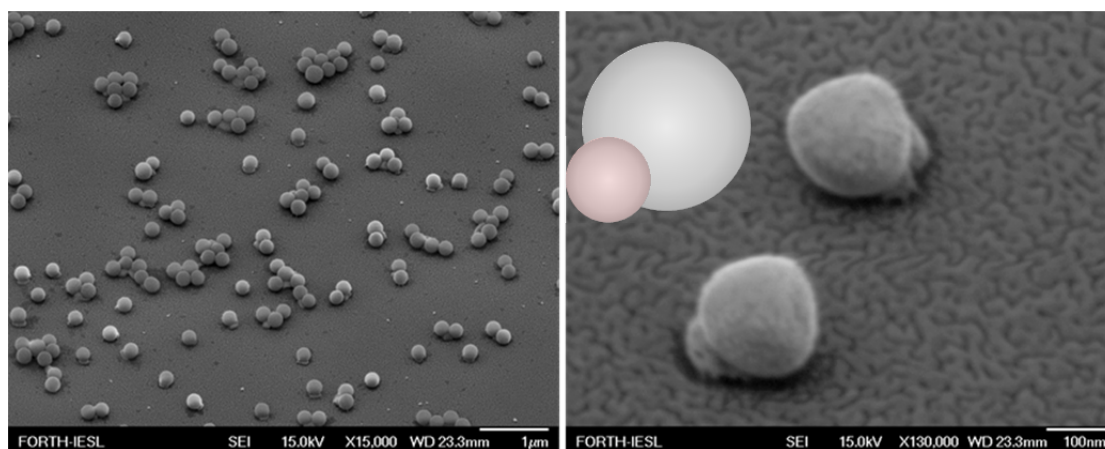


**Figure 3.67.** SEM images of the JF-PDMAEMA particles from a tilted view.

The hydrodynamic size of the JF-PDMAEMA particles was calculated by DLS measurements in DMF. Figure 3.68 shows a single exponential decay of the intensity autocorrelation functions accompanied by linear increase of the decay rates with  $q^2$ . This indicates particles with uniform size and the absence of aggregates. The diffusion coefficient was found to be  $8.592 \cdot 10^{-13} \text{ m}^2/\text{s}$  which corresponds to a hydrodynamic diameter of 543 nm.

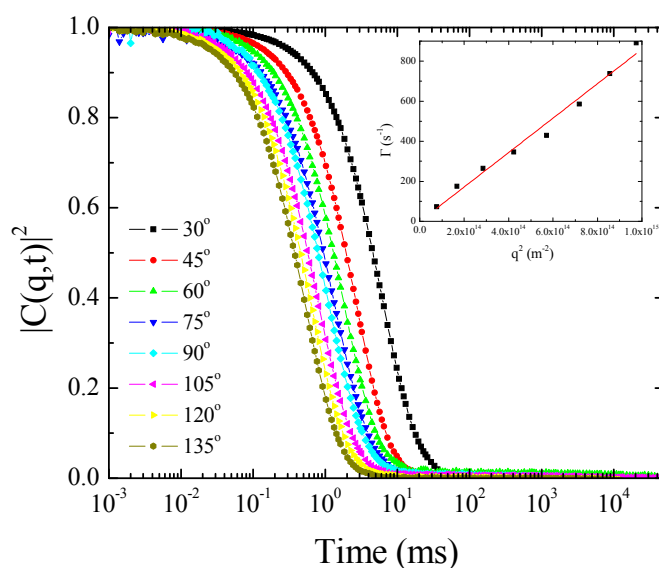


**Figure 3.68.** Intensity autocorrelation functions for the JF-PDMAEMA particles.

Inset: Decay rates as a function of the square wavevector.

The radius of gyration of the JF-PDMAEMA particles was calculated from the minimum of the scattered intensity as a function of the wavevector (Figure 3.69). This was found to be at  $0.0226 \text{ nm}^{-1}$  which corresponds to a radius of gyration equal to 152.1 nm. Therefore the shape factor of the particles is calculated to be 0.56. This value strongly diverges from the known value for hard spheres (0.774), however its correlation to snowman-like particles is not possible at this point.

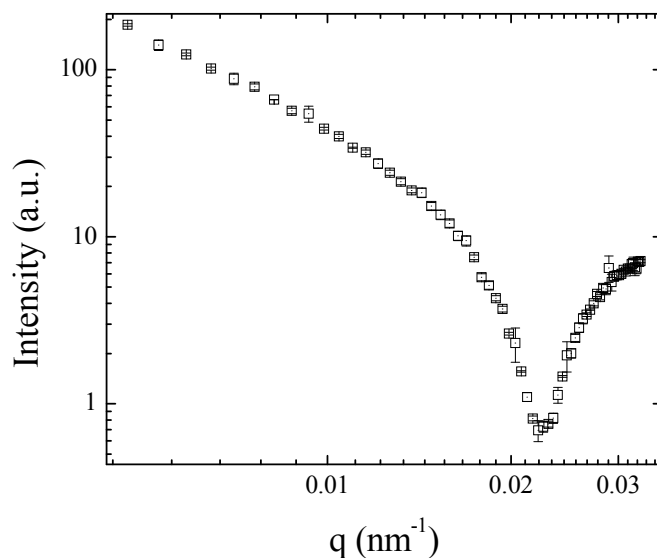


**Figure 3.69.** Scattered intensity for a dispersion of the JF-PDMAEMA particles in DMF as a function of the wavevector.

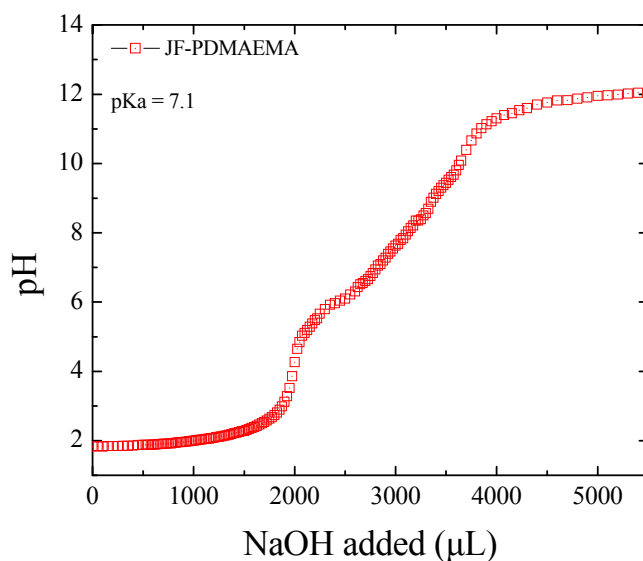
Comparison of the JF-PDMAEMA and the FCF-PDMAEMA particles (Table 3.10) shows that the grafting density of the latter, and thus the number of grafted chains per particle, is 5 times higher. However, although the  $R_h$  found for the JF-PDMAEMA particles is higher, the  $R_G$  of the two samples is similar, resulting in different shape factors. Since to our knowledge no model for snowman-like particles exists, these numbers cannot be correlated to the Janus character of the particles at this point.

**Table 3.10.** Comparison of the molecular weight of the grafted chains, the grafting density, the calculated number of chains per particle, the  $R_h$ , the  $R_G$  and the shape factor for the FCF-PDMAEMA and the JF-PDMAEMA particles.

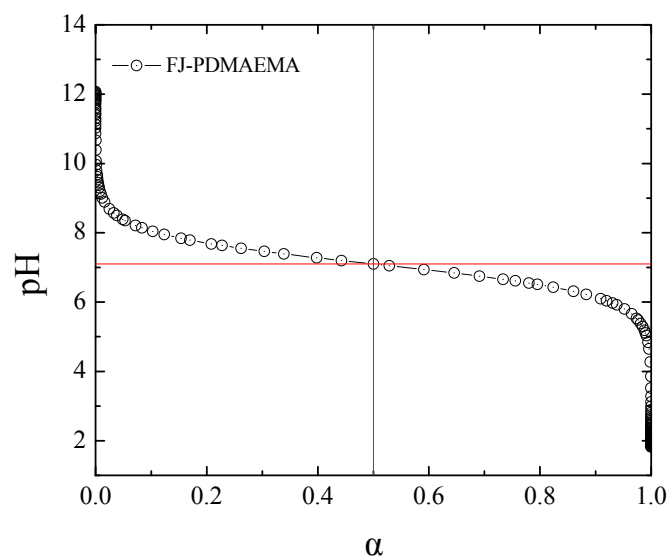
	FCF-PDMAEMA 40 h	JF-PDMAEMA 40 h
$M_n$ grafted polymer (g/mol)	76,250	119,200
grafting density (chains/nm <sup>2</sup> )	0.51	0.11
chains per particle	99,400	22,100
$R_h$ (nm)	195.0	271.5
$R_G$ (nm)	152.5	152.1
$\rho$	0.782	0.560

*(i) pH-responsive behavior*

The pH-dependent behavior of the JF-PDMAEMA particles was examined by potentiometric titration and DLS. Figure 3.70 shows the titration curve for the JF-PDMAEMA particles as a function of added NaOH. A wide plateau region is observed attributed to the simultaneous protonation of the DMAEMA moieties on one hemisphere of the particles and the primary amino groups on the other hemisphere of the particles. The overlapping ionization regions are due to the similar  $pK_a$  values of the ionizable moieties (6.7 for PDMAEMA and 5 for the primary amino groups) and hinder the independent calculation of the two  $pK_a$  values for the JF-PDMAEMA particles. An average value of the total ionizable groups at 50 % ionization could be only calculated at  $pH = 7.1$  (Figure 3.71).

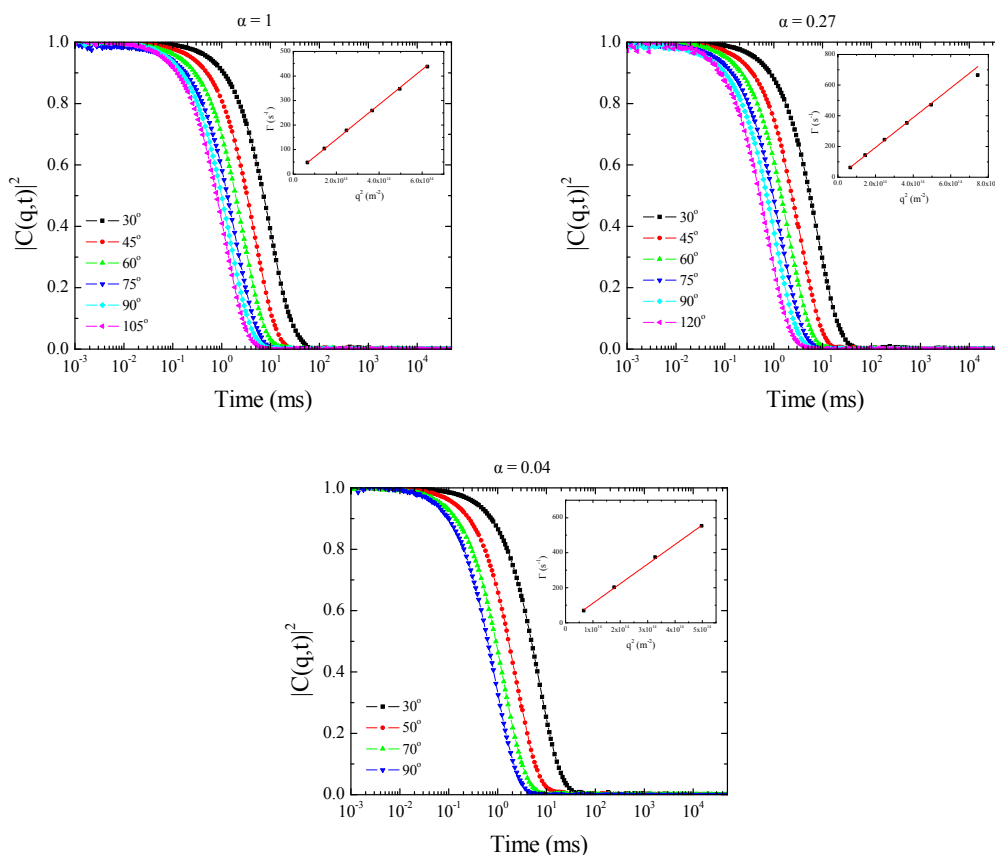


**Figure 3.70.** Potentiometric titration for the JF-PDMAEMA particles upon addition of NaOH.



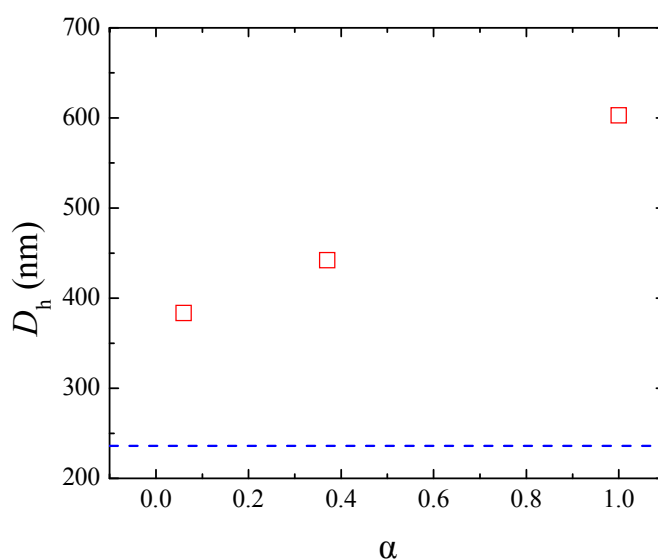
**Figure 3.71.** Solution pH as a function of the degree of ionization of the total amine groups for the JF-PDMAEMA particles.

The effect of the degree of ionization of the amine groups on the hydrodynamic size of the particles was investigated by DLS measurements. The intensity autocorrelation functions shown in Figure 3.72 demonstrate a single exponential decay behavior while the decay rates increase in a linear fashion as a function of the square wavevector. This is indicative of particles with uniform size and the absence of aggregates. The diffusion coefficient at a degree of ionization equal to  $\alpha=1$  where all the amine groups are protonated was found to be  $7.106 \cdot 10^{-13} \text{ m}^2/\text{s}$  which corresponds to a hydrodynamic diameter of 602.8 nm. This value is considerably higher than the one found for the JF-PDMAEMA particles in DMF, and was attributed to the electrostatic repulsions among the charged polymer chains that drive the polymer to adapt an extended conformation in solution. At a lower degree of ionization ( $\alpha = 0.27$ ) the diffusion coefficient was found to be higher and equal to  $9.688 \cdot 10^{-13} \text{ m}^2/\text{s}$  which corresponds to a hydrodynamic diameter of 442.2 nm. Upon further deprotonation of the particles, the diffusion coefficient increases further to  $1.114 \cdot 10^{-12} \text{ m}^2/\text{s}$ , a value that corresponds to a hydrodynamic diameter of 384.6 nm.



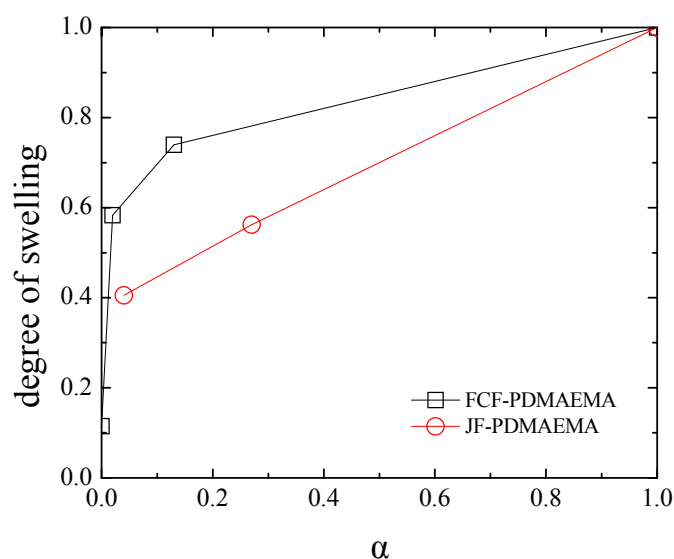
**Figure 3.72.** Intensity autocorrelation functions of the JF-PDMAEMA particles at different degrees of ionization. Insets: Decay rates as a function of the square wavevector.

The above results are summarized in Figure 3.73 where the hydrodynamic diameter of the particles is shown as a function of the total degree of ionization of the amine groups. The decrease of the degree of ionization results in the gradual decrease of the hydrodynamic diameter of the particles, which is attributed to the deprotonation of the polymer and thus shrinkage of the PDMAEMA chains in solution. It is noted that for the Janus particles no aggregation was observed down to 4 % ionization of the amine groups.



**Figure 3.73.** Dependence of the hydrodynamic diameter of the JF-PDMAEMA particles on the total degree of ionization ( $\alpha$ ). The blue line shows the hydrodynamic diameter of the initiator-coated FCF particles for comparison.

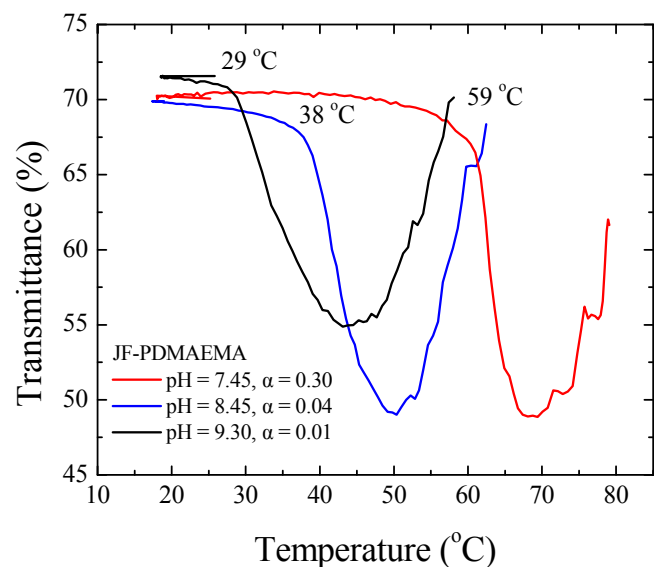
Comparison of the pH-dependent size of the JF-PDMAEMA and the FCF-PDMAEMA particles is shown in Figure 3.74 where the degree of swelling of the polymer layer is calculated as a function of the degree of ionization. For both samples a decrease of the degree of swelling was observed and was attributed to the shrinkage of the particles as the polymer chains become deprotonated and collapse onto the surface of the particles. However at similar degrees of ionization for the two samples, a lower degree of swelling is observed for the JF-PDMAEMA sample. This was attributed to the snowman-like topology of the JF-PDMAEMA particles which, in contrast to the dense brushes of the FCF-PDMAEMA particles, provides more space to the polymer chains to collapse.



**Figure 3.74.** Degree of swelling of the PDMAEMA polymer layer as a function of the degree of ionization for the FCF-PDMAEMA and the JF-PDMAEMA particles.

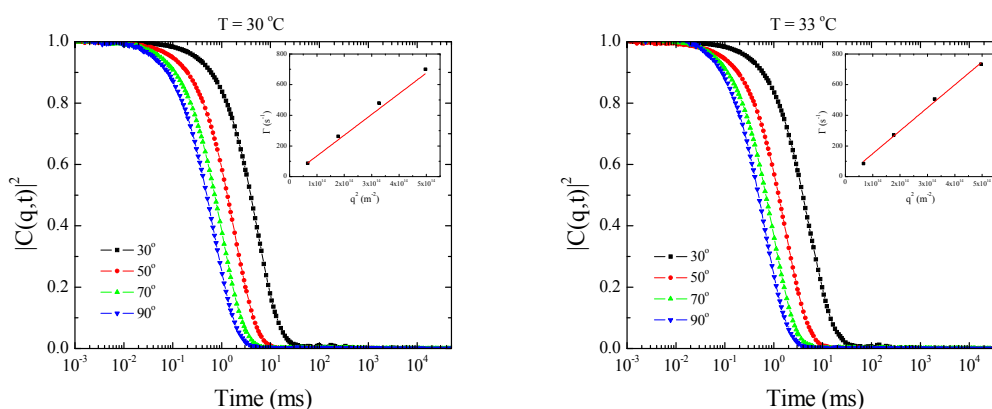
(ii) *Temperature-responsive character*

The temperature-responsive properties of the JF-PDMAEMA particles were also studied by turbidimetry and DLS. Figure 3.75 shows the dependence of the optical transmittance of a dispersion of the JF-PDMAEMA particles on the solution temperature. The rapid decrease of the transmittance at different temperatures for different degrees of ionization of the particles was attributed to the LCST of the particles. For a total degree of ionization equal to 0.3 the LCST of the particles was found to be at 59 °C while upon lowering the degree of ionization to 4 % the LCST decreased to 38 °C. Finally, an almost complete deprotonation of the particles ( $\alpha = 0.01$ ) resulted in the decrease of the LCST to 29 °C. This behavior is expected since at higher degrees of ionization a larger number of amine groups is protonated leading to an increase of the LCST due to the increase of the hydrophilicity of the polymer.



**Figure 3.75.** Transmittance as a function of the solution temperature for the FCF-PDMAEMA particles in aqueous media, at a wavelength of 600 nm.

The effect of the solution temperature on the size of the JF-PDMAEMA particles was evaluated by DLS measurements at a constant degree of ionization  $\alpha$  equal to 0.04. Figure 3.76 shows the intensity autocorrelation functions for a dispersion of the particles at different scattering angles and different temperatures. The calculated diffusion coefficients and the corresponding hydrodynamic diameters are summarized in Table 3.11.



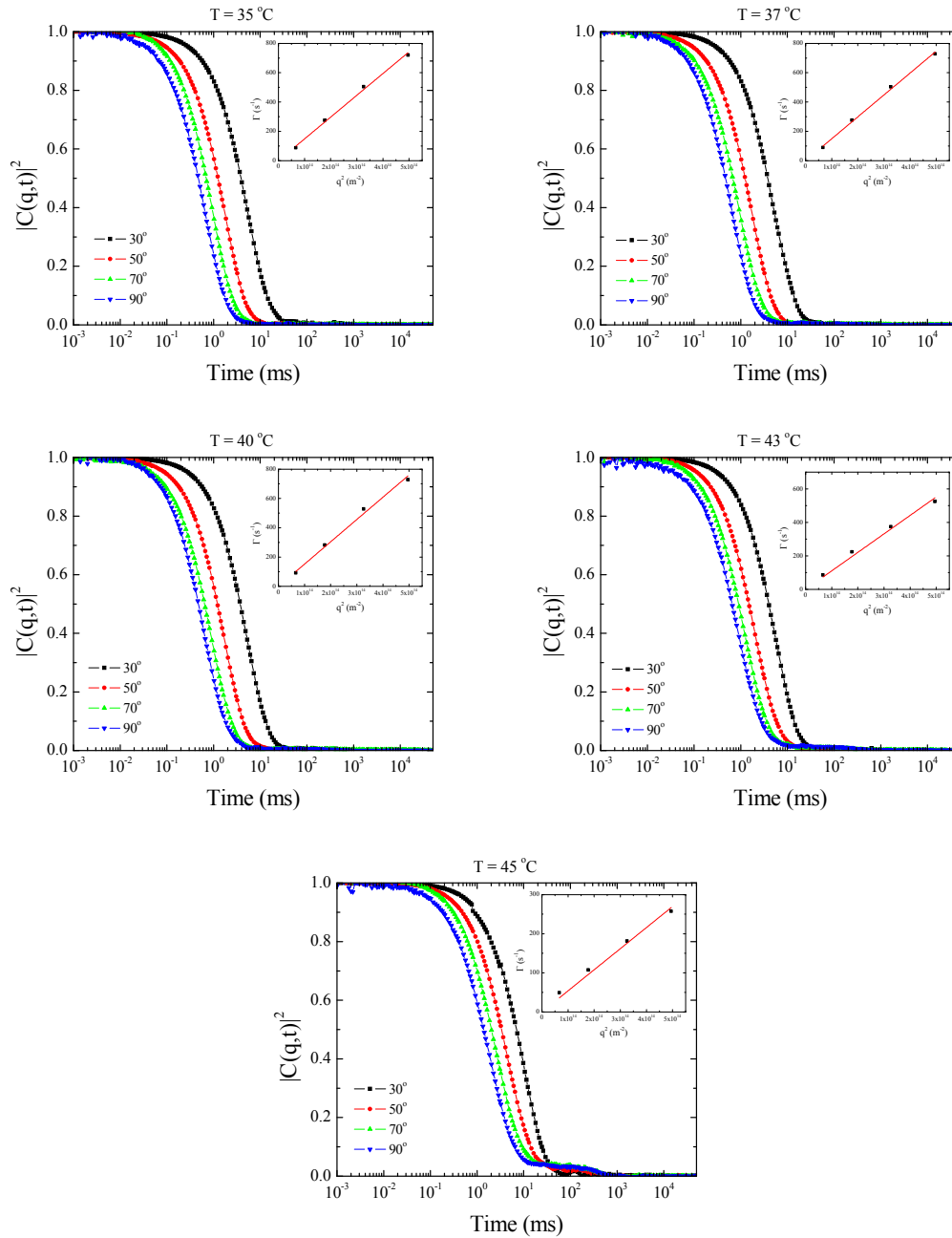


**Figure 3.76.** Intensity autocorrelation functions for the JF-PDMAEMA particles at different scattering angles and different temperatures in water. Insets: Decay rates as a function of the square wavevector.

**Table 3.11.** Diffusion coefficients and the corresponding hydrodynamic diameters for the JF-PDMAEMA particles as a function of solution temperature.

Temperature °C	Ds m <sup>2</sup> /s	Dh nm
20	$1.114 \cdot 10^{-12}$	384.6
30	$1.115 \cdot 10^{-12}$	385.1
33	$1.499 \cdot 10^{-12}$	399.2
35	$1.485 \cdot 10^{-12}$	422.1
37	$1.195 \cdot 10^{-12}$	439.1
40	$1.521 \cdot 10^{-12}$	461.7
43	$1.509 \cdot 10^{-12}$	496.4
45	$5.395 \cdot 10^{-13}$	1448.7

Figure 3.77 shows the dependence of the hydrodynamic diameter of the JF-PDMAEMA particles on the solution temperature. From 20 °C to 30 °C no significant effect on the particles size is observed. However, upon increasing the temperature above 30 °C, the size of the particles seems to gradually increase. At 45 °C the significant increase of the measured size is attributed to the extensive aggregation of the particles induced by the collapse of the PDMAEMA chains. This behavior is in contrast to the observation made for the FCF-PDMAEMA particles under similar conditions where the size of the particles decreased gradually prior to aggregation. It is speculated that above the LCST of the polymer the particles form controlled aggregates that are dispersed in the medium due to the presence of the primary amines on the exposed surface of the aggregates. However, at this point this is only a speculation that remains to be proved.

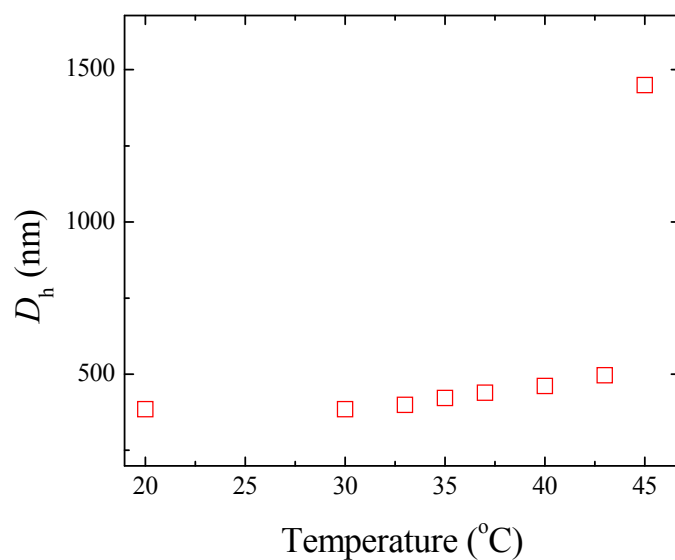


**Figure 3.77.** Dependence of the hydrodynamic diameter of the JF-PDMAEMA particles ( $\alpha = 0.04$ ) on the solution temperature.

- 
- (1) Bottom, C. B. Hanna, S. S.; Siehr, D. J. *Biochemical Education* **1978**, *6*, 4-5.
  - (2) Giermanska-Kahn, J. Laine, V. Arditty, S. Schmitt, V.; Leal-Calderon, F. *Langmuir* **2005**, *21*, 4316-23.
  - (3) Choi, S.; Zhangnewby, B. *Surface Science* **2006**, *600*, 1391-1404.
  - (4) Moatsou, D. Synthesis of polymer functionalized silica nanoparticles by surface initiated atom transfer radical polymerization, University of Crete, 2009, p. Diploma Thesis.



## **Chapter 4 | Conclusions**

The purpose of this work was to synthesize polymer-silica Janus particles by growing polymer chains in a controlled manner from a part of the surface of initiator functionalized Janus silica particles. The selection of monomers was based on the known properties of the functional polymers, that being PMMA which is hydrophobic, *Pt*BuA which is hydrophobic but can be hydrolyzed to form the anionic pH-responsive PAA and PDMAEMA which is hydrophilic, ionizable and responsive to pH and temperature changes.

### **4.1 Controlled ATRP in bulk**

To achieve the controlled growth of the polymer chains from the surface of the particles, a versatile technique was selected; ATRP. The polymerization conditions for all three monomers were first optimized in the absence of silica particles in order to achieve controlled polymer synthesis, in terms of reaction time, polymer molecular weight and molecular weight distribution.

ATRP of MMA in bulk was initiated both from a monofunctional commercially available initiator and a synthesized bifunctional initiator. GPC results showed that the polymerization carried out in the presence of the monofunctional initiator was controlled and capable of providing PMMA with high molecular weight in short polymerization times. The use of a bifunctional initiator provided polymers of relatively narrow molecular weight distributions, although the reaction kinetics were not typical of a controlled polymerization. However, polymers with high molecular weights were synthesized in short reaction times rendering the bifunctional initiator a viable ATRP initiator.

The controlled nature of the ATRP of *t*BuA was also studied. Despite the long reaction times needed to produce polymers with molecular weights higher than 100,000 g/mol, it was shown that the molecular weight of the polymer chains increased linearly while the molecular weight distributions decreased exponentially. This typical behavior of a “living” polymerization, together with the narrow molecular weight distributions obtained proved the controlled growth of *Pt*BuA chains by ATRP.

DMAEMA is a monomer of particular interest as only a handful of reports exist on the controlled synthesis of high molecular weight PDMAEMA. In this work two catalytic systems were studied resulting in the production of high molecular weight polymers. Cu(I)Br was proven a valid choice when short reaction times were needed, although some termination reactions were observed leading to a broadening of the molecular weight distribution with reaction time. On the other hand, Cu(I)Cl exhibited a “living” polymerization behavior and a decrease of the molecular weight distribution at high monomer conversions, at the price of longer reaction times.

#### **4.2 Fully polymer-coated particles**

The monomer polymerization conditions investigated in bulk were employed in order to successfully grow dense polymer brushes from the surface of commercially available silica particles using a surface-initiated polymerization method. Two surface-bound initiators were synthesized; a monofunctional and a bifunctional one.

ATRP of MMA was carried out in a control manner from the surface of the silica particles. The successful grafting of the polymer was evidenced by a significant weight loss found by TGA, as well as by the increase of the size of the particles as shown by DLS. The control of the reaction was indicated by the narrow peaks observed in the GPC of the free polymers. Two hybrid samples with different polymer chain lengths, by carrying out the polymerization at different reaction times, were prepared utilizing the bifunctional initiator-coated particles. This was shown by GPC as a growth of the molecular weight of the polymer, while the polymer content found by TGA and the size of the particles measured by DLS increased also verifying the grafting of longer chains from the surface of the particles. A larger size for the particles with the longer polymer chains was also found by SEM. When comparing the results of the particles functionalized with the two initiators, it was found that the bifunctional initiator-coated particles were able to grow 6 times more dense PMMA chains from the surface of the particles compared to the monofunctional initiator-coated particles.

*t*BuA was also successfully grown from the surface of the silica particles. The polymerization initiated from the surface of the monofunctional initiator-coated particles was controlled, as confirmed from the narrow peaks observed by the GPC

measurement of the free polymers. An increase of the polymer content and the size of the hybrid particles was found by TGA and DLS, respectively, attributed to the growth of the polymer chains with the reaction time. On the other hand, the polymer chains grown from the surface of the bifunctional initiator-coated particles were rather bimodal and with a broad molecular weight distribution, signifying the loss of the polymerization control. This was attributed to the long reaction times required which rendered the reactive chains labile to side reactions.

Finally, the successful growth of PDMAEMA chains from the surface of the silica particles was confirmed by TGA and DLS. Both the monofunctional and bifunctional initiator-coated particles polymerized DMAEMA in a controlled manner as evidenced by the narrow peaks obtained by GPC. The latter were found to have a much higher amount of chains grafted per particle (4 times), proving the effectiveness of the bifunctional initiating sites. The PDMAEMA-coated particles were pH-responsive exhibiting changes in their size with the degree of ionization of the DMAEMA units as shown by DLS measurements. The temperature-induced collapse of the PDMAEMA chains onto the particle surface was also shown by DLS while the macroscopic precipitation of the particles above the LCST of the polymer in water was observed by turbidimetry and the onset was dependent on the degree of ionization of the polymer.

### **4.3 Colloidosomes**

In need of an interface where the particles would be trapped in order to partially modify their surface, hybrid colloidosomes were synthesized. Initial attempts involved the use of wax in different organic solvents onto the surface of which the silica particles were immobilized. However, this method was proven unsuitable due to the formation of multiple layers of silica particles onto the wax-solvent interphase and the presence of unbound particles in solution. Although the use of water as the continuous medium for the formation of wax-silica colloidosomes has been reported in the literature and was successfully repeated in this work, it was shown that modification of the exposed surface of the particles with ATRP initiating sites resulted in the desorption of the silica particles from the surface of the wax microparticles and the failure to prepare Janus initiator particles.

The synthesis of polystyrene-silica hybrid colloidosomes in methanol was found to be a valid solution to this problem. Amine-functionalized silica particles formed monolayers embedded in the polymer surface, while the functionalization of their exposed surface with the bifunctional initiator did not compromise the stability of the colloidosomes. Therefore, Janus colloidal initiator particles were successfully synthesized in a one gram scale.

#### **4.4 Janus particles**

The successful transformation of the commercial silica particles into Janus initiator-coated particles was proven by dyeing the two particle parts with different fluorescent pigments, observed by fluorescence microscopy, as well as by decorating the polymer buried side of the particles with small gold nanoparticles, observed by TEM.

Next, the Janus particles were used as colloidal multifunctional initiators for the synthesis of PMMA brushes. TGA verified the successful synthesis of the Janus polymer-silica particles, while GPC confirmed the controlled nature of the polymerization reaction. The size of the particles was evaluated by DLS and SLS measurements, while SEM images provided insight on the topology of the Janus particles, indicating the formation of acorn-like particles. Comparison of the fully PMMA-coated particles with the Janus PMMA particles verified their anisotropic character, as indicated by the lower grafting densities and smaller hydrodynamic sizes of the latter. The ability of the particles to stabilize water-oil emulsions was also shown.

P(*t*BuA) was also grown from the initiator-coated surface of the Janus particles by ATRP. The organic content assessed by TGA measurements and the larger size of the particles found by DLS verified the presence of the polymer chains which, according to the narrow peaks obtained by GPC, were grown in a controlled manner. The calculated low grafting density of the polymer was indicative of the Janus character of the particles, although no specific topology was observed by SEM.

Finally, PDMAEMA chains were successfully grown from the initiator-functionalized surface of the Janus particles, as verified by TGA. The low molecular weight distribution of the polymer found by GPC was indicative of the controlled

surface-initiated ATRP. The number of chains grafted on the Janus particles was significantly lower than that calculated for the fully PDMAEMA-coated particles which accompanied by the SEM images in which snowman-like particles were observed, proved the anisotropic character of the particles. The pH-dependent size of the Janus PDMAEMA particles was shown by DLS measurements verifying the pH-responsive behavior of the Janus particles. Although a temperature-induced precipitation of the particles was observed by turbidimetry, the size of the particles measured by DLS was not found to decrease before the LCST of the polymer, as was the case for the fully-coated PDMAEMA particles. Instead, an increase of the size of the particles was found attributed to the formation of controlled aggregates.

#### **4.5 Future work**

Due to the versatility of the proposed method towards the synthesis of Janus particles it is now possible to produce various combinations of functionalities on the two parts of the particles in high yields.

It is proposed that the particles synthesized in this work can be used as templates for the synthesis of dual-functionalized polymer Janus particles. That is, by the controlled growth of a different polymer from the ungrafted part. The Janus PMMA particles would be rendered into amphiphilic polymer-coated particles by the growth of a hydrophilic polymer. The Janus *Pt*BuA particles have been already hydrolyzed to produce anionic PAA chains. The growth of a cationic polymer from the ungrafted surface will provide polyampholyte particles with an interesting aggregation behavior as a function of the solution pH.

The Janus PDMAEMA particles possess interesting temperature-responsive properties. We propose that rapid switching of the temperature of an aqueous dispersion of the particles around the LCST of the polymer could propel the particles due to the alternating collapsing-hydration of the chains, mimicking the flagella-induced movement of some micro-organisms.

In the future, a light-responsive monomer will be incorporated in the polymer allowing a use of a less intrusive stimulus to collapse-hydrate the polymer coating of the Janus particles.



## Ευχαριστίες

Για την περάτωση αυτής της μεταπτυχιακής εργασίας θα πρέπει να αναγνωριστεί η συμβολή κάποιων ανθρώπων.

Σε πρώτη φάση θα ήθελα να ευχαριστήσω προκαταβολικά τα μέλη της τριμελούς επιτροπής, κο Πετεκίδη και κο Φυτά, για την υπομονή και τη συμμετοχή τους.

Θα ήθελα επίσης να ευχαριστήσω τους Σάντρα Σιάκουλη, Αλέκα Μανουσάκη, Στέφανο, Δημήτρη Θεοδωρίδη, Λάμπρο Παπουτσάκη όπως και τον κο Παντελή Τρικαλίτη για τη συμμετοχή τους στη μικροσκοπία.

Η ομάδα πολυμερών-κolloειδών του ΙΤΕ αποτέλεσε σημαντική υποστήριξη για μένα κατά τη διάρκεια της αναζήτησής μου στο λαβύρινθο της επιστήμης μας και για αυτό θα είμαι ευγνώμων (παρόλο που δεν ξέρουν να παίζουν ποδόσφαιρο).

Οι τελευταίες 100 + σελίδες θα ήταν κενές χωρίς το θετικό κλίμα που επικρατεί τα τελευταία δύο χρόνια, που διήρκεσε η εκπόνηση αυτής της εργασίας, αλλά και τα δύο χρόνια της διπλωματικής που προηγήθηκαν, στο εργαστήριο σύνθεσης πολυμερών. Οφείλω να ευχαριστήσω θερμά τους φίλους και συνεργάτες μου όλα αυτά τα χρόνια: Μαρία Καλύβα, Γιώργο Πασπαράκη, Nikki Mateescu, Δήμητρα Αχιλλέως, Φάνη Κρασανάκη, Ορέστη Φαληρέα, Ελμίνα Καμπουράκη, Κωνσταντίνο Στόικο, Μαρία Κισσαμιτάκη αλλά και τα νεότερα μέλη: Μαρία Βεργάκη και Χαρά Φλουράκη όπως και τον guest star Ανδρέα Παμβουξόγλου.

Μου είναι αδύνατο να χωρέσω την ευγνωμοσύνη μου για το «αφεντικό» σε μία παράγραφο. Είμαι τυχερή που το ένστικτό μου για την καθηγήτριά μου, Μαρία Βαμβακάκη, αποδείχθηκε σωστό. Κάθε συμβουλή της, επιστημονική και μη, αποδείχθηκε πολύτιμη. Η μεταδοτικότητα της γνώσης και του πνεύματος είναι χάρισμα, λένε.

Οι πιο 'ρηγμένοι' στην υπόθεση master ήταν οι φίλοι και η οικογένειά μου, μιας και στο λίγο χρόνο που πέρασα μαζί τους έπρεπε να υπομένουν την φλυαρία μου για τα Janus μπαλάκια. Σαν ανταπόδοση τους αφιερώνω την τελευταία παράγραφο αυτής της ιστορίας. Μοατσέοι, Όλγα, Αντρέα, Μαρία, Χριστιάνα, Άλκη, Αλέξανδρε, Φένη, Κωνσταντίνε .. ευχαριστώ.

